Quantum Fluctuations in Kondo Materials and Kitaev Quantum Spin Liquids

Huanzhi Hu

A dissertation submitted in partial fulfillment

of the requirements for the degree of

Doctor of Philosophy

of

University College London.

Department of Physics and Astronomy

University College London

August 6, 2025

I, Huanzhi Hu, confirm that the work presented in this thesis is my own. Where information has been derived from other sources, I confirm that this has been indicated in the work.

Abstract

In strongly correlated systems, quantum fluctuations play a crucial role in the ordering at low temperatures, leading to various exotic ground states. The critical points usually correspond to some universal scaling behaviours, which can be described phenomenologically by the Ginzburg-Landau-Wilson paradigm. However, it breaks down in systems where gapless fermionic excitations or topological features play a key role. Understanding such cases is crucial to explaining complex behaviors in quantum materials, such as unconventional magnetism and quantum spin liquids.

This thesis focuses on some different scenarios where the presence of gapless fermions alters the behavior of the phase transitions. Firstly, we use the perturbative and numerical renormalisation group to study the role of Kondo fluctuations in an anisotropic Kondo model to explain the moment reorientation and hard-direction ordering in Kondo materials. Secondly, we study the antiferromagnetic quantum criticality when the local moments are Kondo-coupled to Dirac fermions, and show that the Néel critical point is stable against the particle-hole fluctuations. In the last part, both the magnetic and topological phase transitions of the Kitaev-Ising model are studied and compared through different Majorana fermion representations, and then a renormalisation group approach is applied to the topological phase transition of the gapless and gapped quantum spin liquid states. It turns out that in the presence of other magnetic interactions, the topological phase transition can be studied in a similar manner as the symmetry-breaking phase transitions of semi-Dirac fermions.

The results in this thesis contribute to the theoretical understanding of fermionic quantum criticality and the nature of novel quantum phase transitions

in strongly correlated electron systems.

Acknowledgements

First I would like to thank my supervisor Dr. Frank Krüger for his selfless guidance, support and generous tolerance of my stupidity throughout my PhD life. I will try my best to ensure that the countless time and beers he spent discussing with me won't be in vain. His sharp instinct in physics and diligent working style set a high goal that I aim to achieve in my lifetime. If it were not him my PhD time wouldn't be such enjoyable. Secondly, I am grateful to my second supervisor Dr. Michal Kwasigroch, whose brilliant ideas have inspired me until today. I am thankful to Prof. Andrew Green for useful discussions and advice.

I would also like to thank Ewan Scott and Jennifer Lin for fruitful discussions. Many thanks to Alexander Broad, Dylan Behr, Sophia Walls and Bangye Qin, who have collectively created the excellent vibe of our office. I am grateful to Chenwei Zheng for his generous help, support and discussions on all sorts of topics, physics or not, throughout the whole PhD journey. Additionally, I would like to thank my housemates Yuhan Yang, Xing Li and Maoze Bai. H9 was made a place full of memories.

At last, I would like to thank my parents, Xin Hu and Guilian Qi, who brought me into this wonderful world, and provided me with undying love and support since. I hope I can be a son they will be proud of.

Impact Statement

The work presented in this thesis provides insights into the effect of quantum fluctuations in exotic quantum phases and phase transitions. The main benefit would be to deepen the understanding of critical phenomena that happen in the quantum regime, which could in principle stimulate and point ways for industrial interests in the application of exotic quantum materials.

Contents

List of Figures

List of Tables

Chapter 1

Introduction

Fluctuations are a fundamental ingredient of many-body physics. They are usually discussed in the context of phase transitions, as they represent the deviation of a physical quantity from its equilibrium value. When the deviation becomes critical, the system may end up in a different equilibrium, indicating a phase transition. In our everyday lives, thermal fluctuations are the key to phase transitions like solid-liquid and liquid-gas transitions. In the quantum regime, a different type of fluctuations, namely quantum fluctuations, which are rooted in the uncertainty principle, can be significant and lead to phase transitions even at zero temperature. In analogy to thermal fluctuations, quantum fluctuations become strong in systems at the vicinity of a quantum critical point, and leads to a wide range of quantum phases at zero temperature. Understanding the role of quantum fluctuations in phase transitions is the key to unravelling the mysteries in strongly correlated electron systems such as the origin of the linear resistivity in strange metals [1], and the microscopic theory of unconventional superconductivity [2].

However, the general difficulty of solving such strongly correlated many-body problems remains the ultimate shadow over the field of condensed matter physics. The number of coupled Schrödinger equations one needs to solve for a typical condensed matter problem is astronomical ($\sim 10^{23}$) even for cutting-edge high-performance computers. Though there are methods like density functional theory in which the wave functions are mapped to electron density functional to reduce the complexity [3], solving the simplified problems is still extremely challenging when

the electron-electron interaction is strong. Fortunately, the ordering in many-body systems corresponds to some emergent collective excitations of the system, rendering the microscopic details irrelevant at the critical point. The phase transition can thus be studied at a phenomenological level by defining a proper order parameter of the ordered phase and working with the theory of such order parameters. This technique, the so-called Ginzburg-Landau theory, was later completed by the renormalisation group method developed by Wilson[4, 5], and became the paradigm for explaining the symmetry-breaking phase transitions in which all other degrees of freedom apart from the order parameter are gapped.

Though extremely powerful, the Ginzburg-Landau-Wilson paradigm is not the full story of second-order phase transitions. Firstly, for a gapless system, there is no way to systematically integrate out the fermions without eliminating the low-energy order parameter modes at the same time. In such cases, the effective theory must also involve fermions explicitly, giving rise to the so-called fermion-induced quantum criticality[6]. Secondly, spontaneous symmetry-breaking is the key to a non-zero order parameter, but it is not a necessary ingredient of phase transitions. Followed by the discovery of the quantum Hall effect in 1980s [7, 8], a new kind of phase transition surfaced, in which the symmetry remains the same in both phases but the topology of how the quantum states wind the parameter space differs. Obviously, a local order parameter theory cannot be constructed to describe such a change in the global topology. To properly define and categorise different topological phases, one needs the language of category theory [9]. In general, phases with nontrivial topology can be distinguished as symmetry-protected trivial (SPT) states and symmetry-enriched topological (SET) states. The latter one has the so-called topological order, which is deeply connected to the large degeneracy and long-range quantum entanglement in the ground states [9]. Furthermore, topological order is usually followed by the emergence of gauge fields and fractionalisation of quasi-particles, which could in principle connect a symmetry-breaking ordered phase and a topologically ordered phase. Examples of such include the deconfined quantum criticality between the antiferromagnetic and resonating valence bond state on a

square lattice[10, 11].

In this thesis, we focus our study on the fermion-induced quantum criticality in gapless systems. The presence of a Fermi surface introduces the fermion fluctuation on top of the order parameter fluctuation, and their interplay can lead to interesting quantum criticality distinct from that of a pure order parameter theory. It is not hard to realise that the shape of the Fermi surface plays a crucial role, and here we will only consider the simple cases in which the Fermi surface is either a point (Dirac semimetals), or a perfect small sphere (metals). The scenarios discussed are quite different at the microscopic level, but the phase transitions turn out to be similar.

Here we first briefly introduce the scenarios that will be discussed in this thesis. For a typical strongly correlated electron system, the underlying low-energy degrees of freedom are charge and spin. Generically, the electrons are subject to long-range Coulomb interactions. However, the scattering events of electrons and holes around the Fermi surface effectively screen the Coulomb interaction, leaving only a short-range residue of it. In this spirit, the simplest model one can write down is the so-called Hubbard model:

$$\hat{H} = -\sum_{\langle ij\rangle,\sigma} t_{ij}(c^{\dagger}_{i\sigma}c_{j\sigma} + H.c.) + U\sum_{i}\hat{n}_{i\uparrow}\hat{n}_{i\downarrow} \tag{1.1}$$

in which the first term is the kinetic energy of electrons, and the second represents the on-site Coulomb repulsion of the electrons. Depending on the specific system and problem, the strength of U may vary, leading to different effective low-energy simplifications of the problem by separating the two degrees of freedom. For example, when the Hubbard repulsion is weak, the kinetic energy dominates the physics, and the interaction of electrons can just be taken as an adiabatic renormalisation of the parameters of a non-interacting Fermi gas, leaving us the famous Fermi liquid theory. In this case, all that matters is the charge degree of freedom, as the interplay of the mobile electron spins averages out. On the other hand, at the strong U limit of a half-filled Hubbard model, the energy penalty for two electrons to sit on the same site is infinite, and the ground state is naturally that there is one electron per

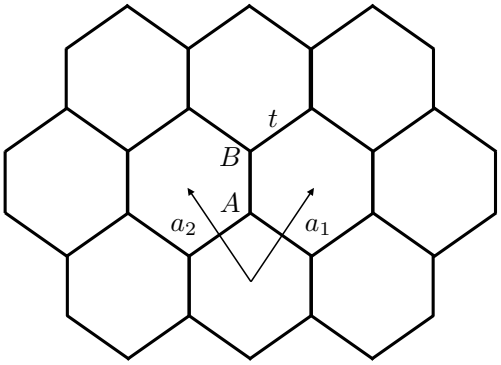

Figure 1.1: Honeycomb structure of graphene. In each unit cell, there are two sites (A, B), corresponding to the sublattice degree of freedom.

site. This is called a Mott insulating state. Since the charge degree of freedom is completely localised, one can then only keep the electron spins into consideration, and end up with the spin-1/2 Heisenberg model. Furthermore, there exist cases in which both degrees of freedom are important, such as the Kondo lattice model. In a Kondo lattice model, The d and f electrons in the transition metal elements are highly localised, whose spin degree of freedom is then coupled to the conduction electrons in the system. The resulting Hamiltonian contains both fermion and spin operators. The richness in the effective low-energy descriptions in turn leads to a plethora of exotic ordered states at low energy. The quantum fluctuations of the dominating interactions can then tune the system through various kinds of quantum phase transitions, whose criticality and universality are intriguing both theoretically and experimentally.

1.1 Dirac electrons in graphene

The electrons in graphene are an example of where the interesting physics mainly lies in the charge channel. Graphene is a two-dimensional single layer of carbon atoms sitting on a honeycomb lattice, as shown in Fig.1.1. The simplest way of obtaining a single-layer graphene is to exfoliate it from graphite by a tape. Though it has been more than two decades since its first discovery, graphene remained one of the most popular 2d materials in research until today. Despite the simple structure, various physics can be found in it, such as massless Dirac fermions [12] and

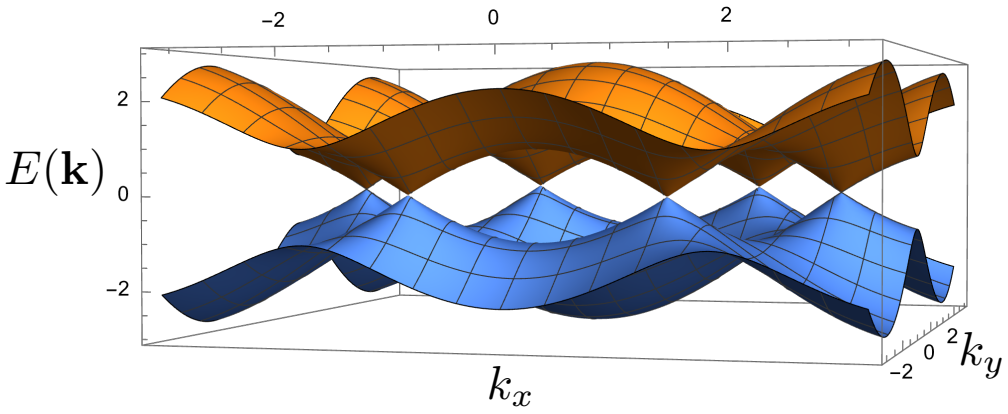

Figure 1.2: The energy dispersion of electrons in graphene. Six Dirac points with linear band touching appear at the corners of the Brillouin zone.

anomalous quantum Hall effect [13]. Then more recently, it was realised that a new layer of richness in physics can simply be added to the system by putting a second layer on top of the single layer - the discovery of flat bands and unconventional superconductivity in twisted double-layer graphene has stimulated the idea of 'twistronics'[14].

Here we focus on the Dirac fermions in graphene. The electrons on the outer shell that contribute to the conductivity are from the s and three p orbitals, therefore the low energy microscopic model is just electrons on a honeycomb lattice at half-filling. This is simply a single-particle Hamiltonian written as

$$H = -t\sum_{\mathbf{r}}\sum_{j=1,2,3}\left(c_A^{\dagger}(\mathbf{r})c_B(\mathbf{r}+\delta_j)+H.c.\right), \boldsymbol{\delta} = (0,\boldsymbol{a_1},\boldsymbol{a_2}) \tag{1.2}$$

where t is the hopping strength between nearest neighbor sites, and $\boldsymbol{a_1},\boldsymbol{a_1}$ are the lattice vectors. The single particle Hamiltonian can be simply diagonalized by Fourier transforming to the momentum space, giving rise to the energy dispersions:

$$E_{\pm}(\mathbf{k}) = \pm t\sqrt{3+4\cos(\frac{3k_x}{2})\cos(\frac{\sqrt{3}k_y}{2})+2\cos(\sqrt{3}k_x)} \quad , \tag{1.3}$$

and the electronic band dispersion is shown in fig.1.2. It is evident that

there are zero energy solutions at the two equivalent high symmetry points $K^{(\prime)} = \pm 4\pi/3\sqrt{3}(1,0)$, which correspond to the so-called valley degree of freedom. One can then zoom in and expand the dispersions around one of the zero-energy points, which in turn gives linear dispersion $E(\mathbf{k}) = v_F |\mathbf{k}|$. The linear dependence in momentum indicates the emergent Lorentz invariance at the $K(K')$ points, and the corresponding fermions are Dirac fermions. The relativistic nature of the Dirac fermions arouses broad interests both theoretically and experimentally. It makes a perfect playground to study high energy physics like QED_3, and the linear dispersion guarantees ballistic transport of electrons which has huge potential in the semiconductor industry. From the point of this thesis, the Dirac fermions are perfect since they are low-energy fermionic excitations with only a point-like Fermi surface at half-filling.

1.2 Quantum Spin liquids

The spin degree of freedom is the origin of magnetism in materials. Normally, the rotation symmetry of spins is broken at low temperatures, forming ground states with long-range magnetic order like ferromagnetism, antiferromagnetism, nematic and stripe orders. However, there are rare cases in which the spins remain disordered even at zero temperature due to frustrations. Such exotic ground states, dubbed quantum spin liquids (QSL), are a type of symmetry-enriched topologically ordered state. The idea was first proposed by Phil Anderson as a related problem in explaining high-temperature superconductivity [15, 16, 17], which considered a ground state with a combination of paired spin singlets. The resonating valence bond (RVB) state was later joined by a family of other spin-disordered ground states. The common properties among them are the emergent gauge fields and fractionalised quasiparticles. For example, the ground state of a $J_1 - J_2$ Heisenberg model on a triangular/kagome lattice could be a spin liquid with spinon excitations[18, 19, 20, 21], and one of the main characters of this thesis, the Kitaev model [22], has a ground state with emergent Z_2 gauge fields and relativistic Majorana fermions.

Though theorists have predicted QSL states in some materials [23, 24, 25, 26,

27, 28, 29, 30], the experimental confirmation remains elusive [31]. This is mainly due to the competition between a magnetic order and a QSL state. It is thus important to study the stability of a QSL against different types of spin interactions, and the nature of the phase transition to magnetically ordered phases. Furthermore, a phase transition between a QSL and an ordered phase could be described by a theory of the emergent quasiparticles and the gauge fields, giving rise to exotic quantum criticality like QED_3 [32, 33, 34, 35, 36, 37] and fractionalised criticality [38].

1.3 Kondo physics

The origin of the study of Kondo physics can be dated back to the 1930s when the resistivity of Au was shown experimentally to increase as the temperature decreased at very low temperatures [39]. The observation was puzzling, as in a metal one expects the resistivity to be proportional to T^2, which is a result of low energy electron-electron scattering. Only thirty years later, the inverse temperature dependence was found to be a product of the magnetic nature of the materials - the localised electrons scatter the conduction electrons strongly at low temperatures, even if the impurity concentration is very low. The physics of mobile electrons interacting with localised spins was then dubbed 'Kondo physics', named after the Japanese physicist who proposed the idea of impurity scattering of electrons.

In Kondo's calculation [40], he came up with the simplest effective model by considering only a single impurity in a conduction band. The Hamiltonian reads

$$H = \sum_{\mathbf{k}\sigma} \varepsilon_{\mathbf{k}\sigma} c^{\dagger}_{\mathbf{k}\sigma} c_{\mathbf{k}\sigma} + J_K \mathbf{S}(\mathbf{0}) \cdot \mathbf{s}, \tag{1.4}$$

where $\mathbf{S}(\mathbf{0})$ is the impurity spin at the origin, and $\mathbf{s}$ the spin of conduction electrons. With the perturbation theory up to 3rd order, he showed that the resistivity of such a model has a minimum at a certain temperature scale T_K that depends on the exponential of the electron-impurity interaction strength J, $T_K \propto e^{\frac{1}{-2\rho J}}$, after which the resistivity blows up to infinity at zero temperature. The temperature scale T_K is now called the Kondo temperature, which in real materials could range from a few Kelvins to a hundred due to its exponential nature. The diverging resistivity at

the lowest temperature is of course unphysical, but it nevertheless contains important hints to what's really happening: The Kondo effect is non-perturbative which cannot be understood by a finite order perturbative expansion.

The understanding of the physics below the Kondo temperature was then pushed forward by Phillip Anderson, who proposed that the Kondo problem can be viewed as a scaling problem [41]. By performing the well-known 'poorman's scaling', he derived the renormalisation of the Kondo interaction strength J, which flows to infinity in the IR limit, indicating the non-perturbative nature of the problem. The idea of coarse-graining the system by integrating out the high energy fluctuations around the Fermi surface shares the very spirit of the renormalisation group (RG). Later, Kenneth Wilson came up with a numerical approach to systematically approach the low-energy Kondo physics in a non-perturbative way, dubbed the numerical renormalisation group (NRG) [4, 5]. It is well understood that at low temperatures, the conduction electrons form a cloud to screen the impurity spin. Depending on the number of conducting channels (bands) and size of the impurity spin, the system could either be overscreened or underscreened, and the rest of the system mainly determines the low energy physics after the screening.

1.4 Outline of the Thesis

This thesis focuses on the exotic fluctuation-induced phases in Kondo materials and Kitaev quantum spin liquids and the nature of the associated quantum phase transitions. The central idea is to use a renormalisation group to study the universality of continuous quantum phase transitions beyond the conventional Ginzburg-Landau-Wilson paradigm, more precisely, the fermion-induced quantum criticality due to the presence of Fermi surfaces.

In Chapter 2, we first introduce the general techniques of Ginzburg-Landau order parameter theory and Wilson's momentum-shell renormalisation group, with an emphasis on the physical idea of the universality of continuous phase transitions rather than the detailed maths. As an example, we then study the renormalisation of the simple model, the ϕ^4 theory, where the order parameter fields ϕ are scalar

fields. After that, cases where the low-energy effective theory cannot be represented simply by a pure order parameter theory are motivated, revealing the necessity of going beyond the Ginzburg-Landau-Wilson paradigm. We show that starting from the low energy theory of electrons in graphene, we naturally arrive at the so-called family of fermion-induced quantum criticality, which could be described by the Gross-Neveu-Yukawa (GNY) theory.

In Chapter 3, starting with the origin where the idea of renormalisation group was first introduced into condensed matter physics, we scrutinize an anisotropic Kondo model by perturbative and numerical renormalisation group, to explain the magnetic moment reorientation observed in many Kondo lattice materials. We show that the interplay between the anisotropic Kondo coupling and single-ion anisotropy can lead to a non-trivial RG flow where the single-ion anisotropy changes signs in certain parameter regimes, indicating a crossing of magnetic susceptibilities along different directions. Such interplay of quantum fluctuations could explain the metamagnetic phase transition in many Kondo materials.

Then in Chapter 4 we apply the modern momentum-shell renormalisation group to a honeycomb model, where the local moments are connected to the itinerant electrons with Dirac fermions through Kondo interaction, as our first example of Dirac fermion-induced quantum criticality. We examine the impact of Dirac electrons on the Néel quantum critical point. The results suggest that the Néel criticality is quasi-stable against the screening effect from particle-hole fluctuations in certain parameter regime, outside of which the anti-ferromagnetic order is destroyed by the Kondo fluctuation. This illustrates the exotic criticality one can find in systems with gapless fermions.

Chapter 5 and 6 is dedicated to the more exotic case of Kitaev honeycomb lattice, where the ground state is a gapless Z_2 quantum spin liquid with emergent relativistic Majorana fermions. In Chapter 5, We first use different fermion representations to study the phase diagram of the Kitaev model in the presence of Ising interaction, and show that the phase transition between the gapless and gapped QSL can also be induced by short-range magnetic interactions. The topological phase transi-

tion is very similar to the semimetal-insulator transition that happens in graphene, suggesting the low-energy theory is again GNY-like. Hence, in the Chapter 6, we start from the microscopic Kitaev-Ising model to derive the effective field theory of such topological phase transition. The nature of the transition is then shown to be a GNY theory of Majorana fermions with semi-Dirac dispersion, in analogy to the case of complex fermions. The criticality of the topological phase transition in the Kitaev-Ising model corresponds to a new universality class of Majorana fermions.

At last, in Chapter 7, we summarise and conclude the general results and remark on future research directions.

Chapter 2

Phase Transitions and Renormalisation Group

In this chapter, we briefly introduce the main tools for studying the critical behavior of phase transitions: the Ginzburg-Landau-Wilson paradigm which describes conventional symmetry-breaking phase transitions in gapped electron systems, and the Gross-Neveu-Yukawa theory which describes the ones in gapless electron systems. Note that the aim of this introduction is not to be exhaustive but self-contained. There are already detailed and well-structured reviews and notes on the topics, and interested readers will be pointed to the related materials when appropriate.

2.1 Ginzburg-Landau theory and Universality

The first general phenomenological view of phase transitions is based on the concept of order parameters, which describes symmetry-breaking phase transitions. In the ordered phase of such a transition, a certain symmetry of the Hamiltonian is spontaneously broken, resulting in a ground state without such a symmetry. Depending on the microscopic details of the systems, a phase transition can happen at different parameters. However, for any symmetry-breaking phase transition, one can define an order parameter ϕ which is an observable that takes zero in the disordered phase and becomes finite in the ordered one. For example, for a ferromagnetic phase transition, the order parameter is the magnetization, and for a charge density wave state, the order parameter is the difference in fermion number density between

sites. The nature of an order parameter depends on the specific phase transition to study, it could be a scalar, a vector or a tensor. Since we are only interested in the long-wavelength collective behavior of the system, it is natural to coarse-grain the system by going to the continuum limit and leaving out the details of the lattice. In this way, the order parameter becomes a field $\phi(x)$ defined in real space. In the vicinity of the critical point, one can then write down a general field theory of the order parameter fields to describe the thermodynamic behavior of the system:

$$F = \int dx[a\phi(x)^2 + b\phi(x)^4 + \cdots \\ + c(\nabla\phi(x))^2 + d((\nabla^2\phi(x))^2) + f\phi(x)^2(\nabla\phi(x))^2 + \cdots], \tag{2.1}$$

which is known as the Ginzburg-Landau free energy. Though the phenomenological parameters $(a, b, \cdots)$ depend on the microscopic details, the form of the expression is only constrained by the symmetry and dimensionality of the system. This already suggests the possibility of some hidden universality behind different phase transitions.

The partition function can be written as a functional integral of the order parameter fields:

$$Z = \int \mathscr{D}\phi(x) e^{-F[\phi(x)]}, \tag{2.2}$$

which is in general hard to evaluate. However, one can consider a mean-field approximation of the free energy by considering only the saddle-point solution of the functional integral $F_{mf} \simeq \min[F[\phi(x)]]$, which has the greatest contribution in the Boltzmann factor according to the least action principle. We here consider the case where $c > 0$, in which the saddle-point solution is simply a uniform distribution of $\phi(x) = \phi$. This for example corresponds to the ferromagnetic phase transition of an Ising magnet. Near the ferromagnetic phase transition, the free energy density can be well approximated by only the lowest powers in the expansion,

$$f_{mf} \equiv \frac{F_{mf}}{V} = a\phi^2 + b\phi^4, \tag{2.3}$$

whose behavior mainly depends on the sign of a. For $a > 0$, the minimum of f_{mf} occurs at the origin, suggesting the system is paramagnetic. If $a < 0$, the minima take finite values of ϕ when $b > 0$, which corresponds to the symmetry-broken ferromagnetic ground state.

The above treatment gives the classical effective field theory to describe the phase transition. It is straightforward to extend to a quantum phase transition by rewriting the quantum statistical partition function $Z = \mathrm{Tr} e^{-\beta H}$ into the path integral formalism

$$Z = \int \mathscr{D}\phi(x,\tau) e^{-S[\phi]}, \tag{2.4}$$

where

$$S[\phi] = \int_0^\beta d\tau \int dx \, [a\phi(x)^2 + b\phi(x)^4 + \cdots]. \tag{2.5}$$

The imaginary time $i\tau := \beta$ here can be viewed as a Wick rotation of the axis, which represents the Boltzmann weight as an imaginary time evolution operator. In this way, a d-dimensional quantum field theory corresponds to a classical field theory in $d+1$ dimensions [42]. In the rest of the thesis, we will use the imaginary time path integral formalism only. The equivalence of the temporal and spatial integrals is salient when one works at $T = 0$.

With the partition function known, one can utilise it to calculate the behaviors of all physical observables near the critical point. For more details, readers are asked to consult [43]. At the critical point of a continuous phase transition, quantities like correlation length and susceptibility diverge as a power law of the temperature. The powers form a set of critical exponents which uniquely determine the nature of the phase transition. The values of the exponents are determined by the symmetry and dimensionality of the problem only, regardless of the microscopic details, which leads us to one of the keystones of the modern theory of phase transitions: Universality. Though qualitatively convincing, one would expect the critical exponents obtained by the mean-field treatment to be wrong quantitatively, as the fluctuation of the order parameter fields is neglected. However, the speculation is only partly true, as there exists a lower critical dimension in which a phase transition can-

not happen. For example, the Mermin-Wagner theorem proves that a spontaneous symmetry-breaking phase transition cannot happen in two or lower dimensions if the symmetry is continuous [44]. Furthermore, there also exists an upper critical dimension in which the mean-field theory is exact. This can be understood easily in the next section after introducing the renormalisation group.

The Landau-Ginzburg theory tells us that a phase transition can be understood by an effective theory of the order parameter. Different phase transitions with the same symmetry and dimensionality might belong to the same universality class, sharing the same set of critical exponents. However, such phase transitions can happen in drastically different length/energy scales. This seems to suggest the theory is scale-invariant. Also, how can one systematically include the fluctuation of the order parameter in the calculation to make quantitative predictions beyond mean-field theory? In order to answer these questions, another puzzle piece named the renormalisation group is needed.

2.2 Perturbative Renormalisation Group

The concept of renormalisation group was first introduced to tackle the ultraviolet divergences in high-energy physics in 1950s [45]. When calculating physical quantities with quantum field theory, one naturally encounters the problem that the momentum integral diverges at $k \to \infty$, as the integrand is a function of k. This cannot be the case as the quantities are finite experimentally. To reconcile the disaster of infinity, one needs to introduce a cutoff Λ to the integration range. The backfire of such practice is that the physical observables will now become Λ-dependent, but the dependence of Λ can be absorbed by a redefinition of the coupling strengths. This is the core concept of the renormalisation group. At first, the treatment was only regarded as a compromise to get meaningful results. The underlying physical meaning of RG was only clearer after its introduction to condensed matter physics by Kandanoff [46] and Wilson [4, 5].

From a modern perspective, the cutoff in length/energy indicates the scale where the effective theory breaks down. In condensed matter physics, the natural

cutoff corresponds to the size of a unit cell. Within the range where the effective theory is valid, one can coarse-grain the system by eliminating the high-energy (short-range) fluctuations, and the coupling parameters in the bare theory start running. By doing so iteratively, one relates the bare theory at the original high-energy (short wavelength) scale to a theory with a different set of parameters at a lower energy (long wavelength) scale. The coupling parameters will flow to some asymptotic values, where the theory becomes scale invariant. Such a fixed point corresponds to the critical point of a continuous phase transition. This is the reason why phase transitions at different scales exhibit exactly the same behavior of divergence when approaching the critical point. At the critical point of a continuous phase transition, the correlation length diverges, and the system has no characteristic length scale, therefore the theory looks completely the same for all scales.

2.2.1 Renormalisation group transformation

Here we briefly introduce the procedure of the perturbative RG transformation in momentum space. Detailed derivation can be found in [4, 47]. In general, we are interested in the partition function

$$Z = \int \mathscr{D}\phi(\omega,k) e^{-S[\phi(\omega,k)]}. \tag{2.6}$$

Note that this is just the Fourier transformed version of the quantum field theory in frequency-momentum space, where ω is the Matsubara frequency. There are three steps: First, for a system with cutoff Λ, we perform an infinitesimal scale transformation of the frequency-momentum coordinates:

$$\omega' = \omega e^{-zd\ell}, k' = k e^{-d\ell}, \tag{2.7}$$

where z is called the dynamical exponent which tracks the scaling of the imaginary time. Second, we split the modes into fast ($\phi_> = \phi(k), \Lambda e^{-dl} \leq k \leq \Lambda$) and slow ($\phi_< = \phi(k), 0 < k < \Lambda e^{-dl}$) modes. The action can then be written as $S[\phi_<, \phi_>] =$

$S_0[\phi_<] + S_0[\phi_>] + S_I[\phi_>, \phi_<]$, and the partition function

$$\begin{aligned} Z &= \int \mathscr{D}\phi_< \mathscr{D}\phi_> e^{-S_0[\phi_<]} e^{-S_0[\phi_>]} e^{-S_I[\phi_>,\phi_<]} \\ &= \int \mathscr{D}\phi_< e^{-S_0[\phi_<]} \mathscr{D}\phi_> e^{-S_0[\phi_>]} e^{-S_I[\phi_>,\phi_<]} \\ &\equiv \int \mathscr{D}\phi_< e^{-S'[\phi_<]}, \end{aligned} \tag{2.8}$$

where the effective action S' can be written as

$$\begin{aligned} e^{-S'[\phi_<]} &= e^{-S_0[\phi_<]} \int \mathscr{D}\phi_> e^{-S_0[\phi_>]} e^{-S_I[\phi_>,\phi_<]} \\ &= e^{-S_0[\phi_<]} \frac{\int \mathscr{D}\phi_> e^{-S_0[\phi_>]} e^{-S_I[\phi_>,\phi_<]}}{\int \mathscr{D}\phi_> e^{-S_0[\phi_>]}} \int \mathscr{D}\phi_> e^{-S_0[\phi_>]} \\ &= e^{-S_0[\phi_<]} \langle e^{-S_I[\phi_>,\phi_<]} \rangle_{0,>}. \end{aligned} \tag{2.9}$$

The notation $\langle \ \rangle_{0,>}$ stands for the average with respect to the fast modes. This allows us to describe the physics of the slow modes by 'integrating out' the fast modes. However, a theory obtained by the above procedure will have a different cutoff and thus not directly comparable to the bare theory. A final step that rescales the frequency and momenta back to the original cutoff is needed. In addition, there could be some mathematical redundancy as the action can have an overall factor that does not affect any of the physics after renormalisation. Such redundancy can be lifted by rescaling ϕ and fixing the quadratic term from flowing. This point will be clearer in the next section when the RG of the scalar ϕ^4 theory is shown.

One notion related to the rescaling of ϕ is the scaling dimension of an observable $\hat{O}$. In general, any operator can be written as a function of the momenta $\hat{O}(k)$, thus by rescaling the momenta, the operator also gains a nontrivial scaling $\hat{O}' = \hat{O} e^{[\hat{O}]d\ell}$. The scaling dimension $[O]$ characterises the importance of the operator under RG. If $[\hat{O}] > 0$, the term is relevant under RG, as the coupling strength of such term will increase under RG. If $\hat{O}$ is negative, the operator is regarded as irrelevant as the coupling strength flows to zero. Extra care must be taken to handle the marginal case in which $[\hat{O}] = 0$, as the diagrammatic contribution by the

RG calculation could either render the operator relevant or irrelevant. Now we are at the stage to understand the unexplained origin of the upper critical dimension where the mean-field theory is exact. The scaling dimension of operators obviously will depend on the dimensionality of the problem. As the dimension increases, the operators in general become more and more irrelevant, until a point where all the operators that describe interactions in the system are rendered irrelevant. The remaining theory under RG will be a free theory of ϕ, whose behavior can be fully captured by the mean-field theory.

The RG method maps the theory at some scale to a theory with different coupling strengths at a new scale. Through RG one effectively coarse-grains the theory, zooming into the low-energy physics, and rescaling the low-energy sector back to the original cutoff to keep track of the flows of the parameters until they reach a fixed point. Since in the RG process one loses the information from the fast modes sector, the mapping is not bijective, meaning the 'renormalisation group' is not strictly a group, but a semi-group. In any case, the sloppiness in the nomenclature cannot hide the power of RG, especially in the study of quantum criticality.

Before diving into the RG of a scalar order parameter theory, we comment on the perturbativity of the momentum-shell RG scheme introduced above. Since we are only interested in calculating $\langle e^{-S_I[\phi_>,\phi_<]}\rangle_{0,>}$, one can expand out the exponential and calculate the contributions order by order, diagrammatically this means to sum up the contribution of all the possible linked Feynman diagrams. The integrals to be worked out are all defined on a frequency-momentum shell, which suggests the integrals are rather simple if there is full rotational symmetry. This seems to give an unrealistic illusion that the $\langle e^{-S_I[\phi_>,\phi_<]}\rangle_{0,>}$ can be worked out easily with precision up to any order. Unfortunately, this is not the case as any Feynman diagrams involving more than one loop cannot be worked out simply on-shell. One will have to integrate over the real axis to get the higher-order contributions. With this said, ideally we need a small parameter in the theory like always. Expanding in the orders of the small parameter might give us analytic control for results even in one-loop order. Finding a small parameter is not always possible as the problems

we are interested in are in the strong interaction regime. Fortunately, the fact that the expansion we do is mostly asymptotic expansion helps.

Two common methods are used to control the expansion. The first is the so-called ε-expansion proposed by Wilson, in which he utilised the advantage of the exactness of mean-field theory in the upper critical dimension. One can take the continuum limit of the dimensionality and introduce a small deviation ε in the dimensionality away from the upper critical dimension. Then the RG corrections will be in orders of ε. Another more traditional way is to introduce a large number of flavors to the fields considered. The theory will then contain a sum over the field flavors, which blows up when $N \to +\infty$. To get around this and maintain the scale invariance of some coupling g, one needs to define the coupling as $g \sim O(1/N)$. Therefore in the large-N limit, the coupling strength becomes perturbative and the expansion is controlled in orders of $1/N$. In the remainder of the thesis, we will utilise these two methods to control the calculation.

2.2.2 Simple Example: ϕ^4 Theory

We now perform an RG analysis of a simple theory that has only a scalar order parameter. Such a ϕ^4 theory can be used to describe a phase transition with a broken Z_2 symmetry. The partition function in the d-dimensional k-space can be written as

$$Z = \int \mathscr{D}\phi(\mathbf{k}) e^{-S[\phi(\mathbf{k})]}, \tag{2.10}$$

where the action has the form

$$S = S_\phi + S_I, \tag{2.11}$$

$$S_\phi = \frac{1}{2}\int_0^\Lambda \frac{d^d\mathbf{k}}{(2\pi)^d}\phi(\mathbf{k})(k^2+m^2)\phi(\mathbf{k}), \tag{2.12}$$

$$S_I = \lambda \int_0^\Lambda \prod_{i=1,2,3,4} \frac{d^d\mathbf{k}_i}{(2\pi)^d}\phi(\mathbf{k}_1)\phi(\mathbf{k}_2)\phi(\mathbf{k}_3)\phi(\mathbf{k}_4)\delta(\mathbf{k}_1+\mathbf{k}_2+\mathbf{k}_3+\mathbf{k}_4). \tag{2.13}$$

where $\mathbf{k} = (\omega \equiv k_0, k_1, k_2, \cdots, k_{d-1})$ is the d-dimensional frequency-momenta, and $k = |\mathbf{k}|$, and m^2 is the mass term.

2.2.2.1 Tree Level Scaling

Before attacking $\langle e^{-S_I[\phi_>,\phi_<]}\rangle_{0,>}$, we first look at the tree level scaling. As defined in the previous section, the momenta are rescaled as $\mathbf{k}' = \mathbf{k}e^{-d\ell}$. Note that here $z = 1$ as the frequency is equivalent to the momenta. To get the scaling dimension of ϕ, we fix the quadratic term from flowing: $2[\phi] + d + 2 = 0 \Rightarrow [\phi] = -(d + 2)/2$. The scaling dimension of the mass term is then $[m^2] = d + 2[\phi] = 2$, which suggests that the mass m^2 is relevant under RG. Similarly, we can work out the scaling dimension of the quartic coupling strength $[\lambda] = 3d - 4[\phi] = 4 - d$. (One needs to be careful as the d-dimensional delta function has dimension $-d$.) That is to say, for $d > 4$, the quartic interaction is irrelevant under RG. This provides an upper bound on the dimensionality in which the theory remains interacting. At 'upper critical dimension' $d = 4$, the effective theory is just a free theory of the order parameter, which provides a mounting point for us to perform a $4 - \varepsilon$ expansion.

One may ask why the higher-order terms in ϕ are neglected. The answer also lies in the tree-level scaling: As we can observe in the above calculation of scaling dimensions, higher order terms in ϕ are less and less relevant since $[\phi] < 0$. Since for $d = 4$, the quartic term is already marginal, higher-order terms will for sure be irrelevant under RG. For a similar reason, the coupling λ is just a constant rather than a function of $\mathbf{k}$. In general, the coupling is a function of the momenta $\lambda(\mathbf{k})$, which can be expressed as a Taylor series in $\mathbf{k}$: $\lambda(\mathbf{k}) = \lambda_0 + \lambda_2\mathbf{k}^2 + O(\mathbf{k}^4)$, and only the constant term is relevant under RG.

2.2.2.2 One Loop Corrections

The key is to expand out $\langle e^{-S_I[\phi_>,\phi_<]}\rangle_{0,>}$ to get a series of n-point functions:

$$\langle e^{-S_I[\phi_>,\phi_<]}\rangle_{0,>} = \langle \sum_{n=1}^{\infty} \frac{(-1)^n S_I^n}{n!} \rangle_{0,>}^{\text{1PI, con.}} \equiv \delta S[\phi_<] \tag{2.14}$$

Each order of the expansion corresponds to a set of Feynman diagrams with n external ϕ fields. Fortunately, the so-called linked-cluster theorem suggests that only the connected (con.) one particle irreducible (1PI) diagrams have non-zero contributions, which help eliminate most of the diagrams in the expansion.

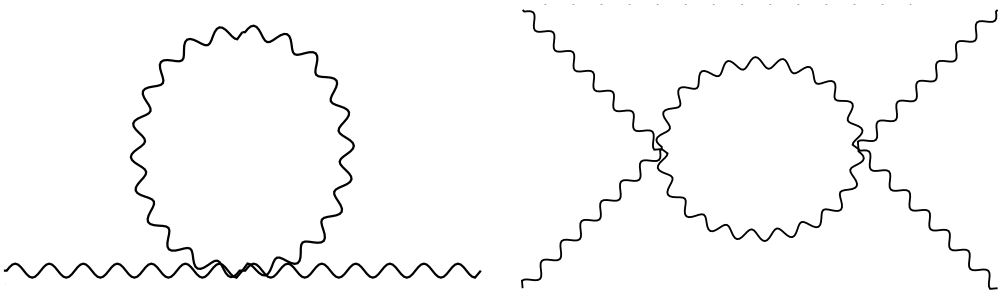

Figure 2.1: One-loop diagrams of the ϕ^4 theory. The diagram on the left corrects the bosonic self-energy, and the one on the right corrects the ϕ^4 interaction strength λ.

In one-loop order, the correction is simply

$$\delta S = \langle S_I \rangle_{0,>} - \frac{1}{2}\langle S_I^2 \rangle_{0,>}, \tag{2.15}$$

which corresponds to the two Feynman diagrams shown in Fig.2.1. The first diagram corrects the boson propagator and mass, and the second term corrects the quartic coupling strength λ.

In order to calculate the diagrams one needs to make use of the bosonic propagator

$$\langle \phi(\mathbf{k})\phi(\mathbf{q}) \rangle = G_\phi(\mathbf{k})\delta(\mathbf{k}+\mathbf{q}) = \frac{\delta(\mathbf{k}+\mathbf{q})}{k^2+m^2}, \tag{2.16}$$

which defines the contraction rule of the fields. The diagram that corrects the quadratic propagator gives

$$\begin{aligned} \langle S_\lambda \rangle &= 6\lambda \int_{\Lambda e^{-d\ell}}^{\Lambda} \frac{d^d\mathbf{q}}{(2\pi)^d} G_\phi(\mathbf{q}) \int_0^{\Lambda e^{-d\ell}} \frac{d^d\mathbf{k}}{(2\pi)^d} \phi(\mathbf{k})^2 \\ &= 12 S_d \frac{\Lambda^d d\ell}{\Lambda^2+m^2}\lambda \times \frac{1}{2}\int_0^{\Lambda e^{-d\ell}} \phi(\mathbf{k})^2. \end{aligned} \tag{2.17}$$

The factor of 6 in the first line is the combinatorial factor from the equivalent ways of contractions. Since the high-energy modes to be integrated out are on the momentum shell $\Lambda e^{-d\ell} < |\mathbf{q}| < \Lambda$, the integral can be done by simply switching to the spherical coordinates. $S_d = 2\pi^{d/2}/(\Gamma(d/2)(2\pi)^d)$ is the surface area element of a $d-$sphere. The shell integral leaves no dependence on the external momenta $\mathbf{k}$,

therefore it only corrects the mass m^2. The second diagram in Fig.2.1 corrects the quartic interaction, which evaluates to

$$-\frac{1}{2}\langle S_\lambda^2\rangle = -36S_d\frac{\Lambda^d d\ell}{(\Lambda^2+m^2)^2}\lambda^2\int^<_{\mathbf{k}_1,\mathbf{k}_2,\mathbf{k}_3}\phi(\mathbf{k}_1)\phi(\mathbf{k}_2)\phi(\mathbf{k}_3)\phi(-\mathbf{k}_1-\mathbf{k}_2-\mathbf{k}_3). \tag{2.18}$$

2.2.2.3 RG Equations and Fixed Points

The RG scaling equations of the parameters can be derived by combining the tree-level scaling and the diagrammatic corrections, which leads to

$$\frac{dm^2}{d\ell} = 2m^2 + 12S_d\frac{\Lambda^d}{\Lambda^2+m^2}\lambda, \tag{2.19}$$

$$\frac{d\lambda}{d\ell} = (4-d)\lambda - 36S_d\frac{\Lambda^d}{(\Lambda^2+m^2)^2}\lambda^2. \tag{2.20}$$

The RG equations are differential equations of the parameters with respect to the 'time step' ℓ. The parameters flow to some fixed point as the time step goes to infinity, or in other words, the system goes to the long-wavelength limit. Recall that we only took the first order (one-loop) term in the cumulant expansion when calculating the diagrammatic corrections. This is only justified by doing an ε-expansion around the upper critical dimension $d_* = 4$. Substituting $d = 4-\varepsilon$ into the RG equations and solving for the fixed points where $dm^2/d\ell = 0$ and $d\lambda/d\ell = 0$, one gets two sets of solutions: $(m_*,\lambda_*) = (0,0)$ and $(m_*,\lambda_*) = (-\Lambda^2\varepsilon/6, 2\pi^2\varepsilon/9)$. The RG flow of the parameters and the fixed points are shown in Fig.2.2. The origin is the Gaussian fixed point where all the interaction vanishes and the left theory is simply a free theory of massless bosons. This fixed point is unstable, as an infinitesimal perturbation will drive the parameters to flow away from this fixed point. The nontrivial fixed point at finite values of m^2 and λ is called the Wilson-Fisher fixed point, which is an interacting fixed point that governs the symmetry-breaking phase transition described by the ϕ^4 theory.

The subtlety of the above derivation is that we perform the integration of the high-energy modes over a frequency-momenta shell. In principle, the frequency integral should be done on the whole real axis. However, it can be shown that the

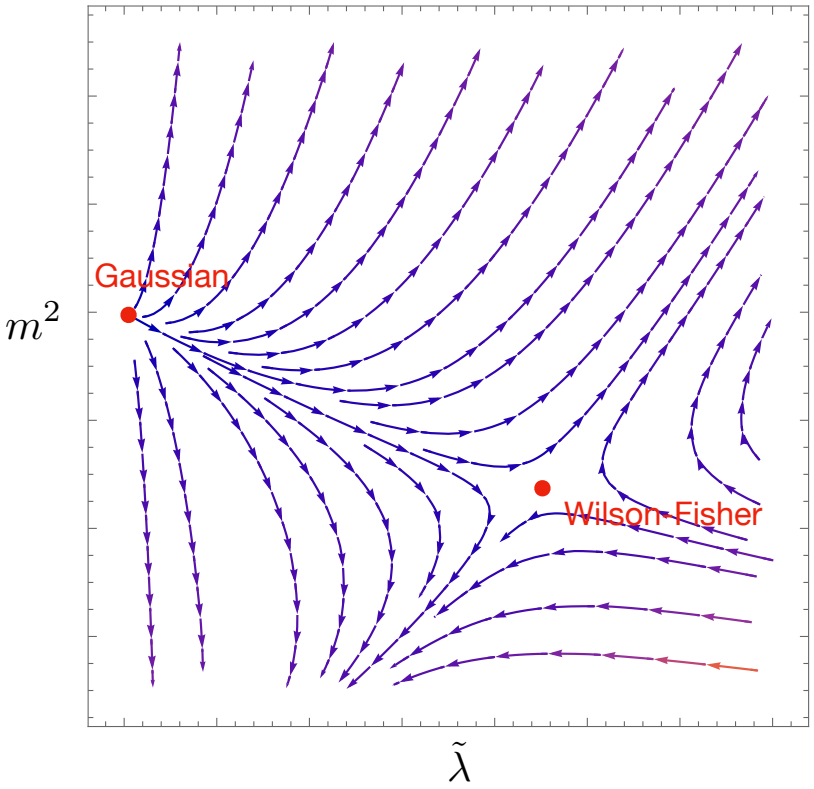

Figure 2.2: RG flow of the parameters. The Gaussian fixed point at the origin corresponds to the free theory without any interactions. It is unstable against infinitesimal perturbations. The Wilson-Fisher fixed point, on the other hand, is an interacting fixed with finite values of m^2 and $\tilde{\lambda}$.

nature of the fixed points is insensitive to the cutoff scheme used in RG, though the exact values of the coupling parameters at the fixed points will.

2.3 From Graphene to Gross-Neveu-Yukawa Theory

The Ginzburg-Landau-Wilson paradigm provides a compact way to understand continuous phase transitions at a phenomenological level. In a gapped electron system, using a pure order parameter theory to describe a symmetry-breaking phase transition makes perfect sense, as the only low-energy degree of freedom is the bosonic order parameter field. However, as mentioned in the Introduction, there are cases where the GLW paradigm fails, which include topological phase transitions in which no symmetry is spontaneously broken, and fermion-induced quantum criticality where the fermions are gapless and hence cannot be integrated out in the

low-energy theory. The difference is that, for a topological phase transition, usually no order parameter can be defined as the symmetry remains untouched, while for fermion-induced criticality, the fermions can simply be added on top of a symmetry-breaking phase transition.

On the other hand, RG can also be used in other scenarios without phase transitions. After all, when first proposed, RG was used to explain the low-energy physics of the single-impurity Kondo problem, where there's no phase transition at all. In general, one can use RG as a tool to extract the low-energy physics of an interacting system away from the exactly solvable point. Examples are to study the transport property in low dimensions [48, 49, 50], or to compare the relevance of different fermion interactions and the corresponding instability susceptibilities and decide which instability wins [51, 52, 53]. Since we are interested in strongly correlated electron systems, it is natural to consider RG for fermions instead of the bosons in an order parameter theory.

Here we leave out the details of introducing the fermionic RG and only point the interested readers to this review [47], as in the next chapter we will use perturbative RG to face its primaeval archenemy in condensed matter physics, for which the method was designed: an anisotropic Kondo model. The RG used there is merely a slightly more complicated version of the original design, therefore by itself instructive and tractable. The main difference to bear in mind is the Grassmann algebra of the fermionic field operators which gives the right anti-commutation relation of the fermions [42].

2.3.1 Phase Transitions in Graphene: Dirac Fermion-induced Quantum Criticality

How do we describe a symmetry-breaking phase transition if the electron dispersion is gapless? We need an order parameter theory for the phase transition while keeping track of the fermions, as they are crucial to the correct low-energy physics. Such a resulting low-energy theory includes three types of interaction: the lowest order fermion-fermion interactions, boson-boson interactions, and a Yukawa interaction that couples the fermions and bosons. In order to study the low-energy fluctuations

of the fermions, we expand the momentum around the Fermi surface. The RG will then rely on the shape of the Fermi surface, as accounted for in [47]. To ease the pain we want a Fermi surface as simple as possible, which makes the half-filled Dirac semimetals with a point-like Fermi surface a perfect candidate.

2.3.1.1 Hubbard-Stratonovich Transformation

In real materials, the electrons are usually subject to long-range Coulomb interactions. If metallic then the fermion fluctuations near the Fermi surface will screen the Coulomb interaction, giving rise to an effective short-range interaction. If one only considers nearest neighbor interactions in graphene, the Hamiltonian can be written as

$$\hat{H} = -t \sum_{\langle i,j \rangle} (c_i^\dagger c_j + \text{h.c}) + U \sum_{\langle i,j \rangle} \hat{n}_i \hat{n}_j. \tag{2.21}$$

Recall that the low-energy theory near the Fermi surface is described by relativistic Dirac fermions. In the continuum limit, this gives rise to a Gross-Neveu model[54], which in the path integral form reads

$$\begin{aligned} S =& S_0 + S_I, \\ S_0 =& -i \int_r \bar{\boldsymbol{\psi}}(\tau, \mathbf{r})(\partial_\tau \sigma_0 \otimes \tau_0 + v_F \boldsymbol{\partial} \cdot \boldsymbol{\sigma} \otimes \tau_z) \boldsymbol{\psi}(\tau, \mathbf{r}), \qquad (2.22) \\ S_I =& 4U \int_{r_1, r_2, r_3, r_4} \bar{\boldsymbol{\psi}}_A(r_1) \tau_0 \boldsymbol{\psi}_A(r_2) \bar{\boldsymbol{\psi}}_B(r_3) \tau_0 \boldsymbol{\psi}_B(r_4), \qquad (2.23) \end{aligned}$$

where $\boldsymbol{\psi}$ are Dirac fermion fields, and $r = (\tau, \mathbf{r})$ is the $d+1$ dimensional space-time coordinates. σ, τ are Pauli matrices corresponding to the spin and sublattice degrees of freedom. As the interaction becomes stronger, the electrons on the honeycomb lattice will go through a phase transition from a Dirac semimetal to a charge density wave (CDW) insulator. In the CDW phase, a net difference in electron density on the sublattice sites is established, corresponding to chiral symmetry breaking. The order parameter of the CDW phase is the expectation value $\phi \equiv \langle \bar{\boldsymbol{\psi}} \sigma_z \otimes \tau_0 \boldsymbol{\psi} \rangle$. Therefore we rewrite the interaction in the standard way as

$$\bar{\boldsymbol{\psi}}_A \tau_0 \boldsymbol{\psi}_A \bar{\boldsymbol{\psi}}_B \tau_0 \boldsymbol{\psi}_B = \frac{1}{4} [(\bar{\boldsymbol{\psi}} \sigma_0 \otimes \tau_0 \boldsymbol{\psi})^2 - (\bar{\boldsymbol{\psi}} \sigma_z \otimes \tau_0 \boldsymbol{\psi})^2], \tag{2.24}$$

the first term is a uniform density which can be neglected. To introduce the order parameter field ϕ into the theory, we perform a Hubbard-Stratonovich transformation, which utilises the property of the Gaussian integral

$$e^{x^2} = \frac{1}{4\pi^2} \int e^{(-y^2-2xy)} dy. \tag{2.25}$$

By introducing ϕ as an auxiliary field which conjugates to $\bar{\boldsymbol{\psi}}\sigma_z \otimes \tau_0 \boldsymbol{\psi}$, we have

$$e^{-U\int(\bar{\boldsymbol{\psi}}\sigma_z\otimes\tau_0\boldsymbol{\psi})^2} = \int \mathscr{D}\phi e^{U\int(\phi^2+2\phi\bar{\boldsymbol{\psi}}\sigma_z\otimes\tau_0\boldsymbol{\psi})}, \tag{2.26}$$

and the partition function now becomes

$$Z = \int \mathscr{D}\phi\mathscr{D}[\bar{\boldsymbol{\psi}},\boldsymbol{\psi}] e^{-\int(U\phi^2+\bar{\boldsymbol{\psi}}(\partial_\tau\sigma_0\otimes\tau_0+v_F\boldsymbol{\partial}\cdot\boldsymbol{\sigma}\otimes\tau_z)\boldsymbol{\psi}+2U\phi\bar{\boldsymbol{\psi}}\sigma_z\otimes\tau_0\boldsymbol{\psi})}. \tag{2.27}$$

The resulting theory includes both the fermion fields and the bosonic order parameter field, and a Yukawa interaction that couples them. This is the so-called Gross-Neveu-Yukawa theory, which defines a new family of universality classes for the Dirac-semimetal systems.

2.3.2 Gross-Neveu-Yukawa Theory

Since a detailed RG analysis of a GNY theory in which the order parameter field follows a non-linear σ model will be scrutinized in Chapter 4, it is a bit redundant to go through the details. Here we briefly sketch the momentum-shell RG of the GNY theory. The large-N expansion technique is used to control the results. We

start with the $d+1$ dimensional GNY theory in k-space:

$$S = S_{\boldsymbol{\psi}} + S_{\phi} + S_Y + S_{\lambda}, \tag{2.28}$$

$$S_{\boldsymbol{\psi}} = \int_k \bar{\boldsymbol{\psi}}(\omega,\mathbf{k})(-i\omega\sigma_0\otimes\tau_0 + v_F\mathbf{k}\cdot\boldsymbol{\sigma}\otimes\tau_0)\boldsymbol{\psi}(\omega,\mathbf{k}), \tag{2.29}$$

$$S_{\phi} = \frac{1}{2}\int_k \phi(\omega,\mathbf{k})(\omega^2 + c^2\mathbf{k}^2 + m^2)\phi(\omega,\mathbf{k}), \tag{2.30}$$

$$S_Y = \frac{g}{\sqrt{N_f}}\int_{k,q} \phi(q)\bar{\boldsymbol{\psi}}(k)\sigma_z\otimes\tau_0\boldsymbol{\psi}(k+q), \tag{2.31}$$

$$S_{\lambda} = \lambda\int_{k_1,k_2,k_3} \phi(k_1)\phi(k_2)\phi(k_3)\phi(-k_1-k_2-k_3). \tag{2.32}$$

Note that more terms are involved in the theory compared to Eq. 2.27. This is because a full theory of the order parameter field ϕ needs to be involved to make the RG calculation self-consistent. The matrix structure of the Yukawa coupling S_Y depends on the mean-field channel in which we apply the Hubbard-Stratonovich transformation, so it may vary depending on the specific phase transition. Here ϕ is a scalar field for the CDW transition, but can be a vector or tensor depending on the specific symmetry that's broken. The spin degree of freedom τ is not involved in the matrix structure but acts merely as an extra factor of 2 in the theory. Therefore in the following calculation, we absorb the spins by redefining N_f. c, v_F are the velocities for $\phi, \boldsymbol{\psi}$, respectively.

2.3.2.1 Failure of 4-ε at finite ε

Since the bosonic order parameter field is still a ϕ^4 theory, it is natural for us to seek comfort from the $4-\varepsilon$ expansion as it produces reasonable results even for $\varepsilon = 1$. However, the luck does not extend to the GNY theory. It turns out the RG of the GNY theory is much more sensitive to the dimensionality than the pure ϕ^4 theory. To see this, one can derive the RG equations of the two velocities (v_F, c) through different cutoff schemes. The slightly tedious derivation of the RG equations can be found in [55]. In the paper, the authors have used the spherical and cylindrical cutoff schemes to derive the RG corrections, and found that at infinitesimal ε, both schemes give the same fixed point at $v_F = 1, c = v_F$, indicating the emergence of Lorentz invariance at the fixed point. However, if one goes away from the critical

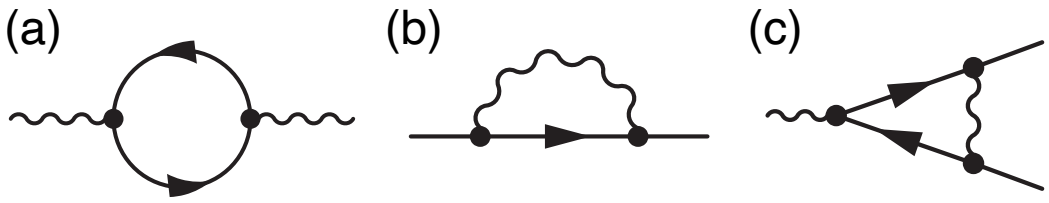

Figure 2.3: The related one-loop diagrams of the GNY theory in $D < 4$. (a)The fermion polarisation bubble diagram gives rise to the non-analytic Landau damping on the bosonic field. (b)The diagram corrects the fermionic self-energy. (c)The diagram corrects the Yukawa interaction.

dimension, i.e., ε becomes finite, $v_F = c = 1$ is no longer a fixed point in the cylindrical scheme but remains untouched in the spherical scheme. That is to say, at lower dimensions, the two cutoff schemes give different sets of critical exponents. This is unphysical. As mentioned in the previous section, although the exact value of the fixed point may be cutoff-dependent, the nature of the fixed point should not. Furthermore, the issue remains at the large-N_f limit: As long as we move away from the upper critical dimension, the results become completely scheme-dependent.

2.3.2.2 Landau Damping

The strong dependence on dimensionality suggests that the problem is probably in the scaling dimension of the fields. In other words, the scaling form of the free theory might be incorrect. Indeed, it was found in [56] that the missing ingredient is the order parameter screening. The Yukawa coupling relates the fermion to the bosons, therefore the scattering events of electrons and holes near the Fermi surface will also exert an impact on the order parameter field, in the same spirit as the screening of the long-range Coulomb interaction and the Kondo screening of the impurity spin. This is a non-perturbative effect, dubbed Landau damping, which cannot be captured within a perturbative RG scheme. To account for such screening effect, one needs to follow the standard way of calculating the Coulomb screening using a random phase approximation (RPA) and re-sum up the fermion polarisation bubble up to infinite orders. Diagrammatically this simply means to calculate the diagram correction in Fig.2.3(a) by taking the integral over the whole real axis. The

boson self-energy correction is then

$$\Pi(q) = \frac{g^2}{N_f} \int_k G_{\boldsymbol{\psi}}(k+q) G_{\boldsymbol{\psi}}(k). \tag{2.33}$$

The integral has an IR divergence at $q = 0$, this suggests that the main contribution of the order parameter screening comes from the low-energy modes, which are not accounted for in the perturbative RG scheme. Regularising the results by removing the $\Pi(0)$ singularity, one arrives at the following form:

$$\Pi(k) = \alpha_D g^2 (\omega^2 + v_F \mathbf{k}^2)^{\frac{D-2}{2}} + m^2, \tag{2.34}$$

where α_D is some prefactor that relies on the dimension D. One can see that for $D \geq 4$, $\Pi(k)$ has a higher power in $|k|$ than the quadratic k^2 term in the bare theory. Therefore the term is irrelevant under RG and could be neglected. However, for $D < 4$, the zero-energy particle-hole fluctuations of the Dirac fermions at the Fermi surface effectively screen the order parameter field, giving rise to a self-energy correction that has a lower power in $|k|$, rendering the k^2 term coming from the bare ϕ^4 theory subleading. In the RG sense, the self-energy contribution from the Landau damping is the most relevant term, and should be kept in the calculation. This non-analytic term will not flow under RG, leaving us the flexibility of choosing the scaling dimension of the bosonic fields $[\phi]$. We can fix $[\phi]$ by choosing the Yukawa coupling to be marginal, which gives $[\phi] = -2 - [g]$. This in turn renders the ϕ^4 term irrelevant, and more importantly, cures the problem of unphysical cutoff-scheme dependence [55].

2.3.2.3 Fixed Point at Large-N_f

The inclusion of the gapless Dirac fermions has significantly changed the scaling of the order parameter fields, and made our theory much more simple: We can drop the subleading k^2 term in the bosonic propagator, and the ϕ^4 interaction, and only

consider the renormalisation of the rest:

$$S = S_{\boldsymbol{\psi}} + S_{\phi} + S_Y, \tag{2.35}$$

$$S_{\boldsymbol{\psi}} = \int_k \bar{\boldsymbol{\psi}}(\omega,\mathbf{k})(-i\omega\sigma_0 + v_F\mathbf{k}\cdot\boldsymbol{\sigma})\boldsymbol{\psi}(\omega,\mathbf{k}), \tag{2.36}$$

$$S_{\phi} = \alpha_D g^2 \int_k \phi(\omega,\mathbf{k})(\omega^2 + c^2\mathbf{k}^2)^{\frac{D-2}{2}}\phi(\omega,\mathbf{k}), \tag{2.37}$$

$$S_Y = \frac{g}{\sqrt{N_f}}\int_{k,q} \phi(q)\bar{\boldsymbol{\psi}}(k)\sigma_z\boldsymbol{\psi}(k+q), \tag{2.38}$$

$$\tag{2.39}$$

Now that we have fixed the problem of cutoff-dependent results, we can choose to work in the spherical scheme, and the velocities v_F and c can be safely set to one. The related one-loop diagrams are shown in Fig.2.3. The fermionic self-energy correction has the form

$$\Sigma d\ell \int_k \bar{\boldsymbol{\psi}}(\omega,\mathbf{k})(-i\omega\sigma_0 + v_F\mathbf{k}\cdot\boldsymbol{\sigma})\boldsymbol{\psi}(\omega,\mathbf{k}), \tag{2.40}$$

where $\Sigma d\ell$ is given by

$$\begin{aligned}
\Sigma d\ell &= -\frac{g^2}{N_f}\int_q^{>} \sigma_z G_{\boldsymbol{\psi}}(q+k)\sigma_z G_{\phi}(q) \\
&= -\frac{g^2}{N_f}\int_q^{>} \sigma_z \frac{i(\Omega+\omega)\sigma_0 + (\mathbf{q}+\mathbf{k})\cdot\boldsymbol{\sigma}}{(\Omega+\omega)^2 + (\mathbf{q}+\mathbf{k})^2}\sigma_z \frac{1}{\alpha_D g^2}(\Omega^2+\mathbf{q}^2)^{-\frac{D-2}{2}} \\
&= -\frac{S_D}{\alpha_D N_f}\int_{\Lambda e^{-d\ell}}^{\Lambda} dq\, q^{-2-\frac{D-2}{2}} \\
&= -\frac{(D-2)S_D}{D\alpha_D N_f} dl.
\end{aligned} \tag{2.41}$$

In the calculation, we have expanded out the external momenta k and only keep the terms that are linear in k.

Similarly, the correction to the Yukawa coupling is evaluated as

$$\begin{aligned}\Omega\sigma_z dl &= \frac{g}{N_f^{3/2}}\int_q^{>}\sigma_z G_{\boldsymbol{\psi}}(q)\sigma_z G_{\boldsymbol{\psi}}(q)\sigma_z G_{\phi}(q)\\ &= -\frac{g}{\alpha_D N_f^{3/2}}dl. \end{aligned} \tag{2.42}$$

Combining all the one-loop corrections we can then derive the critical exponents, whose exact values are not important here. One may realise that, by fixing the scaling dimension of ϕ by making the Yukawa coupling marginal, no parameter flows under RG. That is to say, the theory is always scale-invariant, and we stay at the nontrivial fixed point throughout the whole calculation. One important observation to note is that, under the RG, not only do the bosonic ϕ fields gain an anomalous dimension from the diagrammatic corrections, but so do the fermion fields. The non-zero fermion anomalous dimension suggests that the quasi-particle residue in the fermion spectral function renormalises to zero [56], i.e., the quasi-particle picture of the Fermi liquid theory breaks down. Such non-Fermi liquid behavior [57, 58, 59, 60] near a quantum critical point is a natural result of the fermion-induced criticality, and should be related to the physics within the so-called 'quantum critical fan', such as unconventional superconductivity [61].

One last fact to face is that the one-loop results should only be valid in the large-N_f limit, but in reality the fermions in graphene have $N_f = 4$, which is not large at all. However, as in the case of ε expansion for the ϕ^4 theory when $\varepsilon = 1$, the results seem to be convergent reasonably well [62].

2.4 Discussion

In this chapter, we have introduced the Ginzburg-Landau-Wilson paradigm of phase transition. Accompanied by the powerful renormalisation group method, the order parameter theory developed by Ginzburg and Landau is extremely successful in describing the symmetry-breaking phase transitions in gapped electron systems. This leads to the discovery of similarity of critical systems at different scales, and the universal behaviors of physical observables near a critical point.

We then studied the RG of the simple scalar ϕ^4 theory, through an ϵ expansion at the upper critical dimension. The RG led us to two fixed points, the Gaussian fixed point, corresponding to the free theory, and the Wilson-Fisher fixed point, an interacting fixed point that governs the continuous phase transition.

However, for gapless electron systems, a pure order parameter theory is not enough. In order to study a symmetry-breaking phase transition in presence of electrons with a Fermi surface, one has to include the fermions in the low-energy theory. The geometry of the Fermi surface is crucial to the critical behaviors. We therefore considered the case in which the fermions have the simplest point-like Fermi surface, like the Dirac fermions in graphene. Such a low-energy theory near the Fermi surface corresponds to the Gross-Neveu theory in particle physics. Then a Hubbard-Stratonovich transformation is needed to enforce the bosonic order parameter field into the theory, which rewrites the four-fermion interaction term into a Yukawa coupling that relates the fermions and bosons.

Such a GNY theory indicates a new family of universality. The most significant feature of such a fermion-induced criticality is Landau damping. The zero-energy fluctuations of the fermions screen the order parameter propagator, generating a non-analytic correction to the bosonic self-energy which dominates in dimensions lower than 4. The gapless fermions thus induce a change in the scaling of the bosons, and the bosons in turn slap back and affect the scaling of fermions, leaving a brand new scaling behavior that is strongly dimensionality-dependent, but rather straightforward.

Chapter 3

Magnetic Hard-direction Ordering in the Anisotropic Kondo Model

We start with the original problem that RG was introduced to attack: The Kondo problem. The methods used in this chapter are perturbative numerical RG which are merely a modern version of the original ones developed by Anderson [63] and Wilson [4, 5]. We will show that those simple methods on an old problem can still give some interesting physics that might be able to provide insight into an experimentally wide observed phenomenon.

The original work in this chapter was published in *Magnetic hard-direction ordering in anisotropic Kondo systems*, M. P. Kwasigroch, H. Hu, F. Krüger, A. G. Green, Physical Review B 105 (22), 224418.[64].

3.1 Introduction

Fluctuations are at the heart of many complex ordering phenomena, leading to the formation of exotic phases of matter. Examples include nematic order in iron-based superconductors [65, 66], driven by strong spin fluctuations above the magnetic ordering temperature [67], and p-wave spin-triplet superconductivity near ferromagnetic quantum critical points [68, 69]. In the latter case, the required attraction in the p-wave channel is generated by fluctuations. This mechanism is very similar in spirit to fluctuation generated Casimir and Van-der-Waals forces [70].

In itinerant ferromagnets the coupling between the magnetic order parameter

and soft electronic particle-hole fluctuations leads to a plethora of exotic ordering phenomena [71]. It is responsible for fluctuation induced first-order behaviour at low temperatures [72, 73, 74, 75], observed experimentally in many systems [76, 77, 78, 79, 80]. Since the phase space for electronic fluctuations can be enhanced by deformations of the Fermi surface, metallic ferromagnets are very susceptible towards the formation of spin nematic [73], modulated superconducting [81] or incommensurate magnetic order [82, 83, 84, 85, 86].

Fluctuations can also have counter-intuitive effects upon the direction of magnetic order parameters. A notable example is the partially ordered phase of MnSi, in which the helimagnetic ordering vector rotates away from the lattice favored directions [87, 88]. Magnetic hard-axis ordering in metallic ferromagnets is fairly wide spread [89, 90]. Such a moment re-orientation can arise as combined effect of fluctuations and magnetic frustration in a local moment model [91]. In an alternative scenario the effect was attributed to soft electronic particle-hole fluctuations in a purely itinerant model with spin-orbit induced anisotropy [92].

In this chapter we show that electronic fluctuations can drive magnetic hard-axis ordering in anisotropic Kondo materials. As first established by Kondo [93], the scattering of electrons by local moments gives rise to logarithmic corrections to the magnetic susceptibility. In the presence of magnetic anisotropy, these logarithmic corrections depend upon direction. Near the Kondo scale, these terms can completely overwhelm the crystal-field anisotropy experienced by the local moment, driving a moment re-orientation.

We identify a generic mechanism for magnetic hard-axis ordering that fully accounts for the following experimental facts [89]: (i) All the materials that show hard-axis ordering are Kondo systems. (ii) The susceptibility crossing occurs above the magnetic ordering temperature T_c. (iii) In tetragonal systems the moment re-orientation can occur from easy plane to hard axis [94, 95, 96, 97], or the other way round, from easy axis to hard plane [98, 99]. (iv) The effect also occurs in systems that show a first-order magnetic transition [100, 101]. (v) Similar magnetic hard-axis ordering is observed in Kondo systems that order antiferromagnetically

[102, 103, 104].

The chapter is organized as follows. In Sec. 3.2, we introduce the $S = 1$, N-channel single-impurity Kondo model with single-ion anisotropy. The interplay of Kondo screening and anisotropy is studied within perturbative RG in Sec. 3.3. We show that near the Kondo scale the single-ion anisotropy can change sign, indicative of a reorientation of the dressed magnetic moment. In Sec. 3.4, we use the numerical renormalization group (NRG) to investigate the strong-coupling behavior of the single-channel Kondo model of an $S = 1$ spin with single-ion anisotropy and demonstrate that a crossing of the magnetic susceptibilities can occur far below the Kondo temperature in systems with easy-plane anisotropy. Finally, in Sec. 3.5, we summarize and discuss our results.

3.2 The Anisotropic Kondo Model

Since the magnetic susceptibility crossing occurs above Tc, irrespective of the order of the transition and the nature of the ordered state, the dominant effect can be understood on the level of a single-impurity Kondo model with single-ion anisotropy,

$$\begin{aligned}\hat{H} &= \sum_{n=1}^{N}\sum_{\mathbf{k}}^{|\varepsilon_{\mathbf{k}}|<\Lambda} \varepsilon_{\mathbf{k}}\boldsymbol{\psi}^{\dagger}_{\mathbf{k}n}\boldsymbol{\psi}_{\mathbf{k}n} + \alpha\Lambda\left(\hat{S}^{z}\right)^{2} \\ &\quad + \frac{1}{N^{2}}\sum_{n=1}^{N}\sum_{\mathbf{k},\mathbf{q}}\sum_{\gamma=x,y,z} J_{\gamma}\hat{S}^{\gamma}\boldsymbol{\psi}^{\dagger}_{\mathbf{k}n}\boldsymbol{\sigma}_{\gamma}\boldsymbol{\psi}_{\mathbf{q}n}. \end{aligned} \tag{3.1}$$

Here $\boldsymbol{\psi}^{\dagger}_{\mathbf{k}n} = (c^{\dagger}_{\mathbf{k}n\uparrow}, c^{\dagger}_{\mathbf{k}n\downarrow})$ with $c^{\dagger}_{\mathbf{k}n\sigma}$ the creation operator of an electronic quasiparticle with momentum $\mathbf{k}$ and spin σ in channel $n = 1,\ldots N$. The first term simply denotes N identical bands with dispersion $\varepsilon_{\mathbf{k}}$, subject to an energy cut-off Λ. The second term is the single-ion anisotropy of the local moment spin ($S \geq 1$) in a tetragonal crystal, expressed in units of Λ. In the following we will investigate both easy-axis ($\alpha < 0$) and easy-plane ($\alpha > 0$) anisotropies. The last term in the Hamiltonian denotes the Kondo coupling between the impurity spin and the conduction electrons, where $\boldsymbol{\sigma}_{\gamma}$ are the standard Pauli matrices. Assuming tetragonal symmetry we have Kondo couplings $J_{xy} := J_x = J_y$ and J_z.

3.3 Perturbative Renormalisation Group

To analyze the scale dependence of the single-ion anisotropy α and the Kondo couplings J_{xy} and J_z, we integrate out processes to second order in the Kondo couplings that involve the creation of particles or holes in the infinitesimal energy shells $\Lambda e^{-d\ell} < |\varepsilon_{\mathbf{k}}| < \Lambda$. This procedure, dubbed "poor man's scaling", was first applied by Anderson [63] to the anisotropic $S = 1/2$ one-channel Kondo model. For $S = 1/2$, anisotropy only enters through the Kondo couplings J_{xy} and J_z.

Here we generalize to N channels and an $S \geq 1$ impurity subject to single-ion anisotropy. Moreover, in the spirit of the conventional RG treatment we rescale to the original cut-off at each RG step. The partition function of the single-impurity Kondo model can be written down in the path-integral representation as follows

$$Z = \int \mathscr{D}\mathbf{S}(\tau)\, \mathscr{D}\boldsymbol{\psi}^{\dagger}_{\mathbf{k}n}(\tau)\mathscr{D}\boldsymbol{\psi}_{\mathbf{k}n}(\tau)\, e^{-S_0-U}, \tag{3.2}$$

where $\mathbf{S}(\tau) = (S^x(\tau), S^y(\tau), S^z(\tau))$ is the impurity spin, $\boldsymbol{\psi}^{\dagger}_{\mathbf{k}n}(\tau) = (c^{\dagger}_{\mathbf{k}n\uparrow}(\tau), c_{\mathbf{k}n\downarrow}(\tau))$ the Grassmann variables describing the conduction electrons, and

$$\begin{aligned} S_0 &= \int_0^{\beta} d\tau \sum_{n=1}^{N} \sum_{\mathbf{k}}^{|\varepsilon_{\mathbf{k}}|<\Lambda} \boldsymbol{\psi}^{\dagger}_{\mathbf{k}n}(\tau)\,(\partial_\tau + \varepsilon_{\mathbf{k}})\,\boldsymbol{\psi}_{\mathbf{k}n}(\tau) + S_{\mathrm{imp}}[\mathbf{S}(\tau)], \\ U &= \int_0^{\beta} d\tau \sum_{n=1}^{N} \sum_{\mathbf{k},\mathbf{q}} \sum_{\gamma=x,y,z} J_\gamma S^\gamma(\tau) \boldsymbol{\psi}^{\dagger}_{\mathbf{k}n}(\tau)\boldsymbol{\sigma}_\gamma\boldsymbol{\psi}_{\mathbf{q}n}(\tau). \end{aligned} \tag{3.3}$$

S_0 is the action corresponding to the Hamiltonian $\hat{H}_0 = \sum_{\mathbf{k},n,\sigma} \varepsilon_{\mathbf{k}} c^{\dagger}_{\mathbf{k}n\sigma} c_{\mathbf{k}n\sigma} + \alpha\Lambda\left(\hat{S}^z\right)^2$ and $S_{\mathrm{imp}}[\mathbf{S}(\tau)]$ is the action of a free impurity with a spin quantum number s and Hamiltonian $\hat{H}_{\mathrm{imp}} = \alpha\Lambda\left(\hat{S}^z\right)^2$. This latter action contains the necessary terms that enforce constraints satisfied by $\mathbf{S}(\tau)$. We do not give an explicit form here, which will depend on the representation used, e.g. Abrikosov pseudofermions, spin-coherent states, Schwinger bosons, etc., and is not important for subsequent representation-independent calculations. Note also that every sum over electron momenta $\mathbf{k}$ includes the normalization factor of $1/\sqrt{N_s}$, where N_s is the number of electron lattice sites.

3.3.1 Integrating out fast modes

We begin the renormalization group procedure by integrating out fast fermion modes $\boldsymbol{\psi}^{\dagger}_{\mathbf{k}n}(\tau)$ with $\Lambda e^{-d\ell} < |\varepsilon_{\mathbf{k}}| < \Lambda$. To second order in the Kondo exchange U, the renormalized actions can be written as

$$\begin{aligned} S_0' &= \int_0^\beta d\tau \sum_{\mathbf{k},n}^{|\varepsilon_{\mathbf{k}}|<\Lambda e^{-d\ell}} \boldsymbol{\psi}^{\dagger}_{\mathbf{k}n}(\tau)\left(\partial_\tau + \varepsilon_{\mathbf{k}}\right)\boldsymbol{\psi}_{\mathbf{k}n}(\tau) + S_{\rm imp}[\mathbf{S}(\tau)], \\ U' &= \int_0^\beta d\tau \sum_{\mathbf{k},\mathbf{q},n}^{|\varepsilon_{\mathbf{k},\mathbf{q}}|<\Lambda e^{-d\ell}} \sum_{\gamma=x,y,z} J_\gamma S^\gamma(\tau)\boldsymbol{\psi}^{\dagger}_{\mathbf{k}n}(\tau)\boldsymbol{\sigma}_\gamma\boldsymbol{\psi}_{\mathbf{q}n}(\tau) - \frac{1}{2}\langle U^2\rangle^{\rm conn.}_{\rm fast}, \end{aligned} \tag{3.4}$$

where the expectation value is taken with respect to the part of S_0 describing the fast modes. We write $-\frac{1}{2}\langle U^2\rangle^{\rm conn.}_{\rm fast}$ as the following sum

$$-\frac{1}{2}\langle U^2\rangle^{\rm conn.}_{\rm fast} = u_1 J_{xy}^2 + u_2 J_z^2 + u_3 J_z J_{xy}, \tag{3.5}$$

and we will now go through the calculation of each of the coefficients u_1, u_2, u_3.

3.3.1.1 J_{xy}^2 coefficient

The J_{xy}^2 coefficient is given by the following expectation value

$$\begin{aligned} u_1 &= -\int d\tau_1 d\tau_2 \sum_{n,m=1}^{N} \sum_{\mathbf{k},\mathbf{k}'}^{|\varepsilon_{\mathbf{k},\mathbf{k}'}|<\Lambda e^{d\ell}} \sum_{\mathbf{q},\mathbf{q}'}^{\Lambda e^{-d\ell}<|\varepsilon_{\mathbf{q},\mathbf{q}'}|<\Lambda} \Big(S^+(\tau_2)S^-(\tau_1)\, c_{\mathbf{k}m\uparrow}(\tau_2)c^{\dagger}_{\mathbf{k}'n\uparrow}(\tau_1) \\ &\quad \times \Big\langle c^{\dagger}_{\mathbf{q}m\downarrow}(\tau_2)c_{\mathbf{q}'n\downarrow}(\tau_1)\Big\rangle + S^-(\tau_2)S^+(\tau_1)\, c_{\mathbf{k}m\downarrow}(\tau_2)c^{\dagger}_{\mathbf{k}'n\downarrow}(\tau_1)\, \Big\langle c^{\dagger}_{\mathbf{q}m\uparrow}(\tau_2)c_{\mathbf{q}'n\uparrow}(\tau_1)\Big\rangle \Big), \\ &= -\rho d\ell\Lambda \int d\tau_1 d\tau_2 \sum_n \sum_{\mathbf{k},\mathbf{k}'\in{\rm slow}} {\rm sign}(\tau_2-\tau_1)e^{-|\tau_2-\tau_1|\Lambda}\Big(S^+(\tau_2)S^-(\tau_1)\, c_{\mathbf{k}n\uparrow}(\tau_2)c^{\dagger}_{\mathbf{k}'n\uparrow}(\tau_1) \\ &\quad + S^-(\tau_2)S^+(\tau_1)\, c_{\mathbf{k}n\downarrow}(\tau_2)c^{\dagger}_{\mathbf{k}'n\downarrow}(\tau_1)\Big) \equiv u_1^{(1)} + u_1^{(2)}, \end{aligned} \tag{3.6}$$

where $\sum_{\mathbf{q},\mathbf{q}'\in{\rm fast}}\langle c^{\dagger}_{\mathbf{q}m\sigma}(\tau_2)c_{\mathbf{q}'n\sigma}(\tau_1)\rangle = \delta_{mn}\rho d\ell\Lambda{\rm sign}(\tau_2-\tau_1)e^{-|\tau_2-\tau_1|\Lambda}$ in the limit $\beta\Lambda\to\infty$. It is useful to introduce new variables $\tau = \frac{1}{2}(\tau_1+\tau_2)$ and $\Delta = \tau_2 - \tau_1$, and split the integration over Δ into $\Delta > 0$ and $\Delta < 0$ regions. In the limit $\Lambda\to\infty$, when

$|\Delta| \to 0$, we can write the first term as

$$u_1^{(1)} = -\rho d\ell \Lambda \sum_n \sum_{\mathbf{k},\mathbf{k}' \in \text{slow}} \int d\tau \quad \left(\int_{\Delta>0} d\Delta \, e^{-\Lambda\Delta} \, \langle \tau | e^{\Delta \hat{H}_0/2} \hat{c}_{\mathbf{k}n\uparrow} \hat{S}^+ e^{-\Delta \hat{H}_0} \hat{c}^\dagger_{\mathbf{k}'n\uparrow} \hat{S}^- e^{\Delta \hat{H}_0/2} | \tau \rangle \right.$$
$$\left. + \int_{\Delta<0} d\Delta \, e^{\Lambda\Delta} \, \langle \tau | e^{-\Delta \hat{H}_0/2} \hat{c}^\dagger_{\mathbf{k}'n\uparrow} \hat{S}^- e^{\Delta \hat{H}_0} \hat{c}_{\mathbf{k}n\uparrow} \hat{S}^+ e^{-\Delta \hat{H}_0/2} | \tau \rangle \right), \tag{3.7}$$

where we have transformed to the operator representation of the expansion of the partition function in powers of J_γ, and $|\tau\rangle$ are the path-integral coherent states in terms of which the partition function is written down. Integrating over Δ, we obtain

$$\begin{aligned} u_1^{(1)} &= -\rho d\ell \Lambda \sum_n \sum_{\mathbf{k},\mathbf{k}' \in \text{slow}} \int d\tau \, \left\langle \tau \left| \frac{\hat{S}^+ \hat{S}^- \hat{c}_{\mathbf{k}n\uparrow} \hat{c}^\dagger_{\mathbf{k}'n\uparrow}}{\Lambda(1+\alpha(1-2\hat{S}^z))} + \frac{\hat{S}^- \hat{S}^+ \hat{c}^\dagger_{\mathbf{k}'n\uparrow} \hat{c}_{\mathbf{k}n\uparrow}}{\Lambda(1+\alpha(1+2\hat{S}^z))} \right| \tau \right\rangle \\ &= 2\rho d\ell \sum_n \sum_{\mathbf{k},\mathbf{k}' \in \text{slow}} \int d\tau \, c^\dagger_{\mathbf{k}n\uparrow}(\tau) c_{\mathbf{k}'n\uparrow}(\tau) \left((1-\alpha(1-2s(s+1))) S^z(\tau) - 2\alpha (S^z(\tau))^3 \right) \\ &\quad -2N\rho^2 \Lambda d\ell \int d\tau \, (1-\alpha(1-2S^z(\tau))) \left(s(s+1) - (S^z(\tau))^2 + S^z(\tau) \right) + \mathscr{O}(\alpha^2), \end{aligned} \tag{3.8}$$

where we have neglected terms proportional to $\varepsilon_{\mathbf{k}} \Lambda^{-1}$ in the first line and terms second order in α in the second line. Following the same steps, we obtain for the second term in Eq. 3.6

$$\begin{aligned} u_1^{(2)} &= -\rho d\ell \Lambda \sum_n \sum_{\mathbf{k},\mathbf{k}' \in \text{slow}} \int d\tau \, \left\langle \tau \left| \frac{\hat{S}^- \hat{S}^+ \hat{c}_{\mathbf{k}n\downarrow} \hat{c}^\dagger_{\mathbf{k}'n\downarrow}}{\Lambda(1+\alpha(1+2\hat{S}^z))} + \frac{\hat{S}^+ \hat{S}^- \hat{c}^\dagger_{\mathbf{k}'n\downarrow} \hat{c}_{\mathbf{k}n\downarrow}}{\Lambda(1+\alpha(1-2\hat{S}^z))} \right| \tau \right\rangle \\ &= -2\rho d\ell \sum_n \sum_{\mathbf{k},\mathbf{k}' \in \text{slow}} \int d\tau \, c^\dagger_{\mathbf{k}n\downarrow}(\tau) c_{\mathbf{k}'n\downarrow}(\tau) \left((1-\alpha(1-2s(s+1))) S^z(\tau) - 2\alpha (S^z(\tau))^3 \right) \\ &\quad -2N\rho^2 \Lambda d\ell \int d\tau \, (1-\alpha(1+2S^z(\tau))) \left(s(s+1) - (S^z(\tau))^2 - S^z(\tau) \right). \end{aligned} \tag{3.9}$$

Putting $u_1^{(1)}$ and $u_1^{(2)}$ together, we obtain the coefficient of the J_{xy}^2 term,

$$\begin{aligned} u_1 &= 2\rho d\ell \sum_n \sum_{\mathbf{k},\mathbf{k}'\in \text{slow}} \int d\tau \, \left(c^\dagger_{\mathbf{k}n\uparrow}(\tau) c_{\mathbf{k}'n\uparrow}(\tau) - c^\dagger_{\mathbf{k}n\downarrow}(\tau) c_{\mathbf{k}'n\downarrow}(\tau) \right) \\ &\quad \times \left((1-\alpha(1-2s(s+1))) S^z(\tau) - 2\alpha (S^z(\tau))^3 \right) \\ &\quad + 4N\rho^2 d\ell (1-3\alpha)\Lambda \int d\tau \, (S^z(\tau))^2 + \text{const.} + \mathscr{O}(\alpha^2), \end{aligned} \tag{3.10}$$

The J_{xy}^2 coefficient contains terms proportional to $(S^z(\tau))^2$, which renormalize α by $4NJ_{xy}^2\rho^2 d\ell(1-3\alpha)$, as well as terms proportional to $c^\dagger_\sigma(\tau)c_\sigma(\tau)S^z(\tau)$ and $c^\dagger_\sigma(\tau)c_\sigma(\tau)(S^z(\tau))^3$. For $s=1$, $(S^z(\tau))^3 = S^z(\tau)$, and both of these renormalize J_z. For $s>1$, terms proportional to $c^\dagger_\sigma(\tau)c_\sigma(\tau)(S^z(\tau))^3$ generate a new coupling that is not present in the original model. We will neglect these for $s>1$ and only keep terms proportional to $c^\dagger_\sigma(\tau)c_\sigma(\tau)S^z(\tau)$, which renormalize J_z. (Note that our result is exact for $s=1$.) We thus obtain the following renormalization of J_z

$$J_z' = \begin{cases} J_z + 2\rho d\ell J_{xy}^2 (1+\alpha) & \text{for } s=1, \\ \\ J_z + 2\rho d\ell J_{xy}^2 (1-\alpha(1-2s(s+1))) & \text{for } s>1, \end{cases}$$

3.3.1.2 J_z^2 coefficient

The J_z^2 coefficient is given by

$$u_2 = -\sum_\sigma \sum_{n,m}^{N} \sum_{\mathbf{k},\mathbf{k}'}^{<} \sum_{\mathbf{q},\mathbf{q}'}^{>} \int d\tau_1 d\tau_2 \, S^z(\tau_2) S^z(\tau_1) c_{\mathbf{k}m\sigma}(\tau_2) c^\dagger_{\mathbf{k}'n\sigma}(\tau_1) \left\langle c^\dagger_{\mathbf{q}'m\sigma}(\tau_2) c_{\mathbf{q}n\sigma}(\tau_1) \right\rangle \tag{3.11}$$

Following the same steps as for the J_{xy}^2 coefficient u_1, we rewrite u_2 as

$$\begin{aligned} u_2 &= -\rho\Lambda d\ell \sum_n \sum_{\mathbf{k},\mathbf{k}'\in\text{slow}} \int d\tau \Big(\int_{\Delta>0} d\Delta \, e^{-\Lambda\Delta} \langle \tau | e^{\Delta \hat{H}_0/2} \hat{c}_{\mathbf{k}n\sigma} \hat{S}^z e^{-\Delta\hat{H}_0} \hat{c}^\dagger_{\mathbf{k}'n\sigma} \hat{S}^z e^{\Delta\hat{H}_0/2} | \tau \rangle \\ &\quad + \int_{\Delta<0} d\Delta \, e^{\Lambda\Delta} \langle \tau | e^{-\Delta\hat{H}_0/2} \hat{c}^\dagger_{\mathbf{k}'n\sigma} \hat{S}^z e^{\Delta\hat{H}_0} \hat{c}_{\mathbf{k}n\sigma} \hat{S}^z e^{-\Delta\hat{H}_0/2} | \tau \rangle \Big) \\ &= -\rho d\ell \sum_n \sum_{\mathbf{k},\mathbf{k}'\in\text{slow}} \int d\tau \, \left\langle \tau \left| (\hat{S}^z)^2 (\hat{c}_{\mathbf{k}n\sigma} \hat{c}^\dagger_{\mathbf{k}'n\sigma} + \hat{c}^\dagger_{\mathbf{k}'n\sigma} \hat{c}_{\mathbf{k}n\sigma}) \right| \tau \right\rangle \\ &= -4N\rho^2 d\ell \int d\tau \, (S^z(\tau))^2 . \end{aligned} \tag{3.12}$$

Hence, the J_z^2 term renormalizes α by $-4NJ_z\rho^2 d\ell$. Combining the renormalization of α from the J_{xy}^2 and J_z^2 terms, its overall renormalization is given by

$$\alpha' = \alpha + 4NJ_{xy}^2\rho^2 d\ell(1-3\alpha) - 4NJ_z^2\rho^2 d\ell. \tag{3.13}$$

3.3.1.3 $J_{xy}J_z$ coefficient

The coefficient of the $J_{xy}J_z$ term is given by

$$\begin{aligned} u_3 &= \sum_{n,m=1}^{N}\sum_{\mathbf{k},\mathbf{k}'\in\text{slow}}\sum_{\mathbf{q},\mathbf{q}'\in\text{fast}}\int d\tau_1 d\tau_2 \Big(S^+(\tau_2)S^z(\tau_1)\, c_{\mathbf{k}m\uparrow}(\tau_2)c^\dagger_{\mathbf{k}'n\downarrow}(\tau_1)\, \Big\langle c^\dagger_{\mathbf{q}'m\downarrow}(\tau_2)c_{\mathbf{q}n\downarrow}(\tau_1)\Big\rangle \\ &\quad -S^z(\tau_2)S^+(\tau_1)\, c_{\mathbf{k}m\uparrow}(\tau_2)c^\dagger_{\mathbf{k}'n\downarrow}(\tau_1)\, \Big\langle c^\dagger_{\mathbf{q}'m\uparrow}(\tau_2)c_{\mathbf{q}n\uparrow}(\tau_1)\Big\rangle\Big) + \text{h.c.} \\ &\quad \equiv \Big(u_3^{(1)} + u_3^{(2)}\Big) + \text{h.c.} \end{aligned} \tag{3.14}$$

Following the same steps as for the J_{xy}^2 coefficient, we can rewrite the first of the above terms as follows

$$\begin{aligned} u_3^{(1)} &= \rho\Lambda d\ell \sum_n \sum_{\mathbf{k},\mathbf{k}'\in\text{slow}} \int d\tau \Big(\int_{\Delta>0} d\Delta\, e^{-\Lambda\Delta}\, \langle\tau|e^{\Delta\hat{H}_0/2}\hat{c}_{\mathbf{k}n\uparrow}\hat{S}^+e^{-\Delta\hat{H}_0}\hat{c}^\dagger_{\mathbf{k}'n\downarrow}\hat{S}^z e^{\Delta\hat{H}_0/2}|\tau\rangle \\ &\quad + \int_{\Delta<0} d\Delta\, e^{\Lambda\Delta}\, \langle\tau|e^{-\Delta\hat{H}_0/2}\hat{c}^\dagger_{\mathbf{k}'n\downarrow}\hat{S}^z e^{\Delta\hat{H}_0}\hat{c}_{\mathbf{k}n\uparrow}\hat{S}^+e^{-\Delta\hat{H}_0/2}|\tau\rangle\Big) \\ &= \rho d\ell \sum_n \sum_{\mathbf{k},\mathbf{k}'\in\text{slow}} \int d\tau \left\langle \tau \left| \hat{c}^\dagger_{\mathbf{k}'n\downarrow}\hat{c}_{\mathbf{k}n\uparrow}\left(\frac{\hat{S}^z}{\hat{S}^z - \frac{\alpha}{2}(1-2\hat{S}^z)}\hat{S}^+ - S^+\frac{\hat{S}^z}{1-\frac{\alpha}{2}(1+2\hat{S}^z)}\right)\right|\tau\right\rangle \\ &= \rho d\ell \sum_n \sum_{\mathbf{k},\mathbf{k}'\in\text{slow}} \int d\tau \left\langle \tau \left| \hat{c}^\dagger_{\mathbf{k}'n\downarrow}\hat{c}_{\mathbf{k}n\uparrow}\left(1-\frac{\alpha}{2}-2\alpha\left(\left(\hat{S}^z\right)^2-\hat{S}^z\right)\right)\hat{S}^+\right|\tau\right\rangle + \mathscr{O}(\alpha^2) \\ &= \left(1-\frac{\alpha}{2}\right)\rho d\ell \sum_n \sum_{\mathbf{k},\mathbf{k}'\in\text{slow}} \int d\tau\, c^\dagger_{\mathbf{k}'n\downarrow}(\tau)c_{\mathbf{k}n\uparrow}(\tau)S^+(\tau) + \mathscr{O}(\alpha^2), \end{aligned} \tag{3.15}$$

where the last line is exact for $s=1$, and for $s>1$, higher order terms that generate new couplings have been neglected. Applying the same steps to the second term in

Eq. 3.14 we obtain

$$\begin{aligned} u_3^{(2)} &= -\rho d\ell \sum_n \sum_{\mathbf{k},\mathbf{k}'\in \text{slow}} \int d\tau \left\langle \tau \left| \hat{c}^\dagger_{\mathbf{k}'n\downarrow} \hat{c}_{\mathbf{k}n\uparrow} \left(S^+ \frac{\hat{S}^z}{1-\frac{\alpha}{2}(1+2\hat{S}^z)} - \frac{\hat{S}^z}{1-\frac{\alpha}{2}(1-2\hat{S}^z)} \hat{S}^+ \right) \right| \tau \right\rangle \\ &= \rho dl \sum_n \sum_{\mathbf{k},\mathbf{k}'\in \text{slow}} \int d\tau \left\langle \tau \left| \hat{c}^\dagger_{\mathbf{k}'n\downarrow} \hat{c}_{\mathbf{k}n\uparrow} \left(1 - \frac{\alpha}{2} - 2\alpha \left(\left(\hat{S}^z\right)^2 - \hat{S}^z \right) \right) \hat{S}^+ \right| \tau \right\rangle + \mathscr{O}(\alpha^2) \\ &= \left(1-\frac{\alpha}{2}\right) \rho d\ell \sum_n \sum_{\mathbf{k},\mathbf{k}'\in \text{slow}} \int d\tau \, c^\dagger_{\mathbf{k}'n\downarrow}(\tau) c_{\mathbf{k}n\uparrow}(\tau) S^+(\tau) + \mathscr{O}(\alpha^2) \end{aligned} \tag{3.16}$$

Putting the two parts of u_3 together, we obtain

$$u_3 = 2\left(1-\frac{\alpha}{2}\right) \rho d\ell \sum_n \sum_{\mathbf{k},\mathbf{k}'\in \text{slow}} \int d\tau \, \left(c^\dagger_{\mathbf{k}'n\downarrow}(\tau) c_{\mathbf{k}n\uparrow}(\tau) S^+(\tau) + \text{h.c.} \right) \tag{3.17}$$

The $J_{xy}J_z$ term thus renormalizes the J_{xy} coupling

$$J'_{xy} = J_{xy} + 2\rho d\ell J_{xy} J_z \left(1-\frac{\alpha}{2}\right). \tag{3.18}$$

3.3.2 Restoring the cutoff

In the neighborhood of the Fermi surface defined by $|\varepsilon_{\mathbf{k}}| < \Lambda$, we can approximate the sum over $\mathbf{k}$ states as

$$\sum_{\mathbf{k}} \propto \int dk_\perp d\mathbf{k}_\parallel, \tag{3.19}$$

where $dk_\perp$ and $d\mathbf{k}_\parallel$ correspond to local changes in components of $\mathbf{k}$ perpendicular and parallel to the Fermi surface respectively. In particular, $k_\perp$ measures the perpendicular distance to the Fermi surface in $\mathbf{k}$-space. We will also assume a constant density of states throughout the Fermi surface neighbourhood, as well as a linear energy dispersion $\varepsilon_{\mathbf{k}} \propto k_\perp$. With the above assumptions in mind, the following rescaling will restore the energy cutoff, which has been reduced to $\Lambda e^{-d\ell}$ by

integrating out the fast modes

$$\begin{aligned} k_\perp &\to e^{-d\ell} k_\perp \\ \tau &\to e^{d\ell}\tau \\ c^\dagger_{n\sigma}(k_\perp, \mathbf{k}_\parallel, \tau) &\to e^{d\ell/2} c^\dagger_{n\sigma}(k_\perp, \mathbf{k}_\parallel, \tau), \end{aligned} \tag{3.20}$$

The only couplings that will acquire naive scaling as a result are

$$\begin{aligned} \alpha &\to e^{d\ell}\alpha, \\ \beta &\to e^{-d\ell}\beta. \end{aligned} \tag{3.21}$$

3.3.3 RG flow equations

We can now put together the renormalisations generated by $-\frac{1}{2}\langle U^2\rangle^{\text{conn.}}_{\text{fast}}$, and listed in sec. 3.3.1, and the rescaling given in sec. 3.3.2, to obtain the following RG flow equations

$$\begin{aligned} \frac{dg_z}{d\ell} &= \begin{cases} g_{xy}^2(1+\alpha)) & \text{for } s=1, \\ \\ g_{xy}^2(1+\alpha)\left(1-\alpha\left(1-2s(s+1)\right)\right) & \text{for } s>1, \end{cases} \\ \frac{dg_{xy}}{d\ell} &= g_{xy}g_z\left(1-\frac{\alpha}{2}\right), \\ \frac{d\alpha}{d\ell} &= \alpha + N\left(g_{xy}^2 - g_z^2\right) - 3Ng_{xy}^2\alpha, \end{aligned} \tag{3.22}$$

where we have introduced the dimensionless couplings $g_{xy} := 2J_{xy}\rho$ and $g_z := 2J_z\rho$. The flow equations are exact in the limit $\Lambda \to \infty$ and $\alpha \to 0$. They describe the RG flow fully for $s = 1$. For $s > 1$, new terms in the Hamiltonian, proportional to $\left(\hat{S}^z\right)^3$, $\hat{S}^z\hat{S}^+$, $\left(\hat{S}^z\right)^2\hat{S}^+$ and their hermitian conjugates, are generated. These were not present in the original anisotropic Kondo model and have been neglected.

The above system of equations exhibits two possible runaway behaviours: (i) anisotropy runaway $\{|\alpha| \to \infty, g_{xy} \to 0, g_z \to \text{const}\}$, (ii) Kondo runaway $\{|\alpha| \to 0, g_{xy} \to \infty, g_z \to \infty\}$. The regime we fall in is determined by which parameter

diverges faster. We can illustrate this with the example of initially small anisotropy $\alpha(0)$, and initially small Kondo couplings $g_{xy}(0) = g_z(0)$. At short RG times ℓ, $\alpha(\ell) = \alpha(0)e^{\ell}$ and $g_\gamma(\ell) = (g_\gamma^{-1}(0) - \ell)^{-1}$. Hence, if $|\alpha(0)|e^{-1/g_\gamma(0)}$, α becomes of order one first and we fall into the anisotropy runaway regime. Otherwise, g_γ becomes of order one first and we fall into the Kondo runaway regime. Before the Kondo couplings increase beyond the validity of the weak-coupling RG approach, a sign change of α can occur.

Since the qualitative behaviour of the RG flow is the same for all values of $S \geq 1$ and N, we focus on the under-screened case with $S = 1$ and $N = 1$ from now on. The weak-coupling RG equations are

$$\begin{aligned} \frac{dg_z}{d\ell} &= g_{xy}^2(1+\alpha), \quad \frac{dg_{xy}}{d\ell} = g_{xy}g_z(1-\frac{\alpha}{2}), \\ \frac{d\alpha}{d\ell} &= \alpha + g_{xy}^2 - g_z^2 - 3g_{xy}^2\alpha, \end{aligned} \tag{3.23}$$

where $g_\gamma = 2\rho J_\gamma$ are the dimensionless Kondo couplings. For simplicity, we have adopted the usual assumption [63] of a constant density of states ρ. The scale parameter ℓ is related to temperature, $\ell = \log(\Lambda/T)$.

In the absence of anisotropy, $g_{xy} = g_z$ and $\alpha = 0$, the system remains isotropic under the RG flow, as expected. For $\alpha = 0$, the RG equations for g_{xy} and g_z take the familiar form [63]. In the relevant regime of antiferromagnetic Kondo couplings the flow is towards strong coupling, $g_\gamma \to \infty$, corresponding to the Kondo regime.

This picture is incomplete, however, since the anisotropy in the Kondo couplings generates single-ion anisotropy due to the $\left(g_{xy}^2 - g_z^2\right)$ term in the RG equation for α. This leads to a flow out of the $\alpha = 0$ plane. For $g_{xy} > g_z$ the flow is to positive α, corresponding to easy-plane anisotropy, while for $g_{xy} < g_z$ an easy axis anisotropy is generated. Finite α modifies the RG flow of the Kondo couplings, e.g., easy-plane anisotropy ($\alpha > 0$) leads to g_z growing faster than g_{xy}. The interplay of these effects ultimately leads to the moment re-orientation that is the main subject of this work.

In Fig. 3.1, the evolution of the coupling constants under the RG is shown.

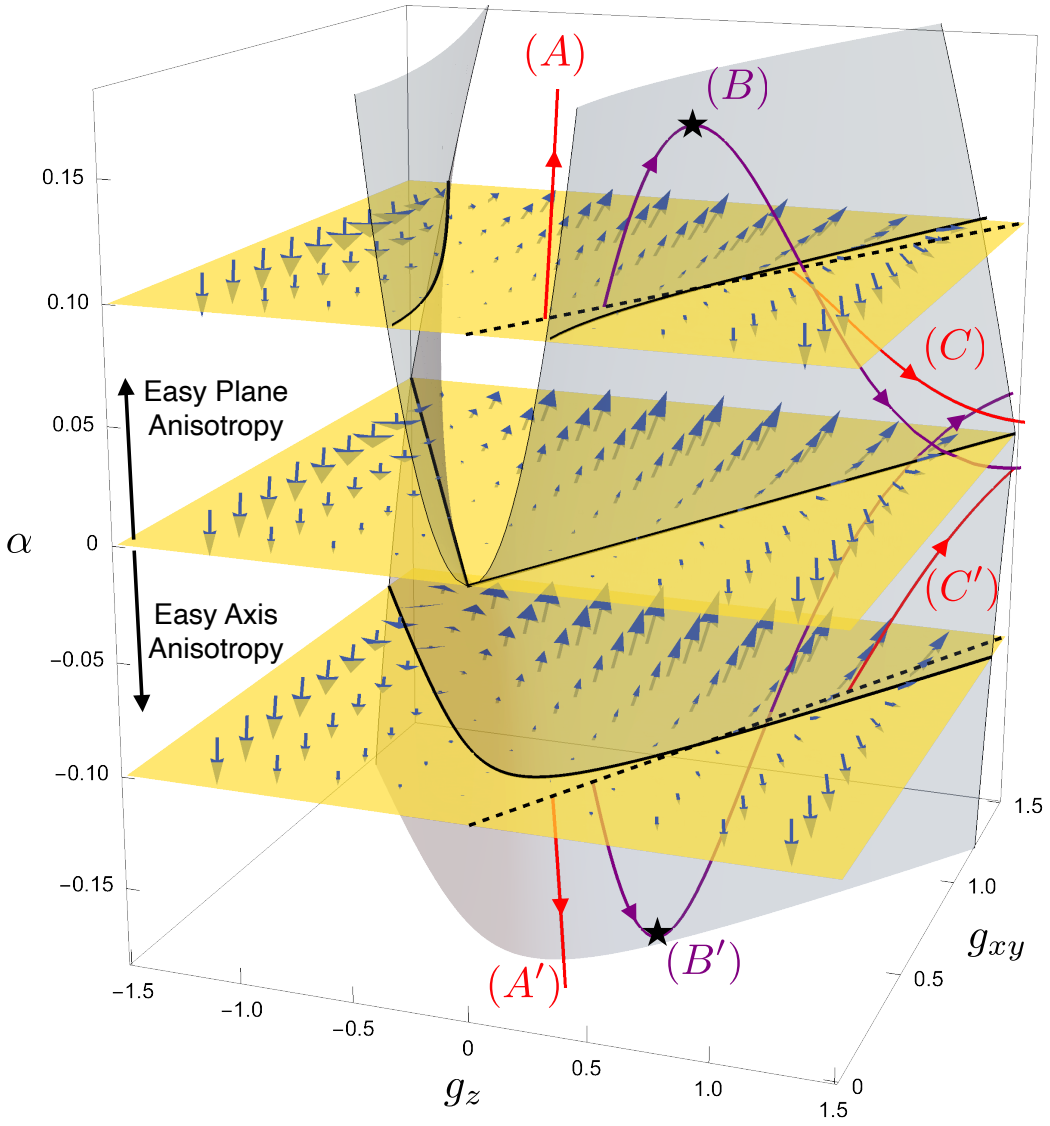

Figure 3.1: RG flow of the single-ion anisotropy α and Kondo couplings g_{xy}, g_z. The direction of the flow is shown by blue arrows and the transparent grey surface separates regions of increasing and decreasing α. The trajectories (A),(B),(C) correspond to an initial easy-plane anisotropy $\alpha(0) = 0.1$ and increasing values of $g_{xy}(0) = g_z(0)$: (A) For weak $g_\gamma(0)$ the anisotropy stabilizes the moment and supresses Kondo screening. (B) For intermediate values of $g_\gamma(0)$, α changes sign before g_γ diverge. This indicates a moment re-orientation above the Kondo temperature. (C) For large $g_\gamma(0)$ the Kondo scale is reached before moment re-orientation can occur. (A'),(B') and (C') show the analogous behaviour for an initial easy-axis anisotropy $\alpha(0) = -0.1$.

For the trajectories (A), (B) and (C) we have chosen an easy-plane anisotropy $\alpha(0) = 0.1$ and initially isotropic Kondo couplings, $g_{xy}(0) = g_z(0)$. In the regime of weak Kondo coupling (A), α keeps growing, leaving the regime where the RG equations are valid. This behaviour indicates that the single ion anisotropy stabilizes the moment, preventing Kondo screening. Magnetic hard-axis ordering therefore does not occur for sufficiently strong anisotropy, compared to the Kondo coupling, which is consistent with experimental observations [89].

For (B) the growing splitting of the increasing Kondo couplings reverse the flow of α at a scale $\ell_{\max}$, corresponding to the point where the trajectory crosses the grey surface in Fig. (3.1), defined by $\alpha + g_{xy}^2 - g_z^2 - 3g_{xy}^2\alpha = 0$. At some scale ℓ_0, corresponding to a temperature $T_0 = \Lambda e^{-\ell_0}$, α changes sign, indicating a re-orientation of the moment. At a larger scale $\ell_* > \ell_0$ the rapidly increasing Kondo couplings diverge, corresponding to the Kondo temperature $T_K = \Lambda e^{-\ell^*} < T_0$.

If the initial Kondo couplings are too large (C), the Kondo scale is reached before a moment re-orientation occurs. Note that this strong coupling regime lies beyond the validity of the perturbative RG treatment. The trajectories (A'), (B') and (C') show the completely analogous behaviour for the case of easy-axis anisotropy.

3.4 Numerical Renormalisation Group

In order to investigate if hard-direction ordering of under-screened moments could occur in the strong-coupling regime at temperatures far below the Kondo temperature T_K, we employ the numerical renormalization group (NRG). Previous NRG studies [105] analyzed the effects of single-ion anisotropy on the Kondo screening mechanism and on possible non-Fermi-liquid behaviour, but did not investigate the behaviour of magnetic susceptibilities along different directions. It is important to stress that in the strong-coupling regime the physics will crucially depend on S and N. Here we only investigate the single-channel Kondo model for $S = 1$.

First, we give a brief overview of the numerical process of the NRG. A detailed derivation of the mapping can be found in Wilson's original paper [4]. The idea is to discretise the RG rescaling to make the calculation numerically compatible. To

do so, the original Hamiltonian is mapped to an iterative Hamiltonian of the form

$$H = \sum_{n=0}^{\infty}\sum_{\sigma} t_n(f^{\dagger}_{n\sigma}f_{n+1\sigma}+f^{\dagger}_{n+1\sigma}f_{n\sigma}) + J_z(f^{\dagger}_{0\uparrow}f_{0\uparrow} - f^{\dagger}_{0\downarrow}f_{0\downarrow})S^z \\ + J_{\pm}(f^{\dagger}_{0\uparrow}f_{0\downarrow}S^- - f^{\dagger}_{0\downarrow}f_{0\uparrow}S^+) - \alpha(S^z)^2, \tag{3.24}$$

where

$$t_n = \frac{[(1+\Lambda^{-1})/2]\Lambda^{-n/2}(1-\Lambda^{-n-1})}{[(1-\Lambda^{-2n-1})(1-\Lambda^{-2n-3})]^{1/2}} \tag{3.25}$$

is the hopping parameter that only depends on the energy scaling factor Λ. f_n are the electrons on the n-th site of the chain, and the impurity spin sits on the origin of the chain. In this language, only the electron on the first site interacts with the impurity spin directly. The Hamiltonian can be further recast into a recursive form

$$H_N = \Lambda^{(N-1)/2}\{\sum_{n=0}^{N-1}\sum_{\sigma} t_n(f^{\dagger}_{n\sigma}f_{n+1\sigma}+f^{\dagger}_{n+1\sigma}f_{n\sigma}) + J_z(f^{\dagger}_{0\uparrow}f_{0\uparrow} - f^{\dagger}_{0\downarrow}f_{0\downarrow})S^z \\ + J_{\pm}(f^{\dagger}_{0\uparrow}f_{0\downarrow}S^- - f^{\dagger}_{0\downarrow}f_{0\uparrow}S^+) - \alpha(S^z)^2\}. \tag{3.26}$$

In each numerical iteration, the Hamiltonian is diagonalized to find the lowest-lying energy states. Just like the RG procedures mentioned in chapter 2, the energy scale gets smaller and smaller as N increases due to the prefactor $\Lambda^{(N-1)/2}$. Therefore in each iteration, the energy needs to be rescaled back to the original scale. Then an extra electron site is added to the chain, and by re-diagonalising the new Hamiltonian we slowly evolve the low-energy states towards the long-wavelength limit. By repeating the above procedure, the Kondo Hamiltonian starts from the weak coupling regime and ends up in the strong coupling regime in a non-perturbative way.

In principle, the results obtained through this process are only exact in the limit of $\Lambda \to 1, N \to \infty$, but it has been shown that the calculation converges quickly after a few dozen iterations, and the results are reasonable even at $\Lambda = 2$. However one may realise that the dimensionality of the Hilbert space scales as 4^N, which blows up quickly after several iterations. To avoid this we need to set a cutoff on the size of the Hilbert space and only keep the lowest energy eigenvalues in each step. This

is justified as we are interested in the ground state behavior of the system at low temperatures.

Implementing the NRG scheme allows us to work out the renormalisation of the theory outside the perturbative regime. In the strong-coupling regime, the experimentally relevant quantity is not χ_γ^{imp}, but the impurity contribution to the total susceptibility, $\chi_\gamma^{\text{cont}}$, defined as the difference between the total susceptibility of the system with and without the impurity. As the temperature is lowered, the impurity increasingly 'outsources' its magnetic moment to the conduction electrons. While the total z-angular momentum is conserved and the dressed impurity states are eigenstates of $\hat{J}_z$, the conduction electrons are carrying an increasing fraction of the impurity's angular momentum which is no longer negligible at $T \sim T_K$.

We first benchmark our NRG results against those of Ref. [105], where the total susceptibility χ_z^{cont} in the z-direction was calculated for systems with easy-plane and easy-axis anisotropy. Our NRG results, show excellent agreement with the results of that work. However, the reference did not include the total susceptibility in the x-direction χ_x^{cont}, which is a dynamical, rather than thermodynamic quantity, as $[\hat{H}, \hat{J}_x] \neq 0$. In this case, the computation of χ_x^{cont} is equivalent to calculating the entire spectral density function, which is a more involved process [106].

Fig. 3.2 shows the total susceptibilities $\chi_\gamma^{\text{cont}}$ for the same parameters of the anisotropic Kondo model ($S = 1$, $N = 1$, $g_\gamma = 0.1$, $\alpha = \pm 10^{-5}$) along both, the z-axis and directions in the xy-plane. Unlike in the weak-coupling regime where moment re-orientation can occur regardless of the sign of α, at strong coupling ($T \ll T_K$) we only observe a crossing of magnetic susceptibilities in the case of easy-plane anisotropy ($\alpha > 0$).

The crossing of total susceptibilities can be understood in terms of the subspaces with different total angular momentum J_z. Without Kondo screening the states are product states of the impurity and conduction electrons. We can divide the $J_z = 0$ subspace into sectors $(m,n) = (0,0), (1,-1), (-1,1)$, where m,n are the z-angular momenta of the impurity and conduction electrons, respectively. In the limit $T \ll \Lambda$, it costs energy to inject angular momentum into the Fermi sea and it costs

energy for the impurity to have $m \neq 0$. Hence, sectors $(1,-1),(-1,1)$ are higher in energy than the $(0,0)$ sector and Kondo exchange gives weak mixing between the sectors. For the $J_z = 1$ subspace the relevant sectors are $(m,n) = (1,0),(0,1)$. These are much closer in energy than $J_z = 0$ sectors, because the cost of injecting angular momentum into the Fermi sea can be offset by lowering the m quantum number of the impurity. The sectors resonate more strongly and Kondo exchange gives stronger mixing between them. As a result, the $J_z = 1$ subspace is lowered in energy more strongly than the $J_z = 0$ subspace, allowing for the possibility of a susceptibility crossing at $T \ll T_K$.

The negative susceptibility contributions at lowest temperatures in Fig. 3.2(a) result from the discretization of the conduction electron band in Wilson's NRG [107, 108]. This is equivalent to being away from the thermodynamic limit, where there is a finite number of conduction electron sites N_s, resulting in a non-zero Curie moment $T\chi$ of the free conduction electrons. When the impurity becomes entangled with the conduction electrons, it leads to a reduction of the conduction electron's Curie moment. This can lead to a negative contribution in the difference of total susceptibilities with and without the impurity. The susceptibility crossing takes place above the temperature where the contribution becomes negative and is robust against changes of the discretization. To some extent the numerical discretization mimics that in a realistic system there is a finite density of impurities and hence a finite number of conduction electron sites per impurity, even in the thermodynamic limit.

3.5 Conlusion and Discussion

We have presented a perturbative RG analysis of the single impurity Kondo model with single-ion anisotropy. Our main finding is that fluctuations near the Kondo temperature T_K can drive a reorientation of the moment away from the lattice favored direction at $T_0 > T_K$. This hard-direction ordering occurs over a wide range of parameters and for different types of anisotropy. As additional proof of principle, we have shown that a crossing of magnetic susceptibilities occurs in second-order

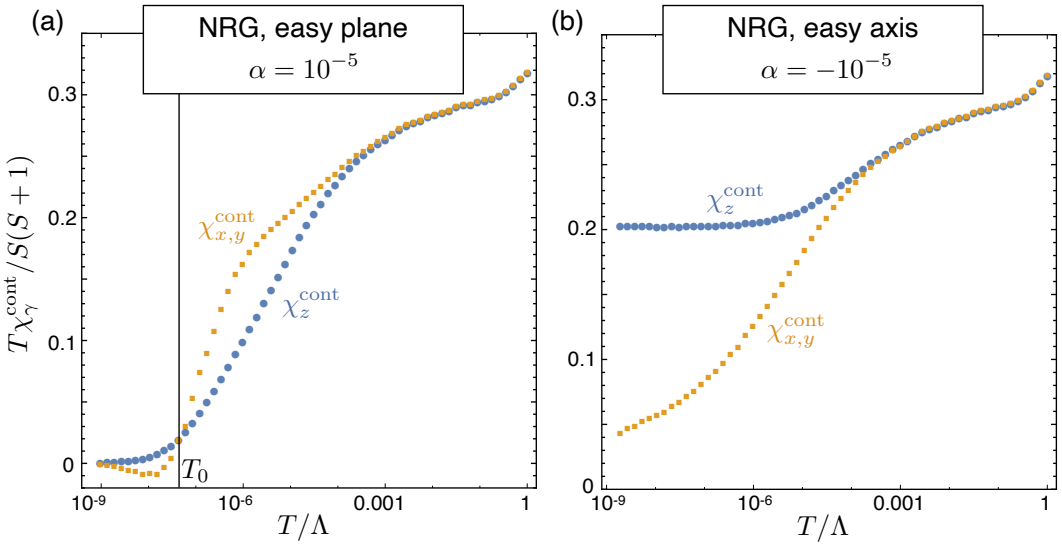

Figure 3.2: Impurity contribution to the susceptibility for the single-channel $S = 1$ Kondo models with $g_\gamma = 0.1$ and (a) easy-plane ($\alpha = 10^{-5}$) and (b) easy-axis ($\alpha = -10^{-5}$) anisotropies. Note that moment re-orientation, signalled by a crossing of the susceptibilities, only occurs in the case of easy-plane anisotropy.

perturbation theory, for all values of N and $S = 1$.

It is important to stress that magnetic hard-direction ordering could occur even at temperatures above T_0, since the RKKY interaction, $J_\gamma^{RKKY} \sim g_\gamma^2$, is significantly enhanced along the hard direction, e.g., for a system with easy plane anisotropy we find $g_z > g_xy$ significantly above T_0. As a result, the susceptibility along this direction would diverge first, giving rise to magnetic hard-direction ordering.

Using NRG, we investigated the strong-coupling behavior of the under-screened $S = 1$ single-channel Kondo model with single-ion anisotropy. We found that in this regime a crossing of magnetic susceptibilities can occur, but only in systems with easy-plane anisotropy. While the NRG results are robust at strong coupling, they crucially depend on the Hilbert space truncation and energy discretization in the intermediate temperature regime [105, 109], making it impossible to numerically resolve susceptibility crossings and compare with our perturbative calculations. One would expect that with increasing coupling strength the effect becomes more asymmetric and eventually only survives in systems with easy-plane anisotropy. This might explain why this case is more frequently observed in experiments [89]. It would be interesting to investigate the strong coupling behavior

of Kondo models with different S and N, as well as of closely related Coqblin-Schrieffer models, which better describe systems with strong spin-orbit coupling. For the latter, we found susceptibility crossings in perturbation theory and at strong coupling in the infinitely narrow band limit.

The mechanism presented here is rooted in the interplay of Kondo fluctuations and anisotropy on the single-impurity level. This would explain why hard-direction ordering is observed in a range of Kondo lattice systems, irrespective of the order and universality of the magnetic phase transition [89] and for both ferromagnetic [94, 95, 96, 97, 98, 99, 100, 101, 110, 111, 112, 113] and antiferromagnetic ordering [102, 103, 104].

Advances in Nanotechnology and scanning tunneling microscopy have led to a revival of the Kondo effect [114], thanks to unprecedented control on the level of single magnetic adatoms on metallic surfaces [115, 116, 117] or artificial magnetic elements in quantum dots [118, 119]. Such experiments could in principle probe the fluctuation-driven reorientation of a single magnetic impurity.

We argue that the magnetic hard-direction ordering observed in a wide range of Kondo materials is predominantly driven by strong Kondo fluctuations. This mechanism might be further enhanced by soft electronic particle-hole fluctuations that can lead to moment reorientation near ferromagnetic critical points [92]. Such a combined mechanism could be at play in $YbNi_4P_2$ which shows strong quantum critical fluctuations [98].

Our work shows that strong fluctuations in anisotropic Kondo materials can drive magnetic hard-direction ordering. It is to be expected that the interplay of collective critical fluctuations and Kondo physics will lead to many more unexpected ordering phenomena that are yet to be revealed.

Chapter 4

When Néel Criticality Meets Dirac Fermions

In the previous chapter, we have shown how the anisotropy in Kondo interactions can interplay with other magnetic anisotropies to induce crossings in magnetic susceptibilities which may eventually lead to ordering along the 'hard-axis'. This is a nice example of how fluctuations in electronic degree of freedom could affect the spins and account for exotic phenomena in the disordered phase. For such Kondo lattice materials, the RKKY effect will take over the control at low temperatures, leading to magnetic ordering. It is then natural to ask: how will the Kondo fluctuation affect the magnetic phase transition?

In this chapter, we consider such a Néel phase transition of two-dimensional quantum antiferromagnets, in which the spins are Kondo coupled to conduction electrons with Dirac dispersions. The low energy theory is a non-linear sigma model (NLσM) whose fields are coupled to Dirac fermions, forming a Gross-Neveu-Yukawa theory with non-linear order parameter fields. The presence of the Dirac fermions induces strong particle-hole fluctuations near the point-like Fermi surface, damping the long-wavelength propagator of the Goldstone modes. One would hence expect the Néel criticality to be significantly modified, or even destroyed by the fermion fluctuations. Surprisingly, using the momentum-shell renormalization group (RG) technique, we found that the Landau damping is weakly irrelevant at the Néel quantum critical point, even though the corresponding self-

energy correction dominates over the quadratic gradient terms in the IR limit. That is to say, the Néel quantum critical point is stable in the presence of Dirac fermions.

The original work in this chapter was published in *Stability of the Néel quantum critical point in the presence of Dirac fermions*, H. Hu, J. Lin, M. D. Uryszek, F. Krüger, Physical Review B 107 (8), 085113.[120]

4.1 Introduction

The discovery of topological insulators [121, 122] has initiated an explosion of research into Dirac or Weyl semimetals and topological aspects of electronic band-structures [123, 124, 125, 126]. Dirac fermions with relativistic dispersion around point-like Fermi surfaces can arise as low-energy excitations of weakly interacting electron systems. The most prominent example is graphene, which can be described by a tight-binding model of electrons on the half-filled honeycomb lattice. More recently, it was realized that strong correlations in heavy-fermion systems, resulting in the hybridization between conduction electrons and heavy f electron bands, can give rise to topological Kondo insulators [127, 128] or topologically protected Weyl-Kondo semimetals in three-dimensional crystals without inversion symmetry [129, 130].

Because of their point-like Fermi surfaces nodal semi- metals provide the simplest setting to study fermionic quantum criticality. While Dirac semimetals are stable against weak repulsive interactions, a consequence of the vanishing density of states at the Fermi level, sufficiently strong short-range interactions can give rise to a range of competing instabilities. For the extended Hubbard model on the half-filled honeycomb lattice rich phase diagrams were established [131, 132, 133, 134, 135, 136, 137, 138, 139, 140], showing antiferromagnetic, charge ordered, Kekule and topological Haldane phases. The symmetry-breaking transitions are accompanied by the opening of a gap in the electronic spectrum.

Since the fermionic particle-hole excitations are gapless at such quantum phase transitions, the critical behavior falls outside the Ginzburg-Landau-Wilson paradigm of a pure order parameter description [141]. Instead, the nature of the tran-

sitions can be studied within a field theory that describes the coupling of the bosonic order parameter field, which is introduced through a Hubbard-Stratonovich decoupling of the interaction vertex, to the gapless Dirac fermions [142, 143, 144]. This is known as the Gross-Neveu-Yukawa (GNY) theory, which describes chiral symmetry breaking and spontaneous mass generation in high-energy physics [145, 146]. At the fermion-induced GNY fixed point, the fermions acquire an anomalous dimension, resulting in the fermion spectral functions with branch cuts rather than quasiparticle poles [143]. Such non-Fermi liquid behavior is the hallmark of fermionic quantum criticality.

Far below the upper critical dimension, the GNY model can be analyzed in the limit of a large number N_f of Dirac fermion flavors, which allows for a systematic calculation of critical exponents in powers of $1/N_f$, using techniques from particle physics [147, 148, 149, 150, 151, 152]. In the condensed matter language, the correct IR scaling form of the bosonic propagator can be understood in terms of Landau damping of long-wavelength order parameter fluctuations by electronic particle-hole fluctuations [56]. For Dirac fermions in $D = d + 1$ space-time dimensions, this results in a self-energy correction $\Pi(\mathbf{k}, \omega) \sim (\mathbf{k}^2 + \omega^2)^{(D-2)/2}$ to the inverse boson propagator [153]. For $D < 4$, below the upper critical dimension, the self-energy contribution dominates over the regular quadratic gradient terms in the IR limit. In order to correctly describe the universal critical behavior, the dressed RPA order-parameter propagator needs to be used as input for subsequent momentum-shell RG calculations [56].

In this chapter we consider a field theory in two spatial dimension that is very similar to the GNY theory for the antiferromagnetic phase transition on the half-filled honeycomb lattice, driven by an on-site Hubbard repulsion. However, here we consider a situation where the dynamical order parameter field is not generated through a Hubbard-Stratonovich transformation of a fermion interaction, but is instead given by the Néel order parameter field $\vec{N}$ of a local-moment quantum antiferromagnet. While the Kondo coupling between local moments and Dirac electrons takes precisely the form of the Yukawa coupling of the GNY theory, there are crucial

differences in the bosonic sector of the field theory. The Néel transition of a two-dimension quantum antiferromagnet is described by a quantum non-linear σ model (NLσM) [154, 155] that describes spatial and temporal fluctuations of a unit vector field $\vec{N}$, corresponding to long-wavelength, transverse spin-wave fluctuations. As we will show later, because of the constraint of the NLσM the critical behavior is very different from that of the GNY theory.

The outline of this chapter is as follows. In Sec. 4.2 we introduce the RG of the original NLσM in 2+1 space-time dimensions as a warm-up. Unlike the ϕ^4 model, the ε expansion is done near the lower critical dimension, where the model is asymptotically free. The Kondo coupling to Dirac fermions is included in Sec. 4.3. In Sec. 4.3.2 we discuss the importance of Landau damping of the Néel order parameter fluctuations by low-energy electronic particle-hole fluctuations, and analyze the Landau-damped NLσM. Using momentum-shell RG, we demonstrate that Landau damping is weakly irrelevant at the Néel quantum critical point but increases in the ordered state, indicating that spin-wave excitations are damped. The full set of RG equations, including the Yukawa coupling, are derived in Sec. 4.3.3 and analyzed in Sec. 4.3.4. We show that while the Yukawa coupling is weakly relevant at the Néel quantum critical point, sufficiently strong Landau damping renders the critical point quasi-stable for any realistic system size for $N_f \geq 4$ and thermodynamically stable for $N_f < 4$. In the latter case, a new multi-critical point captures the transition between Néel critical and Kondo run-away regimes. We analyze the universal critical behavior associated with this fixed point. As demonstrated in Sec. 4.3.5, the behavior in $D = 3$ space-time dimensions is not accessible within an ε-expansion above the lower critical dimension, $D = 2 + \varepsilon$. Finally, in Sec. 4.4 we summarize and discuss our results.

4.2 Néel Quantum Criticality

The long-wavelength behaviour of the antiferromagnetic phase transition of the quantum Heisenberg model can be described by the $O(3)$ quantum non-linear σ model [156, 157]. Here we briefly introduce the derivation from a microscopic

Heisenberg model to the field theory and derive the RG equations associated with the critical point.

4.2.1 Non-Linear σ Model

We start with a generic spin Hamiltonian for a quantum antiferromagnet on a bi-partite lattice in d-dimensions, e.g. a hypercubic lattice,

$$\hat{H}_{\rm loc} = J \sum_{\langle i,j \rangle} \hat{\boldsymbol{S}}_i \cdot \hat{\boldsymbol{S}}_j + \cdots \tag{4.1}$$

where $\hat{\boldsymbol{S}}_i$ denotes a spin-S operator on lattice site i, the sum is over nearest-neighbour bonds, and $J > 0$ denotes the antiferromagnetic superexchange between neighbouring sites. The ellipsis in Eq. (4.1) denote longer-range couplings or ring exchanges that frustrate the Néel order and might be tuned to drive the system towards a quantum phase transition.

As a next step, we express the Heisenberg model $\hat{H}_{\rm loc}$ in terms of an imaginary-time path integral over spin-coherent states $|\vec{N}_i(\tau)\rangle$, which satisfy $\hat{\boldsymbol{S}}_i|\vec{N}_i(\tau)\rangle = S_i\vec{N}_i(\tau)|\vec{N}_i(\tau)\rangle$, and decompose the unit-vector fields $\vec{N}_i(\tau)$ into the staggered Néel order parameter field $\vec{n}_i(\tau)$ and fluctuations $\vec{L}_i(\tau) \perp \vec{n}_i(\tau)$,

$$\vec{N}_i(\tau) = \varepsilon_i \vec{n}_i(\tau)\sqrt{1 - a^{2d}\vec{L}_i^2(\tau)} + a^d \vec{L}_i(\tau), \tag{4.2}$$

where $\varepsilon_i = +1$ on sublattice A and $\varepsilon_i = -1$ on sublattice B of the bi-partite lattice, and a denotes the lattice constant. After taking the continuum limit, we obtain the action

$$S_{\rm loc}[\vec{n},\vec{L}] \;=\; \frac{1}{2}\int_0^\infty d\tau \int d^d\mathbf{r} \left\{ \rho_S \left(\nabla \vec{n}\right)^2 + \chi_\perp \vec{L}^2 \; - 2iS\vec{L}\cdot\left(\vec{n}\times\partial_\tau \vec{n}\right) \right\},$$

where the spin stiffness and transverse spin susceptibility for the d dimensional hypercubic lattice are given by $\rho_S = JS^2 a^{2-d}$ and $\chi_\perp = 2JS^2 d a^d$, respectively. The last term in $S_{\rm loc}$ is the smooth contribution from the Berry phase. For the AFM phase transition, this term can be neglected. However, it is worth noticing that this term

plays a crucial role in skyrmion generations and the possible deconfined quantum critical point of the Heisenberg model on certain lattices which drives the system into a resonant valence bond (RVB) state [10].

Since the $\vec{L}$ field is massive, it can be integrated out through a Gaussian integral. Carrying out the integral over the massive $\vec{L}$ field, we obtain the final action for the staggered Néel order parameter field $\vec{n}$,

$$S[\vec{n}] = \frac{1}{2g}\int_0^\infty d\tau \int d^d\mathbf{r}\left\{(\nabla\vec{n})^2 + \frac{1}{c^2}(\partial_\tau\vec{n})^2\right\}. \tag{4.3}$$

This is the so-called NLσM, whose non-linearity is enforced through the constraint $\vec{n}^2 = 1$. Here $g = 1/\rho_S$ is the inverse spin stiffness and $c = JSa\sqrt{2}$ is the spin-wave velocity.

4.2.2 Field Decomposition

Before running the RG scheme, the non-linear constraint needs to be taken care of. The partition function in the path integral language reads

$$\begin{aligned} Z &= \int \mathscr{D}\vec{n}\delta(\vec{n}^2 - 1)e^{-S[\vec{n}]}, \\ S[\vec{n}] &= \frac{1}{2g}\int d^D x\,(\nabla\vec{n})^2, \end{aligned} \tag{4.4}$$

where we have rescaled the temporal and spatial coordinates to the dimensional units:$x = (x_0, \mathbf{x})$, where $x_0 = \Lambda c\tau,\ \mathbf{x} = \Lambda\mathbf{r}$. The cutoff Λ is set to be one for simplicity. To incorporate the constraint in the calculation, we then apply the standard trick used in [158]. Generally speaking, for the $O(N)$ NLσM, one can single out the component σ along the direction that the system orders, and write the fields as $\vec{n} = (\vec{\pi}, \sigma)$. Since σ is the ordering direction, one can assume the fluctuation along this direction to be small, and use the constraint to rewrite the component by the left $N-1$ components: $\sigma = \sqrt{1-\vec{\pi}^2}$. The delta function in the partition function can then be used to eliminate the σ component, leaving us a theory of $\vec{\pi}$ fields with

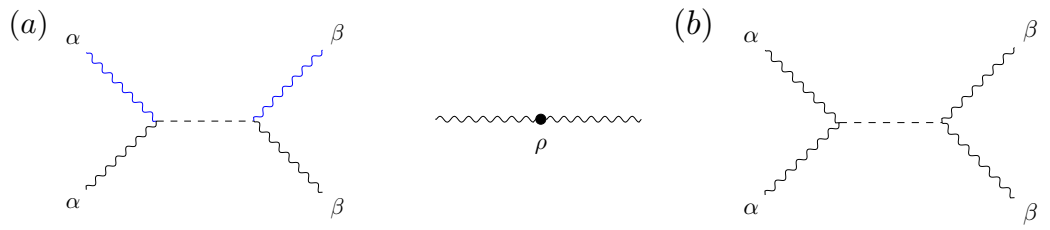

Figure 4.1: The vertices included in the non-linear σ model after the field decomposition. (a) The first diagram is the four-boson interaction vertex of the $\vec{\pi}$ fields, where the two blue lines represent the ones with the gradient. The mass-like term of the $\vec{\pi}$ fields is shown in the second diagram. (b) The four-boson interaction generated from the inclusion of an artificial magnetic field.

$N-1$ components:

$$\begin{aligned} Z &= \int \mathscr{D}\vec{\pi} \int \mathscr{D}\sigma \prod_x \delta(\sigma^2+\vec{\pi}^2-1) e^{-S[\vec{\pi},\sigma]} \\ &= \int \mathscr{D}\vec{\pi} \int \mathscr{D}\sigma \prod_x \frac{\delta(\sigma-\sqrt{1-\vec{\pi}^2})}{2\sigma} e^{-S[\vec{\pi},\sigma]} \\ &= \int \mathscr{D}\vec{\pi} \prod_x (\frac{1}{2\sqrt{1-\vec{\pi}^2}})^{\rho d^D x} e^{-S[\vec{\pi}]} \\ &= \int \mathscr{D}\vec{\pi} e^{-S'[\vec{\pi}]}, \end{aligned}$$

with the action

$$\begin{aligned} S'[\vec{\pi}] &= \frac{1}{2g}\int d^D x \left[((\nabla\vec{\pi})^2 + \left(\nabla\sqrt{1-\vec{\pi}^2}\right)^2 \right] - \rho \int d^D x \ln \frac{1}{2\sqrt{1-\vec{\pi}^2}} \\ &\approx \frac{1}{2g}\int d^D x \left[(\nabla\vec{\pi})^2 + (\vec{\pi}\cdot\nabla\vec{\pi})^2 \right] - \frac{\rho}{2}\int d^D x\, \vec{\pi}^2. \end{aligned} \tag{4.5}$$

The second line is obtained by a Taylor expansion of the square root and the log up to the leading order in $\vec{\pi}$. By eliminating one component of the Néel vector field, the Dirac function in the measure gives rise to an extra mass-like term in the action, where ρ is the density of states. As it will become clear later, this term is crucial to the correct physics. The corresponding vertices are shown in fig 4.1(a). The blue boson fields in the first diagram correspond to the two $\vec{\pi}$ fields with the gradient.

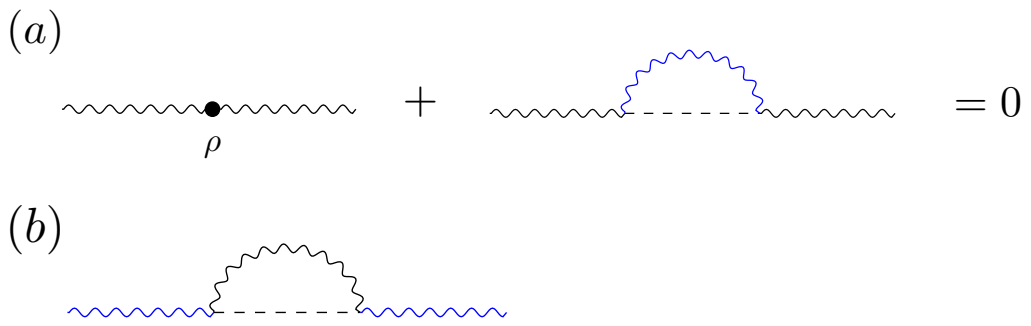

Figure 4.2: Feynman diagrams used in the RG calculation of the NLσM. (a) Contribution from the one-loop diagram which contracts the two blue boson lines exactly cancels the contribution from the mass-like term generated from the field decomposition. As a result, no mass term is generated under RG. (b) The one-loop diagram that corrects the bare propagator.

4.2.3 Renormalisation Group Analysis

The standard momentum-shell RG can be applied to study the criticality. To do so, we first Fourier transform the action to frequency-momentum space. The resulting action has the form

$$S'[\vec{\pi}] = \frac{1}{2g}\int_k k^2 \vec{\pi}(k)\cdot\vec{\pi}(-k) - \frac{\rho}{2}\int_k \vec{\pi}(k)\cdot\vec{\pi}(-k) \\ -\frac{1}{2g}\sum_{\alpha\beta}\int_{k_1k_2k_3k_4}\delta(k_1+k_2+k_3+k_4)(k_2\cdot k_4)\pi_\alpha(k_1)\pi_\alpha(k_2)\pi_\beta(k_3)\pi_\beta(k_4), \tag{4.6}$$

where $k=(\omega,\vec{k})$ is the frequency-momentum vector. From the kinetic term one can obtain the propagator of the Néel vector fields as the inverse of the kernel:

$$\langle\pi_\alpha(k)\pi_\beta(k')\rangle_0 = \frac{g}{k^2}\delta_{\alpha\beta}\delta(k+k'). \tag{4.7}$$

We then use a symmetric scheme by performing the shell integrals over a spherical frequency-momentum shell, which treats the frequency and momenta on equal footing. It is worth emphasizing that applying the cutoff on the frequency/imaginary time axis won't affect the physics that we are interested here, as the universal behaviour of the theory should not be aware of any effect from the cutoff

scheme. Following the standard approach, we rescale the frequency and momenta as $\vec{k} \to \vec{k}e^{dl}, \omega \to e^{zdl}$, and the order parameter fields as $\vec{\pi} \to \vec{\pi}e^{\Delta dl}$, with Δ being the scaling dimension of the $\vec{\pi}$ fields. Note that all the terms are local, which means the whole theory is Lorentz invariant, and the dynamical exponent z does not flow under RG. In this case, the only flowing parameters are the inverse spin stiffness g and the mass. Since the $1/(2g)$ factor appears in the kinetic term, its RG flow can be obtained by just calculating the self-energy diagram. The related Feynman diagrams are shown in Fig 4.2. The mass renormalisation from the one-loop diagram is

$$\begin{aligned}
&-\frac{1}{2g}\sum_{\alpha\beta}\int_{k_1k_2}^{<}\int_{q_1q_2}^{>}\delta(k_1+k_2+q_1+q_2)q_1\cdot q_2\pi_\alpha(k_1)\pi_\beta(k_2)\langle\pi_\alpha(q_1)\pi_\beta(q_2)\rangle_0 \\
=&-\frac{1}{2}\int_k^{<}\int_q^{>} q\cdot(-q)\vec{\pi}(k)\cdot\vec{\pi}(-k)\frac{1}{q^2} \\
=&\,\delta m^2\int_k^{<}\vec{\pi}(k)\cdot\vec{\pi}(-k),
\end{aligned} \tag{4.8}$$

where

$$\delta m^2 = \frac{1}{2}\int^{>}\frac{d^Dq}{(2\pi)^D} = \frac{1}{2}\frac{S_D}{(2\pi)^D}\int_{e^{-dl}}^{1} dq\, q^{D-1} = \frac{S_D}{2(2\pi)^D}dl. \tag{4.9}$$

$S_D = 2\pi^{\frac{D+1}{2}}/\Gamma(\frac{D+1}{2})$ is the surface area of a D-sphere. However, note that the density of states ρ that appears in the mass-like term derived from the non-linear measure can be expressed as an integral over the Brillouin Zone: $\rho = \frac{N_s}{V_{BZ}} = \int\frac{d^Dk}{(2\pi)^D}$, hence the term is rescaled as

$$\begin{aligned}
&-\frac{1}{2}\frac{S_D}{(2\pi)^D}\int_{e^{-dl}}^{1} dq\, q^{D-1}\int_k^{<}\vec{\pi}(k)\cdot\vec{\pi}(-k) \\
=&-\frac{1}{2}\frac{S_D}{(2\pi)^D}dl\int_k^{<}\vec{\pi}(k)\cdot\vec{\pi}(-k).
\end{aligned} \tag{4.10}$$

This contribution exactly cancels out δm^2, leaving the boson fields massless. Physically speaking it makes perfect sense, since the Néel order parameter fields are Goldstone modes generated due to the spontaneous breaking of the $SO(3)$ rotational symmetry of the spin, and therefore should remain gapless under RG.

The bosonic self-energy diagram is obtained by contracting the two boson

lines without derivatives, as shown in Fig.4.2(b). The contribution has the form $\delta_g \int_k^< k^2 \vec{\pi}(k)\cdot\vec{\pi}(-k)$, with the shell integral $\delta_g = -\frac{1}{2g}\int_q^> \frac{g}{q^2} = \frac{S_D}{2(2\pi)^D}dl$. The RG equation of the inverse stiffness g can then be easily derived by rescaling everything back to the original cutoff:

$$\begin{aligned}
&\left(\frac{1}{2g(l)} + \frac{S_D}{2(2\pi)^D}dl\right)\int_k^< k^2\vec{\pi}(k)\cdot\vec{\pi}(-k)\\
=&e^{(D+2-2\Delta)}\left(\frac{1}{2g(l)} + \frac{S_D}{2(2\pi)^D}dl\right)\int_k k^2\vec{\pi}(k)\cdot\vec{\pi}(-k)\\
\approx&\left(\frac{1}{2g(l)} - \frac{D+2-2\Delta}{2g(l)}dl + \frac{S_D}{2(2\pi)^D}dl\right)\int_k k^2\vec{\pi}(k)\cdot\vec{\pi}(-k)\\
\equiv&\frac{1}{2g(l+dl)}\int_k k^2\vec{\pi}(k)\cdot\vec{\pi}(-k),\\
\Longrightarrow&-\frac{D+2-2\Delta}{2g}dl + \frac{S_D}{2(2\pi)^D}dl = -\frac{1}{2g^2}\frac{dg}{dl}dl\\
\Longrightarrow&\frac{dg}{dl} = (D+2-2\Delta)g - \frac{S_D}{(2\pi)^D}g^2.
\end{aligned} \tag{4.11}$$

However, one still needs to determine the scaling dimension Δ of the $\vec{\pi}$ fields. Unlike the ϕ^4 theory, NLSM has the inverse spin stiffness g in both the kinetic term and the interaction. Therefore we can not obtain Δ by simply keeping the kinetic term from flowing. The proper way to get Δ is to first derive the corrections to the interacting term, which will be another RG equation for g, and then demand the two RG equations to be the same and solve for Δ. In doing so one will have to evaluate all the one-loop diagrams that correct $(\vec{\pi}\cdot\nabla\vec{\pi})$. Without the help of the large-N theory, there are more than a dozen related Feynman diagrams. Though many of the diagrams cancel with each other, the calculation is still tedious. Alternatively, Nelson and Pelcovits[158] managed to circumvent the difficulty by introducing a fictitious magnetic field to the Néel order parameter fields. The idea is that the scaling of a magnetic field should be trivial under RG. By calculating the scaling relation of the magnetic field, we get another equation which can be combined with the RG equation of g to help us fix Δ. If we apply the magnetic field along the ordering direction σ, then through the previous field decomposition we can again following the same analysis above, and write down a theory of $\vec{\pi}$ fields, only with additional

quadratic and quartic terms:

$$\begin{aligned}
-\frac{h}{g}\int d^D x\sigma &= -\frac{h}{g}\int d^D x\sqrt{1-\vec{\pi}^2} \\
&\approx \frac{h}{2g}\int d^D x\ \vec{\pi}^2 + \frac{h}{8g}\int d^D x\ \vec{\pi}^4 \\
&= \frac{h}{2g}\int_k \vec{\pi}(k)\vec{\pi}(-k) \\
&\quad + \frac{h}{8g}\int_{k_1k_2k_3k_4} \delta(k_1+k_2+k_3+k_4)\,(\vec{\pi}(k_1)\cdot\vec{\pi}(k_2))\,(\vec{\pi}(k_3)\cdot\vec{\pi}(k_4))
\end{aligned} \tag{4.12}$$

Since there is a quadratic term, the RG equation of h can be calculated by evaluating the diagrams that correct this term, which are similar to the ones we calculated above. The one-loop diagrams after the inclusion of a magnetic field are shown in fig 4.3. The quadratic term derived in eq.4.12 adds to the pure NLSM, giving the field-dependent propagator

$$\langle\pi_\alpha(k)\pi_\beta(k')\rangle_0 = \frac{g}{k^2+h}\delta_{\alpha\beta}\delta(k+k'). \tag{4.13}$$

As a result, the previously calculated Δm^2 is modified accordingly. However, the ρ term from the non-linear measure stays the same as the no-field case under RG. One can then check that, the cancellation still holds once the additional mass term from the new vertex is included. This is shown in fig 4.3(a).

The field renormalisation is obtained through the diagram in fig 4.3(c):

$$\begin{aligned}
&\delta h\int_k^< \vec{\pi}(k)\cdot\vec{\pi}(k) \\
=&2\times\frac{h}{8g}\int_{k_1k_2}^<\int_{q_1q_2}^> \delta(k_1+k_2+q_1+q_2)\sum_{\alpha\beta}\pi_\alpha(k_1)\pi_\alpha(k_2)\langle\pi_\beta(q_1)\pi_\beta(q_2)\rangle_0 \\
=&\frac{h}{4(1+h)}(N-1)\frac{S_D}{(2\pi)^D dl}\int_k^< \vec{\pi}(k)\cdot\vec{\pi}(k).
\end{aligned} \tag{4.14}$$

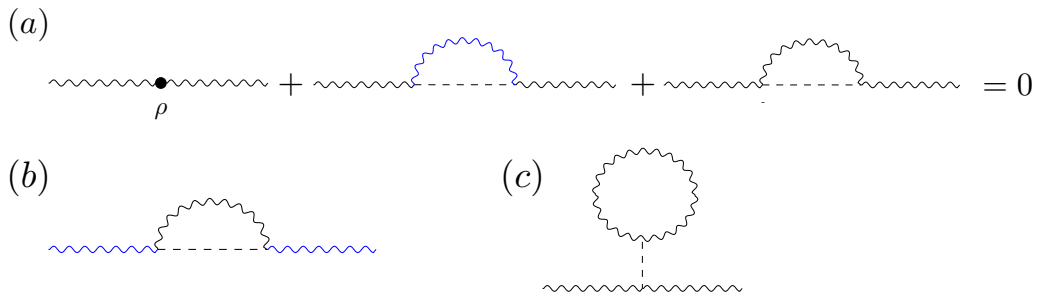

Figure 4.3: One-loop diagrams correspond to the NLSM with a magnetic field. (a) Under the magnetic field the propagator of the order parameter field depends also on h. Therefore the diagrammatic cancellation now involves a third diagram generated from the new vertex. (b) The diagram that corrects the bosonic propagator. (c) The diagram that generates the mass, corresponding to the renormalisation of the magnetic field h.

Combining the tree-level scaling, we can derive the RG equations for h:

$$\begin{aligned}\frac{d}{dl}\left(\frac{h}{2g}\right) &= -(D-2\Delta)\frac{h}{2g} + \delta h \\ &= -(D-2\Delta)\frac{h}{2g} + \frac{N-1}{2}\frac{S_D}{(2\pi)^D}\frac{h}{1+h} \\ &\equiv \Delta\frac{h}{2g}.\end{aligned}$$

In the last line, we use the fact that the magnetic field is a 'mass' term that renormalises trivially under RG. In other words, it should renormalise in the same way as the order parameter fields. Solving the equation gives the scaling dimension Δ of fields π:

$$\Delta = d - \frac{N-1}{2}\frac{S_D}{(2\pi)^D}\frac{g}{1+h}. \tag{4.15}$$

Happily setting $h = 0$, and plugging eq.4.15 back into eq.4.11, we finally obtain the RG equation for g:

$$\frac{dg}{dl} = (2-D)g + (N-2)\frac{S_D}{(2\pi)^D}g^2. \tag{4.16}$$

One can immediately see that for $D = 2+\varepsilon$ and $N = 3$, there exists a non-trivial unstable fixed point at $g_c \approx 2\pi\varepsilon$. This is the Néel fixed point that governs the antiferromagnetic phase transition. For $g < g_c$, the system flows to the Gaussian fixed point, corresponding to the spin-disordered case, and for $g > g_c$, the AFM order is

stabilised as the system approaches the frozen spin limit. (Of course, the latter part falls out of the framework of the perturbative RG once $g \to O(1)$.)

4.3 Inclusion of Dirac Fermions

4.3.1 The model

Now we include the Kondo coupling between the spins and Dirac fermions and study the impact of the latter to the Néel quantum criticality. Our starting model is a $(2+1)d$ NLσM whose vector fields $\vec{N}$ are coupled to N_f copies of two-component Dirac electrons via the conventional Yukawa coupling. On a microscopic level, this model could be realized in the low-energy limit of a quantum antiferromagnet on the honeycomb lattice with Kondo coupling to noninteracting electrons that move on either the same or adjacent honeycomb lattice at half-filling. For this realization we would have $N_f = 4$ due to twofold spin and valley degeneracies. The effective continuum field theory at zero temperature is given by the imaginary-time path integral over the action $S = S_f + S_N + S_Y$, with contributions

$$\begin{aligned} S_f &= \int_{\mathbf{q},\omega} \overline{\boldsymbol{\psi}}(\mathbf{q},\omega) \left(-i\frac{\omega}{v_F} + q_x\tau_x + q_y\tau_y \right) \boldsymbol{\psi}(\mathbf{q},\omega), \\ S_N &= \frac{1}{2g} \int d^2\mathbf{r} \int_0^\infty d\tau \left\{ (\nabla\vec{N})^2 + \frac{1}{c^2}(\partial_\tau \vec{N})^2 \right\}, \\ S_Y &= \frac{\lambda}{\sqrt{N_f}} \int d^2\mathbf{r} \int_0^\infty d\tau \overline{\boldsymbol{\psi}} \left(\vec{N}\cdot\vec{\sigma}\otimes\tau_z \right) \boldsymbol{\psi}, \end{aligned} \tag{4.17}$$

where S_f describes two-dimensional Dirac fermions with Fermi velocity v_F, written in terms of fermionic Grassmann fields $\boldsymbol{\psi}$. The term S_N is the conventional NLσM in terms of the staggered three-component Néel order parameter field $\vec{N}(\mathbf{r},\tau)$ which satisfies the constraint $\vec{N}^2(\mathbf{r},\tau) = 1$, as discussed in the previous section. The last contribution S_Y is the Yukawa coupling between the local moments and Dirac electrons. Here $\vec{\sigma}$ is the vector of spin Pauli matrices, while the Pauli matrices τ_α act on sub-lattice space. Note that since $\vec{N}$ describes the staggered magnetization the coupling has an opposite sign on the two sublattices, resulting in the additional τ_z. The low-energy continuum field theory is subject to a UV momentum cut-off, $|\mathbf{q}| \leq \Lambda$,

corresponding to the finite size of the Brillouin Zone.

The field theory is very similar to the Heisenberg GNY theory in Chapter 3. However, a crucial difference is the constraint of the NLσM which has important consequences for the universal critical behavior. As pointed out in the context of GNY theories, the Landau damping of the bosonic order parameter fluctuations by electronic particle-hole fluctuations gives rise to a self-energy contribution

$$\Pi(\mathbf{q},\omega) = \gamma\sqrt{\mathbf{q}^2 + \omega^2/v_F^2} \tag{4.18}$$

to the inverse boson propagator in two spatial dimensions. This non-analytic self-energy correction arrises from the diagram in Fig. 4.4(a) from integration of fermion modes near zero momenta and frequency. It is therefore not generated within the momentum shell RG, but needs to be included to correctly capture the universal critical behavior of GNY theories [56, 153]. The form of the Landau damping does not depend on the number of order parameter components and is not affected by the fixed-length constraint of the Néel order parameter field. Note that although the bare Landau damping parameter γ_0 is determined by the square of the bare Yukawa coupling, $\gamma_0 \sim \lambda_0^2$, this relation is not preserved under the RG. We therefore treat γ and λ as independent coupling constants.

Under the RG there will be a non-trivial flow of the velocities c and v_F. For simplicity, we will focus on the case $v_F = c$, which is preserved under the RG. For convenience, we rescale to dimensionless momenta $\mathbf{k} = \mathbf{q}/\Lambda$ and frequencies $k_0 = \omega/(c\Lambda)$ and absorb the additional prefactors in a redefinition of the coupling constants. Since both the order parameter and fermion sectors are relativistic and frequency and momenta enter the zero-temperature field theory in the same way, the quantum critical behaviour will be described by a dynamical exponent $z = 1$. We will therefore treat frequency and momenta on an equal footing and impose an isotropic cut-off in 2+1 dimensions, $\sqrt{\mathbf{k}^2 + k_0^2} \leq 1$. Note that the universal critical behavior is independent of the choice of the UV cut-off scheme.

4.3.2 Landau Damped NLσM

We start by investigating the effects of Landau damping on the Néel transition in the case of vanishing Yukawa coupling, $\lambda = 0$. Our starting point is the NLσM

$$S_N = \frac{1}{2g}\int_k \Omega^{-1}(k)\vec{N}(k)\cdot\vec{N}(-k), \tag{4.19}$$

where we have defined $k = (\mathbf{k}, k_0)$ and $\int_k = \int \frac{dk_0}{2\pi}\int \frac{d^2\mathbf{k}}{(2\pi)^2}$, subject to the cut-off $|k| \leq 1$, for brevity, and include the Landau damping γ in the inverse propagator,

$$\Omega^{-1}(k) = k^2 + \gamma|k| = \mathbf{k}^2 + k_0^2 + \gamma\sqrt{\mathbf{k}^2 + k_0^2}. \tag{4.20}$$

We use the same decomposition scheme showed in sec.4.2.2 to single out the ordering direction $\vec{N} = (\vec{\pi}, \sigma)$ and use the constraint $\sigma(\mathbf{r},\tau) = \sqrt{1-\vec{\pi}^2(\mathbf{r},\tau)}$ to eliminate σ and derive an effective action in terms of the transverse fields $\vec{\pi}$. Since the form of Landau damping is defined in momentum space, we need the Fourier transform of the constraint: $\sigma(k) = \delta(k) - \frac{1}{2}\int_q \vec{\pi}(q)\vec{\pi}(k-q)$. This results in the effective action

$$\begin{aligned} S_N &= \frac{1}{2g}\int_k \Omega^{-1}(k)\vec{\pi}(k)\cdot\vec{\pi}(-k) - \frac{\rho}{2}\int_k \vec{\pi}(k)\cdot\vec{\pi}(-k) \\ &+ \frac{1}{16g}\int_{k_1,\ldots,k_4} \delta(k_1+k_2+k_3+k_4)\left[\Omega^{-1}(k_1+k_2)\right. \\ &\left. +\Omega^{-1}(k_3+k_4)\right]\left[\vec{\pi}(k_1)\cdot\vec{\pi}(k_2)\right]\left[\vec{\pi}(k_3)\cdot\vec{\pi}(k_4)\right], \end{aligned} \tag{4.21}$$

where ρ is the density and the corresponding term arises from exponentiation and expansion of $1/(2\sqrt{1-\vec{\pi}^2(\mathbf{r},\tau)})$ from the path-integral measure. Note that the Landau-damped propagator also enter the form of the four-boson interaction through the Taylor expansion and alters the simple gradient form in the bare NLSM in eq.4.6.

We integrate out modes with momenta and frequencies from an infinitesimal shell near the cut-off, $e^{-d\ell} \leq \sqrt{\mathbf{k}^2 + k_0^2} \leq 1$, followed by a rescaling of momenta, $\mathbf{k} \to \mathbf{k}e^{d\ell}$, and frequencies, $k_0 \to k_0 e^{zd\ell}$, with dynamical exponent $z = 1$. In addition,

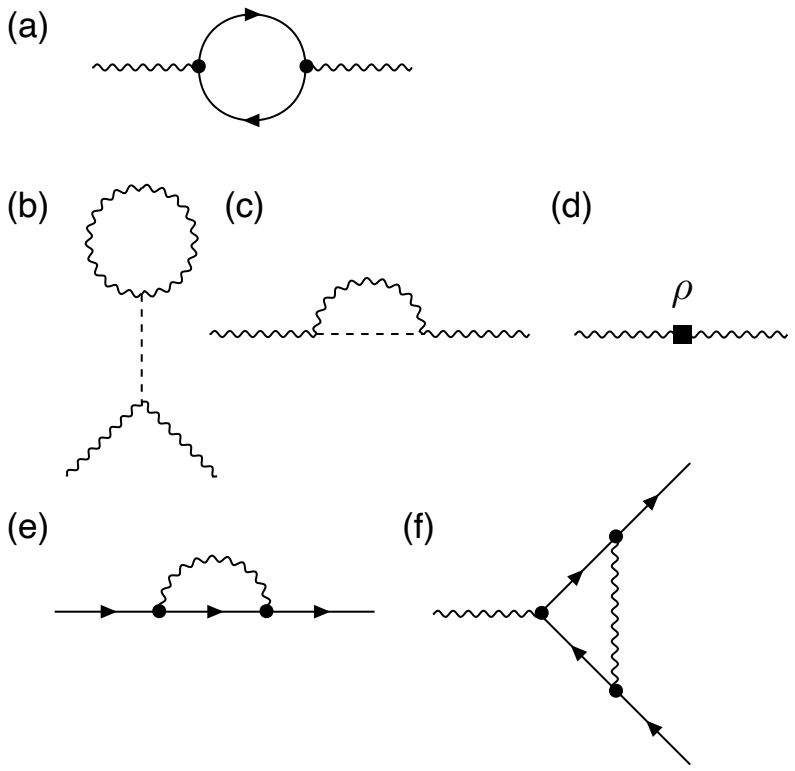

Figure 4.4: One-loop diagrams relevant to our RG calculation. Solid lines represent fermionic degrees of freedom, wiggly lines the bosonic order parameter fields. (a) The fermionic bubble diagram integrated over small momenta and frequencies gives rise to the non-analytic Landau damping of long-wavelength order parameter fluctuations. The momentum-shell contribution of this diagram contributes to the renormalization of the coupling constant g of the NLσM. (b)-(d) Diagrams relevant for the RG of the Landau-damped NLσM. The diagram (b) is identical to zero, (c) renormalizes the quadratic gradient terms and hence the coupling constant g. The unphysical mass term generated by (c) is cancelled by the contribution (d) from the functional integral measure. (e) The fermionic self-energy diagram renormalizes the overall prefactor of the free fermion action S_f. The scaling dimension of the fermion fields is determined such that the prefactor remains constant. (f) Diagram contributing to the renormalization of the Yukawa coupling λ.

we rescale the transverse spin-fluctuation fields as $\vec{\pi}(k) \to \vec{\pi}(k)e^{-\Delta_\pi d\ell}$.

At one-loop order, the contraction of two order parameter fields,

$$\langle \pi_\alpha(k)\pi_\beta(k')\rangle_0 = g\delta_{\alpha\beta}\delta(k+k')\Omega(k), \tag{4.22}$$

gives rise to the renormalization of the quadratic action by the quartic vertex. The diagram in Fig. 4.4(b) vanishes because of $\Omega^{-1}(0) = 0$. The diagram shown in

Fig. 4.4(c) gives rise to a term $\sim k^2\vec{\pi}(k)\cdot\vec{\pi}(-k)$ and hence a renormalization of the coupling constant g. In addition, it produces a mass term $\sim\vec{\pi}(k)\cdot\vec{\pi}(-k)$ which cancels exactly with the trivial term from the reduction of the density ρ by the shell contribution [Fig. 4.4(d)]. Evaluating the momentum shell and frequency integrals and combining with the rescaling contributions, we obtain the RG equations

$$\frac{d}{d\ell}\left(\frac{1}{2g}\right) = (-5+2\Delta_\pi)\frac{1}{2g}+\frac{1}{(2\pi)^2}\frac{1+\gamma/3}{1+\gamma}, \tag{4.23}$$

$$\frac{d}{d\ell}\left(\frac{\gamma}{2g}\right) = (-4+2\Delta_\pi)\frac{\gamma}{2g}. \tag{4.24}$$

The scaling dimension Δ_π of the transverse spin-fluctuation fields needs to be determined such that the constraint of the NLσM is satisfied on all scales. This is only the case if the coupling constant g in front of the quartic vertex renormalizes in exactly the same way as the g in front of the quadratic action. Instead of evaluating the second-order, one-loop diagrams that renormalize the vertex, we employ a trick invented by Nelson and Pelcovits [158] to include a staggered magnetic field term $-\frac{h}{2g}\int_{\mathbf{r},\tau}\sigma(\mathbf{r},\tau)$ in the action. Since the scaling of the magnetic field should not depend on the field direction, and since the staggered magnetic field couples linearly to the Néel order parameter field, the scaling dimension of the applied field is equal to that of the order-parameter field itself,

$$\frac{d}{d\ell}\left(\frac{h}{2g}\right) = \Delta_\pi\frac{h}{2g}. \tag{4.25}$$

On the other hand, we can use the constraint to expand $\sigma(\mathbf{r},\tau)$ in terms of the $\vec{\pi}$ fields and explicitly compute the one-loop renormalization of the applied field,

$$\frac{d}{d\ell}\left(\frac{h}{2g}\right) = (-3+2\Delta_\pi)\frac{h}{2g}+\frac{1}{(2\pi)^2}\frac{h}{1+\gamma}. \tag{4.26}$$

Equating Eqs. (4.25) and (4.26), we obtain

$$\Delta_\pi = 3-\frac{2}{(2\pi)^2}\frac{g}{1+\gamma}, \tag{4.27}$$

which results in the coupled RG equations

$$\frac{d\tilde{g}}{d\ell} = -\tilde{g} + \frac{1-\gamma/3}{1+\gamma}\tilde{g}^2, \tag{4.28}$$

$$\frac{d\gamma}{d\ell} = \gamma\left[1 - \frac{1+\gamma/3}{1+\gamma}\tilde{g}\right], \tag{4.29}$$

for $\tilde{g} = \frac{2}{(2\pi)^2}g$ and the Landau damping γ.

For $\gamma = 0$ we recover the RG equation of the conventional NLσM in 2+1 space-time dimensions. This RG equation exhibits two fixed points: the attractive, Néel ordered fixed point at $\tilde{g} = 0$ and the critical fixed point at $\tilde{g} = \tilde{g}_c = 1$. For $\tilde{g}(0) < 1$ the RG flow is towards $\tilde{g} = 0$, corresponding to a freezing of transverse spin-fluctuations on larger and larger scales. On the other hand, for $\tilde{g}(0) > 1$, $\tilde{g}(\ell) \to \infty$, corresponding to a vanishing of the spin stiffness and indicative of the destruction of long-range order by spatial and temporal fluctuations.

The coupled RG equations (4.28) and (4.29) do not exhibit any additional fixed points at finite γ. The RG flow in the $\tilde{g}$-γ plane is shown in Fig. 4.5. In the anti-ferromagnetically ordered phase, $\gamma(\ell)$ increases, indicative of damped spin-wave excitations. At the critical fixed point of the Néel transition the Landau damping γ is weakly irrelevant. The separatrix between the Néel antiferromagnet and the quantum disordered phase is given by $\tilde{g} \approx 1 + \frac{4}{3}\gamma - \frac{4}{9}\gamma^2$. Along the separatrix and for an initial value $\gamma_0 = \gamma(0) \ll 1$, the Landau damping vanishes as $\gamma(\ell) = \gamma_0/(1 + \frac{2}{3}\gamma_0\ell)$.

4.3.3 Including the Yukawa coupling to Dirac fermions

We now include the Yukawa coupling S_Y between the order parameter field to N_f copies of two-component Dirac fermion fields, as given in Eq. (6.3). The momentum-shell contribution of the diagram Fig. 4.4(a) will give rise to an additional correction to the NLσM,

$$\delta S_N = -\frac{1}{2}\frac{\lambda^2}{N_f}\int_q^< \vec{N}(q)\cdot\vec{N}(-q) \times \int_k^> \mathrm{Tr}\left\{\tau_z G_\psi(k)\tau_z G_\psi(k+q)\right\}, \tag{4.30}$$

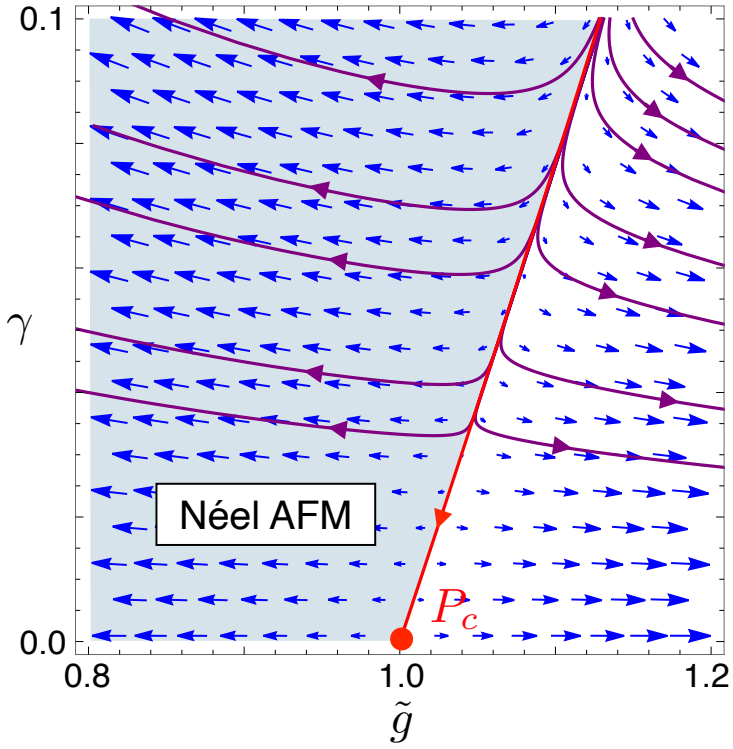

Figure 4.5: RG flow of the Landau damped NLσM as a function of the rescaled inverse spin stiffness $\tilde{g} = g/g_c$ and Landau damping γ. The red line separates the Néel AFM from the paramagnet. Along this separatrix, γ renormalizes to zero, demonstrating that the Néel quantum critical point P_c is stable against Landau damping. The increase of γ in the ordered phase indicates that spin-wave excitations are damped.

where $\int_q^<$ and $\int_k^>$ denote frequency-momentum integrals over $|q| \leq e^{-d\ell}$ and $e^{-d\ell} \leq |k| \leq 1$, respectively. The fermionic Green function in each of the N_f copies is given by

$$G_\psi(k) = \frac{ik_0 + k_x\tau_x + k_y\tau_y}{k_0^2 + \mathbf{k}^2}. \tag{4.31}$$

Note that the trace in Eq. (4.30) results in an additional factor of N_f. Expanding external momenta/frequencies $q = (\mathbf{q}, q_0)$ to quadratic order, we obtain

$$\delta S_N = -\frac{1}{3}\lambda^2 \frac{2}{(2\pi)^2} d\ell \int_q^< q^2 \vec{N}(q)\cdot\vec{N}(-q), \tag{4.32}$$

resulting in an additional contribution $d\left(\frac{1}{2g}\right) = -\frac{1}{3}\lambda^2\frac{2}{(2\pi)^2}d\ell$ to the renormaliza-

tion of the coupling constant. This changes the RG equations for $\tilde{g}$ and γ to

$$\frac{d\tilde{g}}{d\ell} = -\tilde{g} + \left[\frac{1-\gamma/3}{1+\gamma} + \frac{2}{3}\lambda^2\right]\tilde{g}^2, \tag{4.33}$$

$$\frac{d\gamma}{d\ell} = \gamma\left[1 - \frac{1+\gamma/3}{1+\gamma}\tilde{g} + \frac{1}{3}\lambda^2\tilde{g}\right]. \tag{4.34}$$

In order to determine the renormalization of the Yukawa coupling constant λ, we first need to determine the scaling dimension Δ_ψ of the fermion fields. The diagram in Fig. 4.4(e) results in a correction

$$\begin{aligned}\delta S_f &= -\frac{2\lambda^2 g}{N_f}\int_k^< \overline{\psi}(k)\left(\int_q^> D(q)\tau_z G_\psi(k+q)\tau_z\right)\psi(k) \\ &= \frac{2}{3N_f}\frac{1}{1+\gamma}\lambda^2\tilde{g}\,d\ell\int_k^< \overline{\psi}(k)G_\psi^{-1}(k)\psi(k),\end{aligned} \tag{4.35}$$

where the factor of two arises from the number of components of the transverse spin-fluctuation field $\vec{\pi}$, $N_\pi = 2$.

After rescaling frequency and momenta as before and fermion fields as $\psi(k) \to \psi(k)e^{-\Delta_\psi d\ell}$, we demand that that the prefactor of S_f remains scale-invariant, which results in

$$\Delta_\psi = 2 - \frac{1}{3N_f}\frac{1}{1+\gamma}\lambda^2\tilde{g}. \tag{4.36}$$

The diagram that contributes to the renormalization of the Yukawa vertex is shown in Fig. 4.4(f) and equals

$$\delta S_Y = \frac{g\lambda^3}{\sqrt{N_f}^3}\sum_i\int_{k_1,k_2}^< \pi_i(k_1-k_2)\overline{\psi}(k_1)\Omega_i\psi(k_2), \tag{4.37}$$

with coupling matrices

$$\begin{aligned}\Omega_i &= \sum_j\int_q^> D(q)(\sigma_j\otimes\tau_z)G_\psi(q)(\sigma_i\otimes\tau_z) \\ &\quad\times G_\psi(q)(\sigma_j\otimes\tau_z).\end{aligned} \tag{4.38}$$

Since G_ψ is independent of spin, we can evaluate the products of spin Pauli matrices and carry out the sum over j, $\sum_j \sigma_j\sigma_i\sigma_j = (2-N_\pi)\sigma_i$. The momentum-

shell integral is trivial and we indeed find that Ω_i is proportional to the original Yukawa coupling matrix $\sigma_i \otimes \tau_z$,

$$\Omega_i = \frac{2}{(2\pi)^2}(N_\pi - 2)\frac{1}{1+\gamma} d\ell (\sigma_i \otimes \tau_z). \tag{4.39}$$

However, the result crucially depends upon the number N_π of order-parameter components, as discussed in the literature [159, 55]. While the results for $N_\pi = 1$ and $N_\pi = 3$ are equal but of opposite sign, the diagram vanishes in the relevant case of $N_\pi = 2$ components, $\delta S_Y = 0$.

The rescaling of momenta, frequencies and fields gives rise to the RG equation

$$\begin{aligned} \frac{d\lambda}{d\ell} &= (-6 + \Delta_\pi + 2\Delta_\psi)\lambda \\ &= \lambda \left[1 - \frac{\tilde{g}}{1+\gamma} - \frac{2}{3N_f}\frac{\lambda^2 \tilde{g}}{1+\gamma} \right] \end{aligned} \tag{4.40}$$

for the Yukawa coupling λ.

4.3.4 RG Analysis

We will now discuss the coupled RG equations for the inverse spin stiffness $\tilde{g}$ (4.33), the Landau damping γ of the Néel order parameter (4.34) and the Yukawa coupling λ to the Dirac fermions (4.40). In Sec. 4.3.2 we found that in the absence of Yukawa coupling ($\lambda = 0$), the Landau damping γ is weakly irrelevant at the Néel quantum critical point P_c.

Let us first investigate the stability of P_c against Yukawa coupling in the absence of Landau damping ($\gamma = 0$). In this case the RG equations reduce to $d\tilde{g}/d\ell = -\tilde{g} + \left(1 + \frac{2}{3}\lambda^2\right)\tilde{g}^2$ and $d\lambda/d\ell = \lambda\left(1 - \tilde{g} - \frac{2}{3N_f}\lambda^2\tilde{g}\right)$. In this case we find a separatrix $\tilde{g} = 1 - \frac{2}{3}\lambda^2$, along which the flow of the Yukawa coupling increases according to $d\lambda/d\ell = \frac{2}{3}(1 - 1/N_f)\lambda^3$, resulting in $\lambda(\ell) = \lambda_0/\sqrt{1 - \frac{4}{3}\lambda_0^2(1 - 1/N_f)\ell}$. The Néel quantum critical point is therefore very weakly unstable against the Yukawa coupling to Dirac fermions. The RG flow in the $\tilde{g}$-λ plane is shown in Fig. 4.6.

To determine the critical surface in the three-dimensional parameter space of

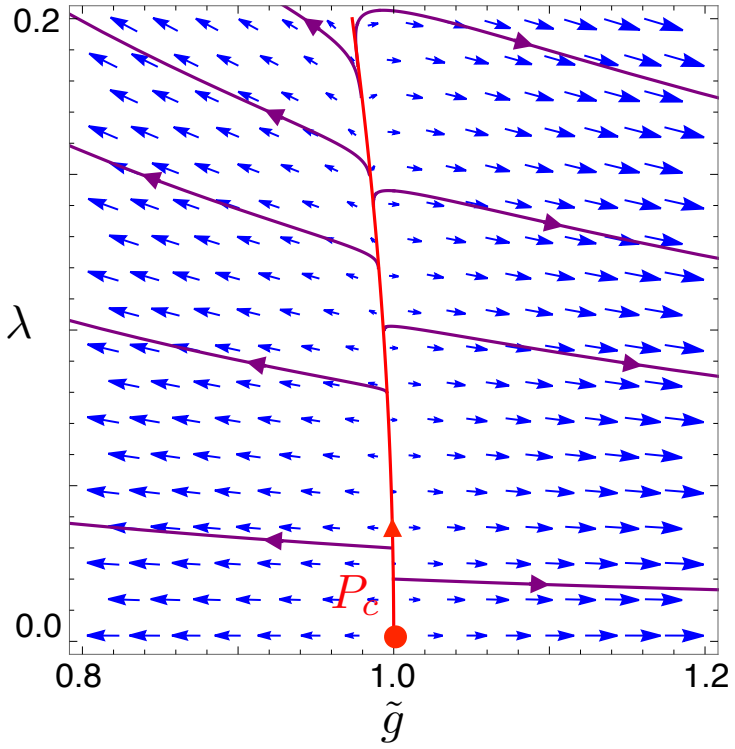

Figure 4.6: RG flow as a function of inverse spin stiffness $\tilde{g} = g/g_c$ and Yukawa coupling λ to Dirac fermions with $N_f = 4$ flavors. At the Néel quantum critical point P_c, the Yukawa coupling is a weakly relevant perturbation, indicated by the increase of λ along the separatrix shown in red.

$\tilde{g}$, γ and λ, we insert a polynomial ansatz $\tilde{g} = f(\gamma, \lambda)$ into the RG equations (4.33), (4.34) and (4.40). To second order we obtain

$$\tilde{g} = 1 + \frac{4}{3}\gamma - \frac{4}{9}\gamma^2 - \frac{2}{3}\lambda^2. \tag{4.41}$$

The critical surface is shown in Fig. 4.7. As expected, the critical surface contains the separatrices in the $\lambda = 0$ and $\gamma = 0$ planes. For initial values of the coupling constants slightly outside the surface, the RG flow is away from the surface: the inverse spin stiffness $\tilde{g}$ renormalizes to zero on one side, indicative of a freezing of spin-wave fluctuations, and to infinity on the other side, corresponding to a quantum disordered state. The Landau damping γ has a stabilizing effect on the Néel order, while the Yukawa coupling λ has a destabilizing effect.

To analyze the competition between γ and λ within the critical surface we

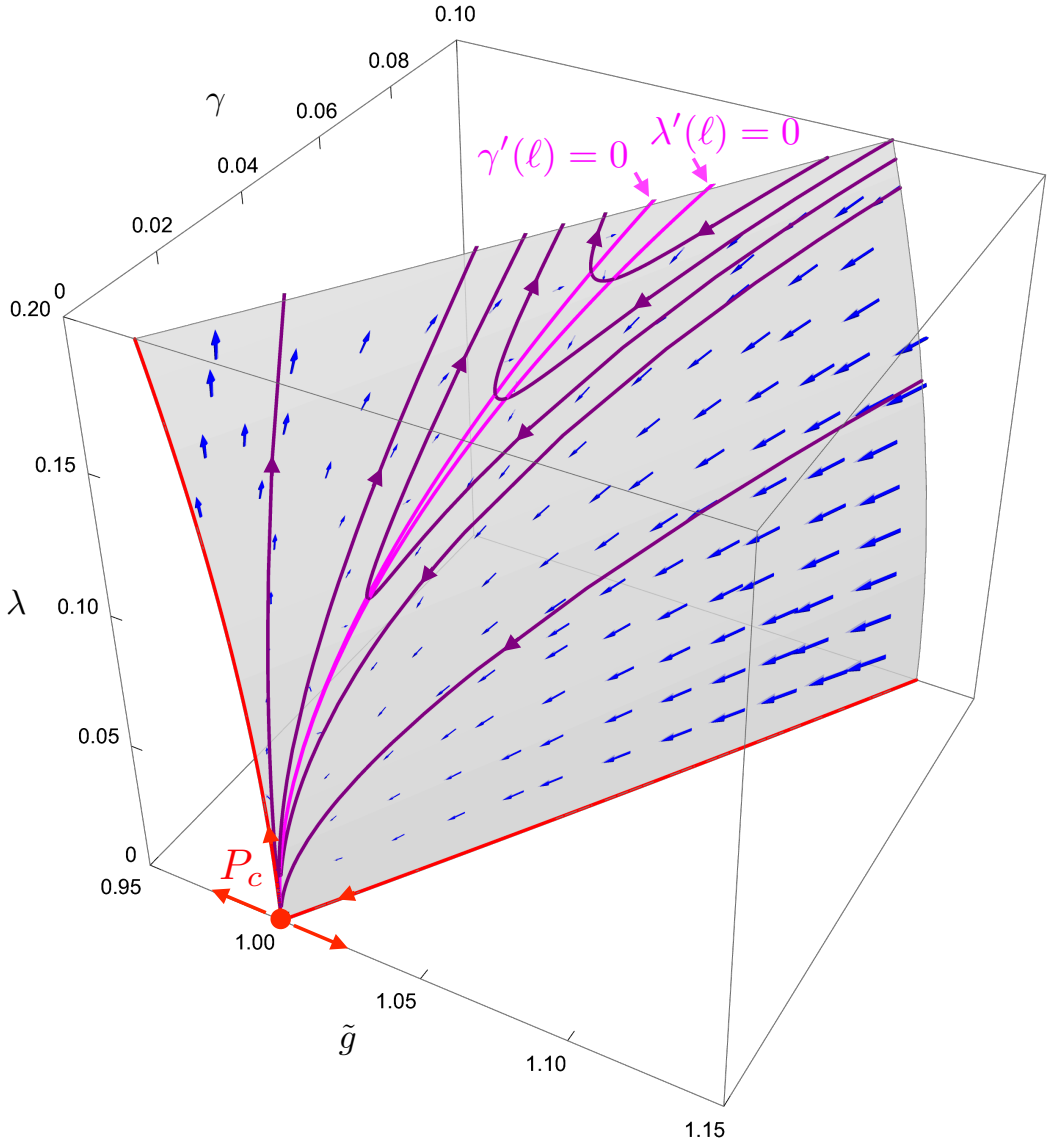

Figure 4.7: RG flow within the critical surface for $N_f = 4$, relevant to Dirac electrons on the honeycomb lattice. The Néel quantum critical point P_c is stable against Landau damping γ but unstable against Yukawa coupling λ. For sufficiently strong Landau damping, the RG flow is towards P_c until the trajectories turn to hit the magenta lines, which are given by $\gamma'(\ell) = 0$ and $\lambda'(\ell) = 0$, respectively, and closely track each other. At this point the RG flow becomes extremely slow and the parameters acquire small metastable values.

replace $\tilde{g}$ in the corresponding RG equations, using Eq. (4.41),

$$\frac{d\gamma}{d\ell} = -\frac{2}{3}\gamma^2 + \frac{2}{3}\gamma^3 + \gamma\lambda^2 \tag{4.42}$$

$$\frac{d\lambda}{d\ell} = -\frac{1}{3}\gamma\lambda + \frac{7}{9}\gamma^2\lambda + \frac{2}{3}(1-1/N_f)\lambda^3, \tag{4.43}$$

where we have expanded up to cubic order in the coupling constants. For $N_f \geq 4$, the RG equations only exhibit a single fixed point at $\lambda = 0$ and $\gamma = 0$, corresponding to the Néel quantum critical point P_c. The RG flow in the critical surface and several trajectories obtained from numerical integration of the RG equations (4.42) and (4.43) are shown in Fig. 4.7 for the case $N_f = 4$.

The RG flow is best understood in terms of the lines along which (i) $\gamma'(\ell) = 0$ and (ii) $\lambda'(\ell) = 0$, shown in magenta in Fig. 4.7, and given by (i) $\lambda^2 = \frac{2}{3}(\gamma - \gamma^2)$ and (ii) $\lambda^2 = \frac{1}{2(1-1/N_f)}(\gamma - \frac{7}{3}\gamma^2)$, respectively. These lines merge at P_c and because of they exhibit the same asymptotic functional form, $\lambda \sim \sqrt{\gamma}$, they closely track each other. As a result, the RG flow becomes very slow in the vicinity of this pair of lines and it is not possible for trajectories to cross them on scales relevant to any realistic system size.

The case $N_f = 4$, relevant to Dirac electrons on the honeycomb lattice, is the most extreme since in this case the coefficients of the leading $\sqrt{\gamma}$ terms are identical. For weak Landau damping, $\lambda^2 > \frac{2}{3}\gamma$, corresponding to points above the magenta lines, the flow is towards the regime of strong Yukawa coupling. This indicates that the Néel quantum critical P_c point becomes unstable toward Kondo physics, which falls outside the validity of our analysis.

On the other hand, if the Landau damping is sufficiently strong, $\lambda^2 < \frac{2}{3}\gamma$, both $\lambda(\ell)$ and $\gamma(\ell)$ decrease under the RG. The corresponding trajectories approach P_c until they eventually turn to hit the magenta lines. Here the RG flow practically comes to a standstill and $\lambda(\ell)$ and $\gamma(\ell)$ reach metastable plateaux values γ_* and $\lambda_*^2 \approx \frac{2}{3}\gamma_*$. The non-zero Yukawa coupling leads to the opening of a small electronic gap $\Delta \sim \lambda_* |\langle \vec{N}(\mathbf{r}, \tau) \rangle|$ in the Néel ordered phase where the spin-rotational symmetry is broken. On the critical surface the finite values γ_* and λ_* result in an anomalous contribution to the scaling dimension Δ_ψ of the fermion fields, giving rise to non-Fermi liquid behavior. However, the corresponding critical exponents are non-universal since the behavior is not associated with a true fixed point.

For $N_f < 4$ the RG equations (4.42) and (4.43) exhibit an additional fixed point

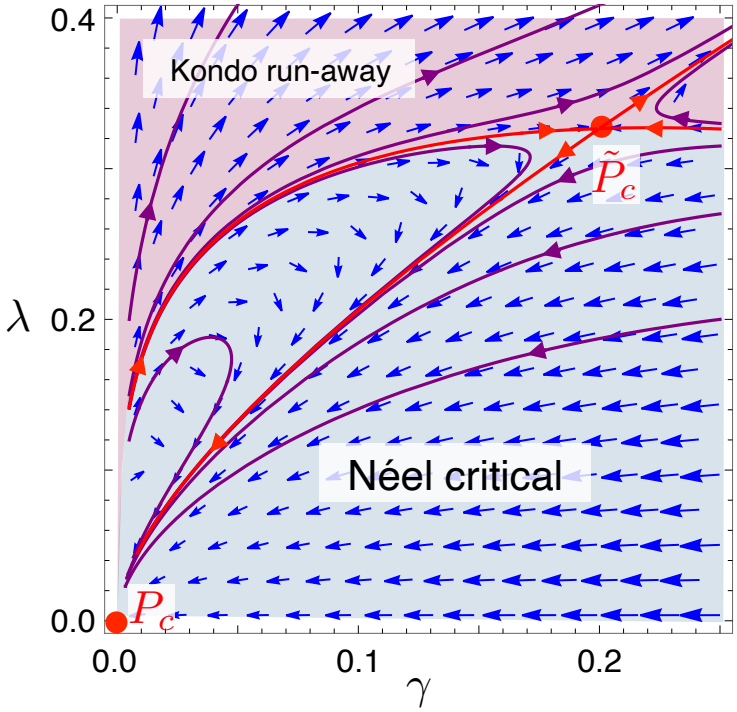

Figure 4.8: RG flow of the Landau damping γ and the Yukawa coupling λ within the critical surface for $N_f = 2$. The Néel quantum critical point P_c is thermodynamically stable in the blue region. In the purple region the flow is towards increasing λ, indicative of strong coupling Kondo physics. The transition between the two regimes is controlled by a new multi-critical point $\tilde{P}_c$.

$\tilde{P}_c$ at

$$\tilde{\gamma}_c = \frac{4-N_f}{4+3N_f}, \quad \tilde{\lambda}_c^2 = \frac{8}{3}\frac{N_f(4-N_f)}{(4+3N_f)^2}, \tag{4.44}$$

which merges with the Néel quantum critical point P_c as $N_f \to 4$, showing again that the case $N_f = 4$ is marginal.

In Fig. 4.8 the RG flow of γ and λ within the critical surface is shown for the representative case $N_f = 2$. In the blue region the RG flow is towards P_c, demonstrating that the Néel fixed point is thermodynamically stable rather than metastable. In the regime of small Yukawa coupling λ, this stability is achieved by finite but very small Landau damping γ. In the purple region the RG flow is towards large values of γ and λ, beyond the validity of our RG equations. The transition between this Kondo run-away regime and the Néel critical region is described by the multi-critical fixed point $\tilde{P}_c$.

We proceed to analyze the universal critical behavior of the multi-critical point

$\tilde{P}_c$ for general $N_f < 4$. The correlation length exponent $\tilde{\nu}$ can be obtained from linearizing the RG equation for the inverse spin stiffness (4.33) around the critical value $\tilde{g}_c \approx 1 + \frac{4}{3}\tilde{\gamma}_c - \frac{2}{3}\tilde{\lambda}_c^2$. The resulting RG equation is of the general form $d(\tilde{g} - \tilde{g}_c)/d\ell = \tilde{\nu}^{-1}(\tilde{g} - \tilde{g}_c)$. A short calculation gives $\tilde{\nu} = 1$ which is identical to the correlation-length exponent $\nu = 1$ at the Néel quantum critical point P_c.

From the scaling dimension Δ_π (4.27) of the transverse spin fluctuations fields $\vec{\pi}$ we obtain the anomalous dimension $\eta_\pi = 1$ at the Néel critical point P_c and

$$\tilde{\eta}_\pi = \frac{\tilde{g}_c}{1+\tilde{\gamma}_c} \approx 1 + \frac{1}{9}\frac{(4-N_f)(12-7N_f)}{(4+3N_f)^2} \tag{4.45}$$

at the new multi-critical point $\tilde{P}_c$. The additional contribution to $\tilde{\eta}_\pi$ results in a slightly different exponent of the algebraic order parameter correlations at criticality, $\langle \vec{\pi}(\mathbf{r})\vec{\pi}(\mathbf{0})\rangle \sim r^{-D+2-\tilde{\eta}_\pi}$, and corrections to other critical exponents, which can be obtained from the conventional scaling and hyper-scaling relations.

Due to the finite value $\tilde{\lambda}_c$ (4.44) of the Yukawa coupling at $\tilde{P}_c$, the symmetry-breaking transition will be accompanied with the opening of a gap [143]

$$\Delta \sim (\tilde{g}_c - \tilde{g})^{z\tilde{\nu}} = (\tilde{g}_c - \tilde{g}) \tag{4.46}$$

in the Dirac fermion spectrum for $\tilde{g} < \tilde{g}_c$, in the Néel ordered phase. Moreover, at $\tilde{P}_c$ the fermions acquire a small anomalous dimension [see Eq. (4.36)],

$$\tilde{\eta}_\psi = \frac{1}{3N_f}\frac{\tilde{\lambda}_c^2 \tilde{g}_c}{1+\tilde{\gamma}_c} \approx \frac{8}{9}\frac{4-N_f}{(4+3N_f)^2}, \tag{4.47}$$

which implies that the fermion Green's function has branch cuts rather than quasiparticle poles. The multicritical point $\tilde{P}_c$ is therefore associated with non-Fermi liquid behavior. From a scaling analysis of the fermionic spectral function [143] we find that the quasiparticle pole strength vanishes as

$$Z \sim (\tilde{g} - \tilde{g}_c)^{(z-1+\tilde{\eta}_\psi)\tilde{\nu}} = (\tilde{g} - \tilde{g}_c)^{\tilde{\eta}_\psi} \tag{4.48}$$

as the critical point is approached from the semi-metallic, non-magnetic phase ($\tilde{g} >$

$\tilde{g}_c$).

4.3.5 Comparison with the ε-expansion

We now address the question whether the same qualitative behavior can be found within an ε-expansion above the lower critical dimension, $D = 2+\varepsilon$. Although such an expansion gives analytic control of the criticality of the NLσM [158, 160], the Padé-Borel extrapolation to $\varepsilon = 1$ may be problematic due to a lack of sign oscillations in the coefficients of the ε-expansion of $1/\nu$ [161].

An additional problem arrises when the NLσM is coupled to Dirac fermions since the form of the resulting Landau damping of the Néel order parameter field explicitly depends on the dimension D, $\Pi(\mathbf{k}) = \gamma|\mathbf{k}|^{D-2}$. At one-loop order the RG equations for the inverse spin stiffness $\tilde{g} = g/(2\pi)$ and the Landau damping γ in $D = 2+\varepsilon$ are given by

$$\frac{d\tilde{g}}{d\ell} = -\varepsilon\tilde{g} + \frac{1-\gamma\varepsilon^2/4}{1+\gamma}\tilde{g}^2, \tag{4.49}$$

$$\frac{d\gamma}{d\ell} = \gamma\left[2-\varepsilon-\frac{1+\gamma\varepsilon^2/4}{1+\gamma}\tilde{g}\right], \tag{4.50}$$

where we have determined the scaling dimension of the order parameter field $\Delta_\pi = 2+\varepsilon-\tilde{g}/(1+\gamma)$ from the renormalization of an auxiliary magnetic field, as before.

Without Landau damping, $\gamma = 0$, we obtain the Néel quantum critical point at $\tilde{g}_c = \varepsilon$. At the critical spin stiffness the linearized RG equation for γ is equal to $d\gamma/d\ell = 2(1-\varepsilon)\gamma$, showing that near the lower critical dimension the Landau damping is a relevant perturbation.

Interestingly, the shell contribution of diagram in Fig. 4.4(a) is equal to zero in $D = 2$ due to a vanishing angular integral. As a result, the Yukawa coupling λ does not contribute to the renormalization of $\tilde{g}$ and γ, unlike in $D = 3$.

For similar reasons, the angular integration over the $D = 2$ dimensional shell causes the fermionic self-energy diagram, shown in Fig. 4.4(e), to vanish. The fermion field does therefore not acquire an anomalous dimension and the scaling dimension is trivial, $\Delta_\psi = (3+\varepsilon)/2$. From the scaling dimensions Δ_π and Δ_ψ we

obtain the renormaization of the Yukawa coupling,

$$\frac{d\lambda}{d\ell} = \lambda \left[1 - \frac{\tilde{g}}{1+\gamma} \right]. \tag{4.51}$$

At $\tilde{g}_c = \varepsilon$ and $\gamma = 0$ the RG equation reduces to $d\lambda/d\ell = (1-\varepsilon)\lambda$, demonstrating that the Yukawa coupling is a relevant perturbation at the Néel quantum critical point for $\varepsilon < 1$. Note that for $\varepsilon = 1$ both the the Landau damping γ and the Yukawa coupling λ become marginal, consistent with our calculation in $D = 3$.

4.4 Discussion

We have investigated the stability of the Néel quantum critical point of a two-dimensional quantum antiferromagnet with a Kondo coupling to N_f flavors of two-component Dirac fermion fields. For $N_f = 4$ this would describe Dirac electrons on the honeycomb lattice with two-fold spin and valley degeneracies.

The resulting long-wavelength field theory is given by a NLσM with a Yukawa coupling to the Dirac fermion fields. It is crucial to account for the Landau damping of the Néel order parameter field. From simple scaling arguments, the resulting self-energy correction to the order-parameter propagator is expected to dominate the IR physics.

At first glance the field theory seems very similar to the Heisenberg GNY theory, which describes the criticality in a purely itinerant model with strong local repulsions between the Dirac electrons. There are crucial differences, however. While in the GNY theory the quantum phase transition is tuned by the mass of the order parameter field, the NLσM only contains gradient terms and the criticality occurs as a function of the inverse spin-stiffness. It is therefore essential to follow the scale dependence of the order parameter propagator with both the quadratic gradient terms and the non-analytic self energy correction arising from Landau damping. In GNY theories on the other hand, the quadratic gradient terms can be discarded.

Another important difference is that the scaling dimension of the transverse spin-fluctuation field of the NLσM is fixed by the requirement that the constraint $\vec{N}^2 = 1$ is satisfied on all length scales. As a result, the boson scaling dimension

cannot be used to enforce scale invariance of the Yukawa coupling, in contrast to the large- N_f GNY theory.

We have employed momentum-shell RG to analyze the scale dependence of the inverse spin stiffness g, the Landau damping γ and the Yukawa coupling λ. Although γ and λ are initially linked to each other via the fermionic polarization diagram, the two parameters flow independently under the RG. At the Néel quantum critical point the scaling dimensions of both γ and λ vanish and a bifurcation analysis is required. We have investigated the coupled RG flow of the two perturbations within the critical surface $g = f(\gamma, \lambda)$ which contains the unperturbed Néel quantum critical point and separates the regions where transverse spin fluctuations freeze or diverge, respectively.

The flow within the critical surface shows that while the Landau damping γ is weakly irrelevant at the Néel critical point, the Yukawa coupling λ is a weakly relevant perturbation. Interestingly, the interplay between the two parameters crucially depends on the number N_f of Dirac fermion flavors. For $N_f \geq 4$, sufficiently strong Landau damping renders the Néel quantum critical point metastable. This is evident from an RG flow towards the Néel critical point up to scales larger than those relevant to experiments. This behavior is most pronounced for the marginal case $N_f = 4$, representing Dirac electrons on the honeycomb lattice,

For $N_f < 4$ the Néel critical point becomes thermodynamically stable over a region where the Landau damping dominates over the Yukawa coupling. We have established a new multicritical point on the critical surface which controls the transition between the Néel-critical and Kondo-runaway regimes. The finite values of γ and λ result in distinct critical exponents and an anomalous dimension of the fermion fields, correponding to non-Fermi-liquid behavior.

Chapter 5

Emergent Dirac Fermions in Kitaev Quantum Spin Liquids I: Majorana Mean-Field Theories

We have shown that even though the Dirac fermions have the simplest point-like Fermi surface, their zero-energy particle-hole fluctuations can significantly alter and complicate a quantum criticality. Another fold of complexity can be introduced if the fermions are originated from fractionalisation. Fractionalisation happens when a quasiparticle breaks into a set of new quasiparticles, each carrying a fraction of the properties. Unlike the integer quasiparticles, the fractionalised quasiparticle excitations have no elementary correspondence in particle physics. Typical examples are the fractional quantum Hall effect, where the fermions fractionalise into anyons carrying a fraction of the electron charges, and the spin-charge separation in one dimension, where the electrons break up into spinons that carry only the spin degree of freedom and holons that only inherit the electron charges. Since the fractionalised excitations have different physical properties or even follow different statistics, the quantum criticality can be more exotic once involved.

In the following two chapters, we focus on the phase transitions of the Kitaev honeycomb model. The model is $S = 1/2$ exactly solvable with a Z_2 quantum spin liquid (QSL) ground state. In the ground state, the spins fractionalise into Majorana fermions and Z_2 gauge fields. We will first introduce the exact solvability of the

pure Kitaev model, and then add additional Ising interaction to it to move the system away from the exactly solvable point. Different fermionisation methods will then be used to study the phase transitions at a mean-field level. In doing so, we will get hints that a topological phase transition in such a model could be described by a Gross-Neveu-Yukawa type theory, though the Dirac fermions are spinless and chargeless Majorana fermions.

The original work in this chapter was published in *Majorana-fermion mean field theories of Kitaev quantum spin liquids*, S. G. Saheli, J. Lin, H. Hu, F. Krüger, Physical Review B 109 (1), 014407.[162].

5.1 Introduction

Quantum Spin Liquids (QSLs) [163, 164, 165] are a novel class of materials in which geometric and/or exchange frustration suppresses magnetic order down to absolute zero temperature. Because of the topological character of the ground-state wave function with a special type of long-range quantum entanglement, QSLs exhibit exotic fractional excitations [166], which are believed to hold great potential for quantum communication and computation [167]. These concepts were put on a firm footing in the seminal work by Alexei Kitaev [22] who constructed an exactly solvable QSL model on the honeycomb lattice and demonstrated that the spins break-up (fractionalize) into a set of Majorana fermions. The emergent fermions essentially behave as the electrons in graphene with a relativistic Dirac dispersion, although they do not carry electric charge and are coupled to gauge fields.

Although the bond-directional dependence of the Ising exchange anisotropy in the Kitaev model might seem artificial, it was later realized that, as a result of spin-orbital entanglement [168], the Kitaev couplings can play a dominant role in honeycomb Iridates and Ruthenates, such as Na_2IrO_3 [169, 170, 171, 172, 173], α-Li_2IrO_3 [171], β-Li_2IrO_3 [174], γ-Li_2IrO_3 [175] and α-$RuCl_3$ [176, 177, 178]. However, small additional magnetic interactions such as Heisenberg terms drive these systems into a magnetically ordered state that forms at low temperatures. Nevertheless, at higher temperatures or in applied magnetic field signatures of the

nearby Kitaev QSL state are seen [179].

While the theoretical interest in the novel fundamental physics of QSLs is considerable, the experimental identification of QSLs has proven difficult. While the emergent fermions have manifestations in specific heat and thermal transport properties [179, 180, 181], rather indirect evidence comes from the lack of magnetic ordering seen in NMR, μSR and neutron diffraction, as well as from the absence of sharp quasiparticle excitations in neutron scattering. Unlike in the case of Heisenberg spin-1/2 chain systems where the measured intensity variation is quantitatively understood from the continuum of fractionalized spinon excitations [182, 183], in the case of two-dimensional QSLs theoretical techniques are yet to be developed to quantitatively understand finite temperature excitation spectra.

A possible way to distinguish signatures of fractionalization from diffuse scattering originating from disorder or short ranged and lived quasiparticle excitations is through entanglement witnesses such as quantum Fisher information [184] which can be directly computed from the dynamic susceptibilities measured in inelastic neutron scattering experiments [185]. In the case of the idealized Kitaev model it was demonstrated theoretically [186, 187] that the magnetic structure factor shows signatures of fractionalized Majorana fermions and fluxes of Z_2 gauge fields that are in qualitative agreement with the finite-temperature excitation spectrum of α-$RuCl_3$ [177, 178]. More recently, the theoretical approach was extended beyond the integrable point of the pure Kitaev model, using an augmented parton mean-field theory based on the Kitaev Majorana representation [188]. Finally, by combining the density-matrix renormalization (DMRG) ground state method and a matrix-product state (MPS) based dynamical algorithm [189] it was demonstrated that the spectra of the Kitaev-Heisenberg model close to the QSL phase show proximate spin-liquid features.

Although the physics of the Kitaev model is naturally captured in terms of Majorana fermions, phase diagrams of the Kitaev-Heisenberg model and extensions thereof were calculated in terms of complex spin-1/2 fermionic spinons, either on the level of SU(2) slave fermion mean-field theory [190, 191] or numerically by

means of pseudo-fermion functional renormalization group [171, 192, 193].

In this chapter we compute zero and finite temperature mean-field phase diagrams in terms of fractionalized Majorana fermion degrees of freedom. There exist different type of representations of the spin-1/2 operators in terms of Majorana fermions which are equivalent for the description of the ground-state properties of the pure isotropic or anisotropic Kitaev model [194, 195], but not necessarily if finite-temperature excitations are considered or additional interactions are taken into account. We focus on two representations, the one originally introduced by Kitaev [22] and the two-dimensional Jordan-Wigner transformation (JWT) [196, 197, 194, 198].

In addition to Kitaev and Heisenberg exchange we will consider magnetic exchange anisotropy, which as a result of the directional dependence of the Kitaev coupling induces spatial anisotropy. For the pure Kitaev model anisotropy is known to result in a topological phase transition [22] from a QSL hosting gapless Majorana and gapped flux excitations to a gapped Z_2 one with Abelian excitations [189].

The outline of the chapter is as follows. In Sec. 5.2 we first give an brief introduction of the pure Kitaev model, and then motivate the Hamiltonian of the anisotropic $S = 1/2$ Kitaev-Heisenberg model on the honeycomb lattice. The two-dimensional JWT and consecutive mean-field decoupling scheme are introduced in Sec. 5.3, where the underlying string operator is defined such that the fermionized Hamiltonian remains local in the extreme Ising limit of the Heisenberg exchange interaction. In Sec. 5.4 we map the spin Hamiltonian to a set of four Majorana fermions, following the original construction by Kitaev, and enforce the Hilbert space constraint through a Lagrange multiplier. We discuss the mean-field decoupling of the interaction terms in bond and magnetization channels and determine the Lagrange multiplier as a function of the mean-field parameters.

Our results are presented in Sec. 5.5. We first demonstrate that the two mean-field theories result in identical phase boundaries for the topological transition between the gapless and gapped Kitaev QSLs. Interestingly, the anisotropy of the Kitaev coupling and the Ising exchange cooperate in driving the transition.We then

determine the antiferromagnetic instability driven by the Ising exchange. This transition is strongly first order and not correctly described by the JWT mean-field theory. We finally determine the finite-temperature phase diagram and show that the magnetic phase transition becomes continuous above a certain temperature. At this temperature scale, the specific heat above the Kitaev QSL shows a peak, indicating a crossover between a fractionalized paramagnet with frozen Z_2 flux excitations to a conventional paramagnetic state at higher temperatures. In Sec. 5.6 we summarize and discuss our results.

5.2 The Kitaev Model and Beyond

5.2.1 Kitaev Model

The Kitaev model is one of the rare models that are exactly solvable. It describes a spin-$1/2$ Hamiltonian on a honeycomb lattice with bond-oriental spin-spin interactions, as shown in fig. 5.1. The Hamiltonian can be simply written as:

$$\hat{H} = \sum_{\gamma=x,y,z} \sum_{\langle i,j \rangle_\gamma} K_\gamma \hat{\sigma}_i^\gamma \hat{\sigma}_j^\gamma. \tag{5.1}$$

On each bond, there's only an anisotropic interaction between the corresponding spin component of the nearest neighbour spins. Though it seems artificial at first glance, its exact solvability and exotic QSL ground state make it a popular model in the community.

In order to solve the model, one needs to first fermionise the spin Hamiltonian with Majorana fermions by defining the transformation: $\hat{\sigma}_i^\gamma = i\hat{\eta}_i^0\hat{\eta}_i^\gamma$, where η_i^0 and $\eta_i^\gamma, \gamma = (x,y,z)$ are different Majorana fermions on lattice site i. This transforms the spin Hamiltonian into an interacting theory of four Majorana fermions:

$$\begin{aligned}\hat{\mathscr{H}} = \sum_{\mathbf{r}} & \eta_A^0(\mathbf{r})\eta_B^0(\mathbf{r}+\mathbf{a}_1)\eta_A^x(\mathbf{r})\eta_B^x(\mathbf{r}+\mathbf{a}_1) \\ & + \eta_A^0(\mathbf{r})\eta_B^0(\mathbf{r}+\mathbf{a}_2)\eta_A^y(\mathbf{r})\eta_B^y(\mathbf{r}+\mathbf{a}_2) \\ & + \eta_A^0(\mathbf{r})\eta_B^0(\mathbf{r})\eta_A^z(\mathbf{r})\eta_B^z(\mathbf{r}),\end{aligned} \tag{5.2}$$

where A, B are the sublattice indices in a unit cell, and $\mathbf{a}_1, \mathbf{a}_2$ are the two lattice vectors of the honeycomb lattice. Note that a pair of Majorana fermions can be combined to form a complex fermion, suggesting that our new Hilbert space is actually twice as large as the original spin space. Therefore a constraint on $\eta_i^0 \eta_i^x \eta_i^y \eta_i^z$ is needed to project the states onto the 'physical' Hilbert space.

The Hamiltonian can be further reduced once realising that the bond operators u_i^γ, defined as the product of the bond-dependent Majorana fermion operators $u_i^\gamma(\mathbf{r}) = i\eta_A^\gamma(\mathbf{r})\eta_B^\gamma(\mathbf{r}+\vec{\delta}_\gamma), \vec{\delta}_\gamma = (\mathbf{a}_1, \mathbf{a}_2, 0)$, commute with the Hamiltonian, $\left[u_i^\gamma(\mathbf{r}), H\right] = 0$. This suggests that the bond operators can be diagonalised simultaneously with the Hamiltonian. Another observation is that $u_i^{\gamma 2} = 1$, leading to the simple eigenvalues ± 1. Due to its property, the bond operator u_i^γ is also called emergent Z_2 gauge field. However, as the name suggests, u_i^γ itself is only a gauge degree of freedom, not physically observable. On the other hand, the collective behaviour of the product of six connected bond operators on a hexagon, $B_p = u_1^x u_2^y u_3^z u_4^x u_5^y u_6^z$, dubbed the plaquette operator, is a physical observable which also commutes with the Hamiltonian, with eigenvalues ± 1. In analogy to the magnetic flux induced by a magnetic field, the eigenvalues of the plaquette operators can be viewed as Z_2 fluxes on the hexagons, with $B_p = 1$ corresponding to zero flux, and $B_p = -1$ as π flux.

It seems that if we know the flux configuration of the ground state, we can replace the bond operators with their eigenvalues in the Hamiltonian and get a single-particle theory. Fortunately, this is exactly the case. According to Lieb's theorem, the ground state on a honeycomb lattice is flux-free. That is to say, $B_p = 1$ for all plaquettes. One can therefore immediately choose the simplest gauge by setting all bond operators to have eigenvalues of 1. The left Hamiltonian,

$$H = \sum_{\mathbf{r}} \left(\eta_A^0(\mathbf{r})\eta_B^0(\mathbf{r}) + \eta_A^0(\mathbf{r})\eta_B^0(\mathbf{r}+\mathbf{a_1}) + \eta_A^0(\mathbf{r})\eta_B^0(\mathbf{r}+\mathbf{a_2}) \right), \tag{5.3}$$

should be very familiar to the readers - It resembles the electrons in graphene. Indeed, the energy dispersion of the Majorana fermions η_i^0 is identical to that of the electrons on a honeycomb lattice, with six Dirac cones sitting on the corners of the Brillouin zone, as shown in fig.5.1(b). The ground state is thus called a gapless Z_2

quantum spin liquid state. In analogy to Dirac fermions on a honeycomb lattice, anisotropy in the Kitaev coupling K_γ will cause a pair of Dirac points with different valley indices to move towards each other. At the critical value, the two Dirac points merge and form a semi-Dirac cone, after which a gap opens in the spectrum, corresponding to a gapped QSL state. Apart from anisotropy, Kitaev has also shown in [22] that a magnetic field along [111] direction can also open a gap in the dispersion, and the gapped state has a well-defined first Chern number.

Before we end the section and move away from the exact solvable point, some discussions on the underlying physics are due. Firstly, the emergence of Z_2 gauge fields suggests that QSLs are topologically non-trivial. In fact, the gapless Z_2 QSL state is sometimes called a symmetry-protected topological (SPT) state, as the gapless nature is protected by inversion and time-reversal symmetry, resembling Dirac semimetals. additionally, the gapped QSLs belong to the category of symmetry-enriched topological (SET) states. Readers are referred to [199] for a detailed categorisation and explanation. Secondly, The Kitaev model is a good example of fractionalisation, where a spin $1/2$ breaks into four spinless, chargeless Majorana fermions. Three of them correspond to the emergent Z_2 gauge fields, which are localised in the zero-flux ground state, while the left Majorana fermion remains mobile, in resemblance to the complex fermion in graphene. Though fractionalisation is only a mathematical choice of rewriting the spin operators, we see that with the appropriate representation, the fractionalised quasiparticles have distinct dynamics, and therefore can be treated as independent degrees of freedom. Such fractionalisation can also be reflected through physical observations. For example, due to the different dynamics of the fractional degrees of freedom, there will be two different typical energy/temperature scales. A fraction of the total entropy will be released at each energy/temperature scale, resulting in a two-step thermalisation as proposed in [200, 201, 202]. However, for observables like the spin-spin correlation, the translation to the fractionalised quasiparticle language is not so straightforward. At last, though being a model with anisotropic bond-oriental interactions as 'unnatural' or 'toy' as one could imagine, the Kitaev model turns out to be realistic. As

uncovered in the neat work by Kalliulin [168], the Kitaev coupling is dominant in a family of transition metal oxides with strong spin-orbit coupling. Nowadays, many of them have suggested that they are in, or very close, to a Kitaev QSL ground state, although decisive proof remains elusive.

5.2.2 Kitaev-Ising model

Our starting model is the anisotropic $S = 1/2$ Kitaev-Heisenberg model on the honeycomb lattice in the limit of an extreme Ising anisotropy in the Heisenberg sector. The Hamiltonian of the model is given by

$$\hat{H} = \sum_{\gamma=x,y,z} \sum_{\langle i,j\rangle_\gamma} K_\gamma \hat{\sigma}_i^\gamma \hat{\sigma}_j^\gamma + J \sum_{\langle i,j\rangle} \hat{\sigma}_i^z \hat{\sigma}_j^z, \tag{5.4}$$

where $\hat{\sigma}^\gamma$ are the spin-1/2 operators in units of $\hbar/2$, $\hat{S}^\gamma = \frac{\hbar}{2}\hat{\sigma}^\gamma$, satisfying the spin commutator relations $[\hat{\sigma}_i^\alpha, \hat{\sigma}_j^\beta] = 2\delta_{ij}\varepsilon_{\alpha\beta\gamma}\hat{\sigma}_i^\gamma$.

The Kitaev couplings K_γ are illustrated in Fig. 5.1(a). Along each of the three inequivalent nearest neighbor bonds, labelled by $\gamma = x, y, z$, different spin components are coupled, e.g. along the x-bonds the Kitaev coupling is $K_x \hat{\sigma}_i^x \hat{\sigma}_j^x$. In this work we consider antiferromagnetic Kitaev couplings and allow the coupling between spin-z components to be stronger than those between the x and y components, $K_z \geq K_x = K_y = K > 0$. Because of the bond-directional nature of the Kitaev coupling, this spin-exchange anisotropy is linked to a strong spatial anisotropy.

By symmetry one should also expect spin-exchange anisotropy in the Heisenberg interactions. For reasons that we will explain later we focus on the case of very strong Ising anisotropy, $J = J_z > 0$ and $J_x = J_y = 0$.

The zero-temperature phase diagram of the model is controlled by the two dimensionless parameters

$$\alpha = \frac{J}{K} \quad \text{and} \quad \delta = \frac{K_z - K}{K}. \tag{5.5}$$

For $\alpha = 0$ the model reduces to an anisotropic Kitaev model which is exactly solvable in terms of Majorana fermions, either by using the original Kitaev con-

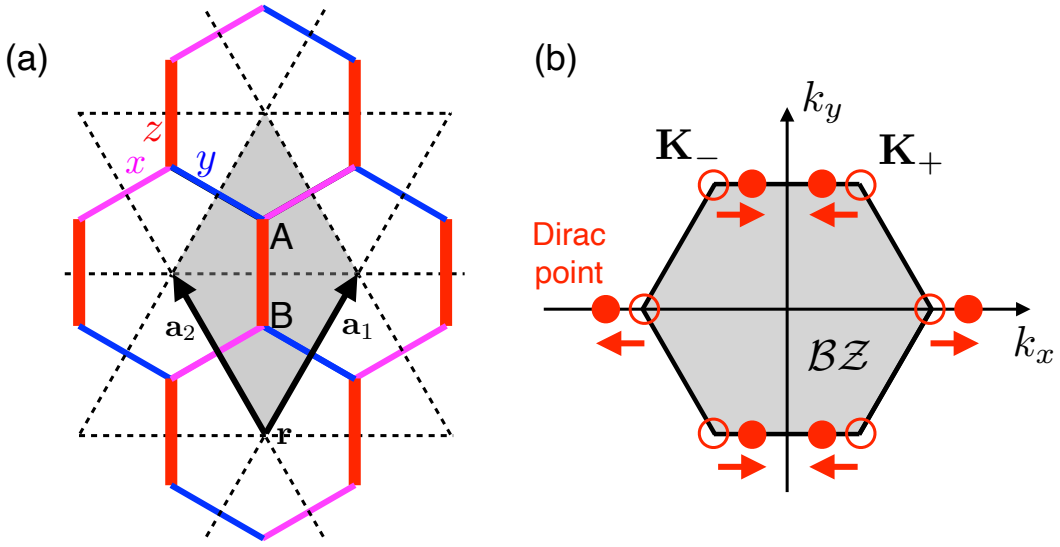

Figure 5.1: (a) Illustration of the Kitaev model on the honeycomb lattice. The three inequivalent nearest neighbor bonds are labelled by $\gamma = x, y, z$ and shown in different colors. Along a bond in the γ direction only the spin components S^γ between the neighboring sites are coupled. We allow the Kitaev couplings to be anisotropic and include an additions Ising exchange between spin-z components on all nearest neighbor bonds. The unit cell of the honeycomb lattice, shaded in grey, contains two lattice sites labelled by A and B. (b) The pure Kitaev model is exactly solvable in terms of Majorana fermions. In the isotropic limit one band is gapless with Dirac points at the corners $\mathbf{K}_+$ and $\mathbf{K}_-$ of the hexagonal Brillouin zone (BZ). With increasing anisotropy δ and Ising exchange α the Dirac points move along the edges of the BZ and eventually merge, corresponding to a topological phase transition to a gapped Kitaev QSL. Sufficiently strong α results in a first-order transition to an antiferromagnet with fully gapped Majorana fermion spectrum.

struction [22] or a two-dimensional Jordan-Wigner transformation [194]. In both cases one obtains flat bands, corresponding to local flux excitations, and a gapless dispersive band with Dirac points at the Fermi level. In the isotropic Kitaev model ($\delta = 0$) the Dirac points are located at the corners $\mathbf{K}_\pm = 2\pi(\pm 1/(3\sqrt{3}, 1/3)$ of the hexagonal Brillouin zone (BZ) [see Fig. 5.1(b)]. Anisotropy in the Kitaev couplings is known to drive a topological phase transition from a gapless to a gapped QSL [22]. With Increasing anisotropy δ, the Dirac points move along the edges of the BZ and merge when $\delta_c = 1$, corresponding to $K_z/K = 2$. At this point the dispersive Majorana band exhibits a semi-Dirac point at $2\pi(0, 1/3)$, which is a quadratic band touching point along the edge but relativistic in the transverse direction. For values $\delta > 1$ the excitations become gapped. This behavior is very similar to the topologi-

cal phase transition proposed to occur for electrons moving in strained honeycomb lattices [203, 204, 205, 55, 153] and observed experimentally in black phosphorus [206, 207].

We will see that $\alpha = J/K$ has a similar effect on the Dirac band and cooperates with the anisotropy in driving the topological phase transition. In addition, the flux excitations become weakly dispersive for $\alpha > 0$. As one might expect, sufficiently strong α leads to a first-order transition between a Kitaev QSL and an Ising antiferromagnet with a gapped Majorana fermion spectrum of strongly hybridized bands.

5.3 Majorana fermions from Jordan-Wigner transformation

The Jordan-Wigner transformation (JWT) is usually used to express one-dimensional $S = 1/2$ spin Hamiltonians in terms of spinless fermions with creation and annihilation operators $\hat{d}_n^\dagger$, $\hat{d}_n$, where n labels the site along the one-dimensional lattice. It is natural to identify the no-fermions state $|0\rangle$ with the eigenstate $|\uparrow\rangle$ of the $\hat{\sigma}^z$ spin operator and the singly occupied state $|1\rangle$ with $|\downarrow\rangle$. However, since spin operators on different sites commute while fermionic operators anti-commute, it is not possible to define a local transformation. Instead one needs to include a semi-infinite string operator

$$\hat{D}_n = \prod_{\ell<n}(1-2\hat{d}_\ell^\dagger \hat{d}_\ell). \tag{5.6}$$

to match the quantum statistics of spins and fermions and define the one-dimensional JWT as

$$\hat{\sigma}_n^z = 1-2\hat{d}_n^\dagger \hat{d}_n = (\hat{d}_n^\dagger + \hat{d}_n)(\hat{d}_n^\dagger - \hat{d}_n), \tag{5.7}$$

$$\hat{\sigma}_n^x = \hat{D}_n(\hat{d}_n^\dagger + \hat{d}_n), \tag{5.8}$$

$$\hat{\sigma}_n^y = i\hat{D}_n(\hat{d}_n^\dagger - \hat{d}_n). \tag{5.9}$$

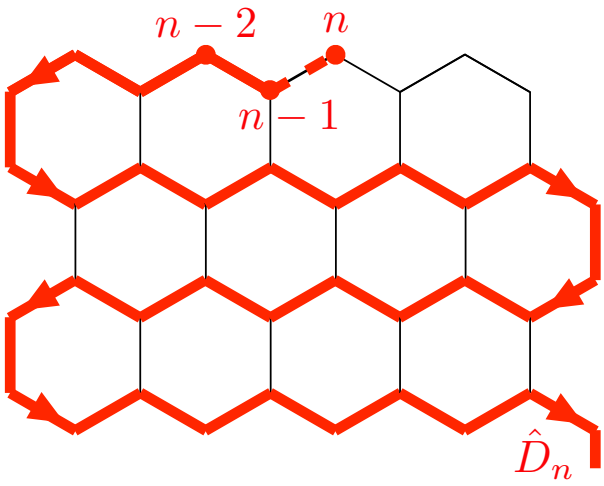

Figure 5.2: Illustration of the snake string operators used in the two-dimensional Jordan-Wigner transformation (JWT) of the Kitaev-Ising model.

It is easy to check that the string operator is hermitian, $\hat{D}_n^\dagger = \hat{D}_n$, and satisfies $\hat{D}_n^2 = 1$, $\hat{D}_n\hat{D}_{n+1} = 1 - 2\hat{d}_n^\dagger\hat{d}_n$ and $[\hat{d}_n^\dagger, \hat{D}_n] = [\hat{d}_n, \hat{D}_n] = 0$.

These properties of the string operator ensure that one-dimensional spin Hamiltonians with short-ranged spin interactions remain short ranged after JWT. The generalization of the JWT to two dimensions is problematic for several reasons. Firstly, the string operator connecting a given lattice site to infinity is not uniquely defined, and in principle gauge transformations corresponding to deformations of the string need to be taken into account [208]. Secondly, nearest neighbor sites in the two dimensional lattice are not necessarily nearest neighbors along the string. As a result, the fermionized Hamiltonian will contain non-local interactions involving segments of string operators.

The Kitaev model on the honeycomb lattice is an example where the second problem of non-locality can be circumvented by defining snake string operators [196, 197, 194] shown in Fig. 5.2. In this case, the x and y bonds, which involve the string operators, couple nearest neighbors along the string. Using that $\hat{D}_n\hat{D}_{n+1} = 1 - 2\hat{d}_n^\dagger\hat{d}_n$ we obtain

$$\hat{\sigma}_n^x\hat{\sigma}_{n+1}^x = (\hat{d}_n^\dagger - \hat{d}_n)(\hat{d}_{n+1}^\dagger + \hat{d}_{n+1}), \tag{5.10}$$

$$\hat{\sigma}_n^y\hat{\sigma}_{n+1}^y = (\hat{d}_{n+1}^\dagger - \hat{d}_{n+1})(\hat{d}_n^\dagger + \hat{d}_n). \tag{5.11}$$

Note that the z bonds connect spins that are not nearest neighbors along the snake string. As a result, any Hamiltonian that involves couplings between the x or y spin components along the z bonds, e.g. the Kitaev-Heisenberg model, would be non-local in terms of the Jordan-Wigner fermions. This however is not the case for the pure Kitaev model or for our model with additional Ising couplings $\hat{\sigma}_i^z\hat{\sigma}_j^z$ on all nearest-neighbor bonds.

The resulting Hamiltonian of the Kitaev-Ising model is given by

$$\begin{aligned}\hat{H}/K &= \sum_{\mathbf{r}}\sum_{i=1,2}(\hat{d}^\dagger_{A,\mathbf{r}}-\hat{d}_{A,\mathbf{r}})(\hat{d}^\dagger_{B,\mathbf{r}+\mathbf{a}_i}+\hat{d}_{B,\mathbf{r}+\mathbf{a}_i})\\ &\quad+\alpha\sum_{\mathbf{r}}\sum_{i=1,2}(\hat{d}^\dagger_{A,\mathbf{r}}+\hat{d}_{A,\mathbf{r}})(\hat{d}^\dagger_{A,\mathbf{r}}-\hat{d}_{A,\mathbf{r}})\\ &\quad\times(\hat{d}^\dagger_{B,\mathbf{r}+\mathbf{a}_i}+\hat{d}_{B,\mathbf{r}+\mathbf{a}_i})(\hat{d}^\dagger_{B,\mathbf{r}+\mathbf{a}_i}-\hat{d}_{B,\mathbf{r}+\mathbf{a}_i})\\ &\quad+(1+\delta+\alpha)\sum_{\mathbf{r}}(\hat{d}^\dagger_{A,\mathbf{r}}+\hat{d}_{A,\mathbf{r}})(\hat{d}^\dagger_{A,\mathbf{r}}-\hat{d}_{A,\mathbf{r}})\\ &\quad\times(\hat{d}^\dagger_{B,\mathbf{r}}+\hat{d}_{B,\mathbf{r}})(\hat{d}^\dagger_{B,\mathbf{r}}-\hat{d}_{B,\mathbf{r}}),\end{aligned}\tag{5.12}$$

where $(\alpha,\mathbf{r})$ denote the sites of the two-dimensional honeycomb lattice, with $\mathbf{r}$ the unit cell spanned by $\mathbf{a}_1$ and $\mathbf{a}_2$ and $\alpha=A,B$ the atom in the unit cell, as illustrated in Fig. 5.1(a). The dimensionless coupling constants α and δ are defined in Eq. (5.5). The interaction terms, which arise from the $\hat{\sigma}_i^z\hat{\sigma}_j^z$ terms in the spin Hamiltonian, are of strength J along the x and y bonds and of strength K_z+J along the z bonds.

The Hamiltonian is naturally expressed in terms of Majorana fermions,

$$\begin{aligned}\hat{c}_A(\mathbf{r}) &= i[\hat{d}^\dagger_A(\mathbf{r})-\hat{d}_A(\mathbf{r})],\\ \hat{\eta}^z_A(\mathbf{r}) &= \hat{d}^\dagger_A(\mathbf{r})+\hat{d}_A(\mathbf{r}),\end{aligned}\tag{5.13}$$

on sub-lattice A and

$$\begin{aligned}\hat{c}_B(\mathbf{r}) &= \hat{d}^\dagger_B(\mathbf{r})+\hat{d}_B(\mathbf{r}),\\ \hat{\eta}^z_B(\mathbf{r}) &= i[\hat{d}^\dagger_B(\mathbf{r})-\hat{d}_B(\mathbf{r})],\end{aligned}\tag{5.14}$$

on sub-lattice B. The meaning of the superscript z on the Majorana fermion η will

become clear when we compare with the mean-field theory based on the Kitaev representation of the spin operators in terms of Majorana fermions. The resulting Hamiltonian is given by

$$\begin{aligned}\hat{H}/K &= -i\sum_{\mathbf{r}}\sum_{i=1,2}\hat{c}_A(\mathbf{r})\hat{c}_B(\mathbf{r}+\mathbf{a}_i)\\ &\quad +\alpha\sum_{\mathbf{r}}\sum_{i=1,2}\hat{c}_A(\mathbf{r})\hat{\eta}^z_A(\mathbf{r})\hat{c}_B(\mathbf{r}+\mathbf{a}_i)\hat{\eta}^z_B(\mathbf{r}+\mathbf{a}_i)\\ &\quad +(1+\delta+\alpha)\sum_{\mathbf{r}}\hat{c}_A(\mathbf{r})\hat{\eta}^z_A(\mathbf{r})\hat{c}_B(\mathbf{r})\hat{\eta}^z_B(\mathbf{r}).\end{aligned} \tag{5.15}$$

The Majorana operators satisfy $\hat{c}^\dagger_\sigma(\mathbf{r}) = \hat{c}_\sigma(\mathbf{r})$. $(\hat{\eta}^z_\sigma(\mathbf{r}))^\dagger = \hat{\eta}^z_\sigma(\mathbf{r})$ and the anti-commutator relations $\{\hat{c}_\sigma(\mathbf{r}),\hat{c}_{\sigma'}(\mathbf{r}')\} = \{\hat{\eta}^z_\sigma(\mathbf{r}),\hat{\eta}^z_{\sigma'}(\mathbf{r}')\} = 2\delta_{\sigma,\sigma'}\delta_{\mathbf{r},\mathbf{r}'}$ and $\{\hat{c}_\sigma(\mathbf{r}),\hat{\eta}^z_{\sigma'}(\mathbf{r}')\} = 0$.

5.3.1 Mean-Field Theory

We perform a self-consistent mean-field decoupling of the interactions in both the bond and density channels. The former is required to recover the physics of the Kitaev model. We define the averages

$$a_{\mathbf{r},\mathbf{r}'} = -i\left\langle\hat{\eta}^z_A(\mathbf{r})\hat{\eta}^z_B(\mathbf{r}')\right\rangle \tag{5.16}$$

$$b_{\mathbf{r},\mathbf{r}'} = -i\left\langle\hat{c}_A(\mathbf{r})\hat{c}_B(\mathbf{r}')\right\rangle, \tag{5.17}$$

where $a_\perp = a_{\mathbf{r},\mathbf{r}+\mathbf{a}_i}$ and $b_\perp = b_{\mathbf{r},\mathbf{r}+\mathbf{a}_i}$ for the x and y bonds and $a_z = a_{\mathbf{r},\mathbf{r}}$ and $b_z = b_{\mathbf{r},\mathbf{r}}$ for the z bonds. The local staggered magnetization of the antiferromagnetic state is given by

$$m = i\left\langle\hat{c}_\sigma(\mathbf{r})\hat{\eta}^z_\sigma(\mathbf{r})\right\rangle. \tag{5.18}$$

Note that this is indeed the staggered magnetization since the roles of $\hat{\eta}^z$ and $\hat{c}$ are switched between the two sub-lattices. All mean-field parameters, $a_\perp$, a_z, $b_\perp$, b_z and m, are real since the corresponding operators are hermitian. After Fourier

transform,

$$\hat{c}_\sigma(\mathbf{r}) = \frac{1}{\sqrt{2N}}\sum_{\mathbf{k}}\left\{e^{i\mathbf{kr}}\hat{c}^\dagger_\sigma(\mathbf{k})+e^{-i\mathbf{kr}}\hat{c}_\sigma(\mathbf{k})\right\}, \tag{5.19}$$

$$\hat{\eta}^z_\sigma(\mathbf{r}) = \frac{1}{\sqrt{2N}}\sum_{\mathbf{k}}\left\{e^{i\mathbf{kr}}(\hat{\eta}^z_\sigma)^\dagger(\mathbf{k})+e^{-i\mathbf{kr}}\hat{\eta}^z_\sigma(\mathbf{k})\right\}, \tag{5.20}$$

where N denotes the number of unit cells and the momenta $\mathbf{k}$ are from the hexagonal Brillouin zone ($\mathscr{BZ}$) shown in Fig. 5.2(a), the resulting mean-field Hamiltonian in momentum space is given by

$$\begin{aligned}\frac{\hat{\mathscr{H}}_{\rm mf}}{NK} &= \frac{i}{N}\sum_{\mathbf{k}}\hat{\Psi}^\dagger_{\mathbf{k}}\begin{pmatrix}0 & -\gamma_c^* & -M & 0\\ \gamma_c & 0 & 0 & -M\\ M & 0 & 0 & -\gamma_z^*\\ 0 & M & \gamma_z & 0\end{pmatrix}\hat{\Psi}_{\mathbf{k}} \\ &\quad -(1+\delta+\alpha)a_zb_z-2\alpha a_\perp b_\perp+(1+\delta+3\alpha)m^2.\end{aligned} \tag{5.21}$$

Here $\hat{\Psi}_{\mathbf{k}} = (\hat{c}_A(\mathbf{k}),\hat{c}_B(\mathbf{k}),\hat{\eta}^z_A(\mathbf{k}),\hat{\eta}^z_B(\mathbf{k}))^T$ and $M=(1+\delta+3\alpha)m$, for brevity, and we have defined the complex valued functions

$$\gamma_c(\mathbf{k}) = (1+\delta+\alpha)a_z+(1+\alpha a_\perp)\left(e^{i\mathbf{ka}_1}+e^{i\mathbf{ka}_2}\right), \tag{5.22}$$

$$\gamma_z(\mathbf{k}) = (1+\delta+\alpha)b_z+\alpha b_\perp\left(e^{i\mathbf{ka}_1}+e^{i\mathbf{ka}_2}\right). \tag{5.23}$$

The energy eigenvalues of the mean-field Hamiltonian are given by (in units of the Kitaev coupling K)

$$\begin{aligned}\varepsilon^2_{1,2}(\mathbf{k}) &= \frac{|\gamma_c|^2+|\gamma_z|^2}{2}+M^2 \\ &\quad \pm\sqrt{\left(\frac{|\gamma_c|^2-|\gamma_z|^2}{2}\right)^2+|\gamma_c+\gamma_z|^2M^2},\end{aligned} \tag{5.24}$$

resulting in the free energy density

$$\begin{aligned} f &= -t\sum_{n=1,2}\sum_{\sigma=\pm 1}\int_{\mathbf{k}} \ln\left(e^{-\sigma|\varepsilon_n(\mathbf{k})|/t}+1\right) \\ &\quad -(1+\delta+\alpha)a_z b_z - 2\alpha a_\perp b_\perp + (1+\delta+3\alpha)m^2, \end{aligned} \tag{5.25}$$

with $t = T/K$ the dimensionless temperature and

$$\int_{\mathbf{k}} \ldots = \frac{1}{V_{\mathscr{B}\mathscr{Z}}}\int_{\mathscr{B}\mathscr{Z}} d^2\mathbf{k}\ldots, \tag{5.26}$$

for brevity, where $V_{\mathscr{B}\mathscr{Z}}$ denotes the volume of the hexagonal Brillouin zone.

Minimizing the free-energy density f with respect to the mean-field parameters $\xi \in \{a_z, b_z, a_\perp, b_\perp, m\}$, $\partial_\xi f = 0$, we obtain the self-consistency equations

$$a_z = -\frac{1}{1+\delta+\alpha}\int_{\mathbf{k}} F_{b_z}(\boldsymbol{\xi},\mathbf{k}), \tag{5.27}$$

$$b_z = -\frac{1}{1+\delta+\alpha}\int_{\mathbf{k}} F_{a_z}(\boldsymbol{\xi},\mathbf{k}), \tag{5.28}$$

$$a_\perp = -\frac{1}{2\alpha}\int_{\mathbf{k}} F_{b_\perp}(\boldsymbol{\xi},\mathbf{k}), \tag{5.29}$$

$$b_\perp = -\frac{1}{2\alpha}\int_{\mathbf{k}} F_{a_\perp}(\boldsymbol{\xi},\mathbf{k}), \tag{5.30}$$

$$m = \frac{1}{2}\frac{1}{1+\delta+3\alpha}\int_{\mathbf{k}} F_m(\boldsymbol{\xi},\mathbf{k}), \tag{5.31}$$

where we have defined

$$F_\xi(\boldsymbol{\xi},\mathbf{k}) = \sum_{n=1,2}\tanh\left(\frac{|\varepsilon_n(\boldsymbol{\xi},\mathbf{k})|}{2t}\right)\partial_\xi|\varepsilon_n(\boldsymbol{\xi},\mathbf{k})|. \tag{5.32}$$

5.4 Kitaev Majorana Fermions

We will now discuss the mean-field scheme based on the local mapping of the spin-1/2 operators $\hat{\sigma}_i^\gamma$ ($\gamma = x,y,z$) to a set of four Majorana fermion operators $\hat{\eta}_i^\mu$, ($\mu = 0,x,y,z$) on each lattice site i, as discussed in the seminal paper by Kitaev [22]. The

Majorana fermion operators satisfy $(\hat{\eta}_i^\mu)^\dagger = \hat{\eta}_i^\mu$ and the Clifford algebra

$$\{\hat{\eta}_i^\mu, \hat{\eta}_j^\nu\} = 2\delta_{ij}\delta_{\mu\nu}. \tag{5.33}$$

In terms of the Majorana fermions the spin operators are expressed as

$$\hat{\sigma}_i^\gamma = i\hat{\eta}_i^0\hat{\eta}_i^\gamma. \tag{5.34}$$

This Majorana representation of spins is over-complete and the physical Hilbert space is obtained by imposing the local constraint $\hat{\eta}_i^0\hat{\eta}_i^x\hat{\eta}_i^y\hat{\eta}_i^z = 1$. It is indeed straightforward to check that the constraint ensures that the spin commutator relations are preserved. Using the properties of the Majorana fermion operators, Eq. (5.33), it is possible to rewrite the constraint as [209]

$$\hat{\eta}_i^0\hat{\eta}_i^\gamma + \frac{1}{2}\varepsilon_{\alpha\beta\gamma}\hat{\eta}_i^\alpha\hat{\eta}_i^\beta = 0, \tag{5.35}$$

which is quadratic in the Majorana operators. Since the antiferromagnetism will develop along the z direction in spin space, it is sufficient to use the constraint $\hat{\eta}_i^0\hat{\eta}_i^z + \hat{\eta}_i^x\hat{\eta}_i^y = 0$. We follow Ref. [209] and impose the constraint through a Lagrange multiplier field λ_i,

$$\delta\hat{H}_\lambda = iK\sum_i \lambda_i(\hat{\eta}_i^0\hat{\eta}_i^z + \hat{\eta}_i^x\hat{\eta}_i^y). \tag{5.36}$$

While λ_i is not expected to enlarge the two-site unit cell of the honeycomb lattice, it could take different values on the A and B sites within the unit cell. We found that $\lambda_A = \lambda_B = 0$ in the gapless and gapped QSL phases and $\lambda_A = -\lambda_B \neq 0$ in the antiferromagnetic phase. From now on we will therefore only include a single Lagrange multiplier

$$\lambda = \lambda_A = -\lambda_B. \tag{5.37}$$

In the following we will define $\hat{c}_i = \hat{\eta}_i^0$ to aid comparison with the mean-field theory based on the two-dimensional JWT. Expressing the spin operators in

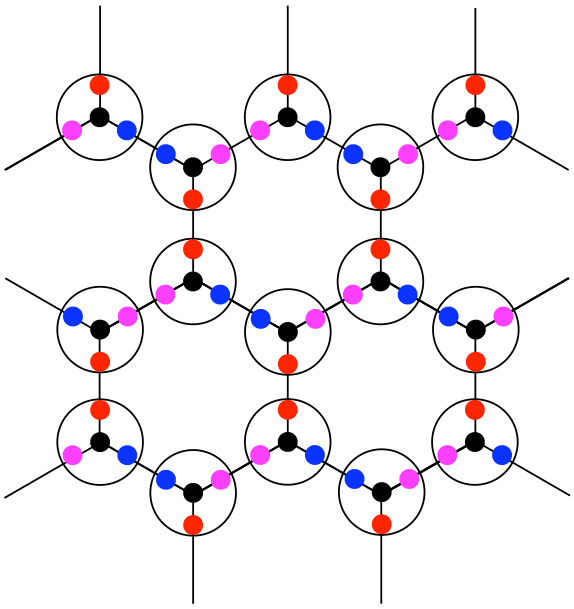

Figure 5.3: Using the Kitaev construction, each $S = 1/2$ spin operator is represented in terms of a set of four Majorana fermions, subject to a local constraint.

terms of Majorana fermions, using Eq. (5.34), the Hamiltonian contains only quartic interaction terms,

$$\begin{aligned}\hat{H}/K &= \sum_{\mathbf{r}} \{\hat{c}_A(\mathbf{r})\hat{c}_B(\mathbf{r}+\mathbf{a}_1)\hat{\eta}^x_A(\mathbf{r})\hat{\eta}^x_B(\mathbf{r}+\mathbf{a}_1) \\ &\quad +\hat{c}_A(\mathbf{r})\hat{c}_B(\mathbf{r}+\mathbf{a}_2)\hat{\eta}^y_A(\mathbf{r})\hat{\eta}^y_B(\mathbf{r}+\mathbf{a}_2) \\ &\quad +(1+\delta+\alpha)\hat{c}_A(\mathbf{r})\hat{c}_B(\mathbf{r})\hat{\eta}^z_A(\mathbf{r})\hat{\eta}^z_B(\mathbf{r})\} \\ &\quad +\alpha\sum_{\mathbf{r}}\sum_{i=1,2}\hat{c}_A(\mathbf{r})\hat{c}_B(\mathbf{r}+\mathbf{a}_i)\hat{\eta}^z_A(\mathbf{r})\hat{\eta}^z_B(\mathbf{r}+\mathbf{a}_i).\end{aligned} \tag{5.38}$$

5.4.1 Mean-field theory

As for the case of the $2d$ JWT we will perform a simultaneous mean-field decoupling in the bond and site-diagonal magnetic channels. We introduce the bond mean-field parameters

$$A^{\gamma}_{\mathbf{r},\mathbf{r}'} = i\langle\hat{\eta}^{\gamma}_A(\mathbf{r})\hat{\eta}^{\gamma}_B(\mathbf{r}')\rangle, \tag{5.39}$$

$$B_{\mathbf{r},\mathbf{r}'} = i\langle\hat{c}_A(\mathbf{r})\hat{c}_B(\mathbf{r}')\rangle, \tag{5.40}$$

and define $A_\perp = A^x_{\mathbf{r},\mathbf{r}+\mathbf{a}_1} = A^y_{\mathbf{r},\mathbf{r}+\mathbf{a}_2}$, $A'_\perp = A^z_{\mathbf{r},\mathbf{r}+\mathbf{a}_i}$, $A_z = A^z_{\mathbf{r},\mathbf{r}}$, $B_\perp = B_{\mathbf{r},\mathbf{r}+\mathbf{a}_i}$, $B_z = B_{\mathbf{r},\mathbf{r}}$ for the relevant nearest neighbor bonds. The staggered magnetization is given by the expectation values

$$m = i\langle \hat{c}_A(\mathbf{r})\hat{\eta}^z_A(\mathbf{r})\rangle = -i\langle \hat{c}_B(\mathbf{r})\hat{\eta}^z_B(\mathbf{r})\rangle. \tag{5.41}$$

After mean-field decoupling and Fourier transformation, as defined in Eqs. (5.19,5.20), the mean-field Hamiltonian is

$$\begin{aligned}
\frac{\hat{\mathscr{H}}_{\rm mf} + \delta\mathscr{H}_\lambda}{KN} &= \frac{i}{N}\sum_{\mathbf{k}}\Big\{ \\
&\hat{\Psi}^\dagger_{\mathbf{k}}\begin{pmatrix} 0 & -\gamma_c^* & -(M-\lambda) & 0 \\ \gamma_c & 0 & 0 & (M-\lambda) \\ (M-\lambda) & 0 & 0 & -\gamma_z^* \\ 0 & -(M-\lambda) & \gamma_z & 0 \end{pmatrix}\hat{\Psi}_{\mathbf{k}} \\
&+\hat{\Phi}^\dagger_{\mathbf{k}}\begin{pmatrix} 0 & -\gamma_x^* & \lambda & 0 \\ \gamma_x & 0 & 0 & -\lambda \\ -\lambda & 0 & 0 & -\gamma_y^* \\ 0 & \lambda & \gamma_y & 0 \end{pmatrix}\hat{\Phi}_{\mathbf{k}}\Big\} \\
&+(1+\delta+\alpha)A_zB_z + 2\tilde{A}_\perp B_\perp + (1+\delta+3\alpha)m^2,
\end{aligned} \tag{5.42}$$

where $\Psi_{\mathbf{k}} = \left(\hat{c}_A(\mathbf{k}), \hat{c}_B(\mathbf{k}), \hat{\eta}^z_A(\mathbf{k}), \hat{\eta}^z_B(\mathbf{k})\right)^T$, $\Phi_{\mathbf{k}} = \left(\hat{\eta}^x_A(\mathbf{k}), \hat{\eta}^x_B(\mathbf{k}), \hat{\eta}^y_A(\mathbf{k}), \hat{\eta}^y_B(\mathbf{k})\right)^T$, $M = (1+\delta+3\alpha)m$, $\tilde{A}_\perp = A_\perp + \alpha A'_\perp$,

$$\gamma_c(\mathbf{k}) = (1+\delta+\alpha)A_z + \tilde{A}_\perp\left(e^{i\mathbf{k}\mathbf{a}_1} + e^{i\mathbf{k}\mathbf{a}_2}\right), \tag{5.43}$$

$$\gamma_z(\mathbf{k}) = (1+\delta+\alpha)B_z + \alpha B_\perp\left(e^{i\mathbf{k}\mathbf{a}_1} + e^{i\mathbf{k}\mathbf{a}_2}\right), \tag{5.44}$$

$\gamma_x(\mathbf{k}) = B_\perp e^{i\mathbf{k}\mathbf{a}_1}$ and $\gamma_y(\mathbf{k}) = B_\perp e^{i\mathbf{k}\mathbf{a}_2}$. The resulting energy eigenvalues $\pm|\varepsilon_{1,2}(\mathbf{k})|$

and $\pm|\varepsilon_{3,4}(\mathbf{k})|$ are given by

$$\begin{aligned}\varepsilon^2_{1,2}(\mathbf{k}) &= \frac{|\gamma_c|^2+|\gamma_z|^2}{2}+(M-\lambda)^2 \\ &\quad \pm\sqrt{\left(\frac{|\gamma_c|^2-|\gamma_z|^2}{2}\right)^2+|\gamma_c-\gamma_z|^2(M-\lambda)^2}, \qquad (5.45)\\ \varepsilon^2_{3,4}(\mathbf{k}) &= B_\perp^2+\lambda^2\pm\lambda|\gamma_x-\gamma_y| \qquad (5.46)\\ &= B_\perp^2+\lambda^2\pm 2B_\perp\lambda\sin\left(\frac{\sqrt{3}}{2}k_x\right).\end{aligned}$$

Minimizing the free-energy density,

$$\begin{aligned}f &= -t\sum_{n=1}^{4}\sum_{\sigma=\pm1}\int_{\mathbf{k}}\ln\left(e^{-\sigma|\varepsilon_n(\mathbf{k})|/t}+1\right) \qquad (5.47)\\ &\quad +(1+\delta+\alpha)A_zB_z+2\tilde{A}_\perp B_\perp+(1+\delta+3\alpha)m^2,\end{aligned}$$

with respect to $\xi\in\{A_z,B_z,\tilde{A}_\perp,B_\perp,m\}$, $\partial_\xi f=0$, we obtain the self-consistency equations

$$\begin{aligned}A_z &= \frac{1}{1+\delta+\alpha}\int_{\mathbf{k}}F_{B_z}(\boldsymbol{\xi},\mathbf{k}), \qquad (5.48)\\ B_z &= \frac{1}{1+\delta+\alpha}\int_{\mathbf{k}}F_{A_z}(\boldsymbol{\xi},\mathbf{k}), \qquad (5.49)\\ \tilde{A}_\perp &= \frac{1}{2}\int_{\mathbf{k}}F_{B_\perp}(\boldsymbol{\xi},\mathbf{k}), \qquad (5.50)\\ B_\perp &= \frac{1}{2}\int_{\mathbf{k}}F_{\tilde{A}_\perp}(\boldsymbol{\xi},\mathbf{k}), \qquad (5.51)\\ m &= \frac{1}{2}\frac{1}{1+\delta+3\alpha}\int_{\mathbf{k}}F_m(\boldsymbol{\xi},\mathbf{k}), \qquad (5.52)\end{aligned}$$

where the functions $F_\xi(\boldsymbol{\xi},\mathbf{k})$ are defined as in Eq. (5.32) but with the sum running over the four bands $n=1,\ldots,4$ given in Eqs. (5.45) and (5.46).

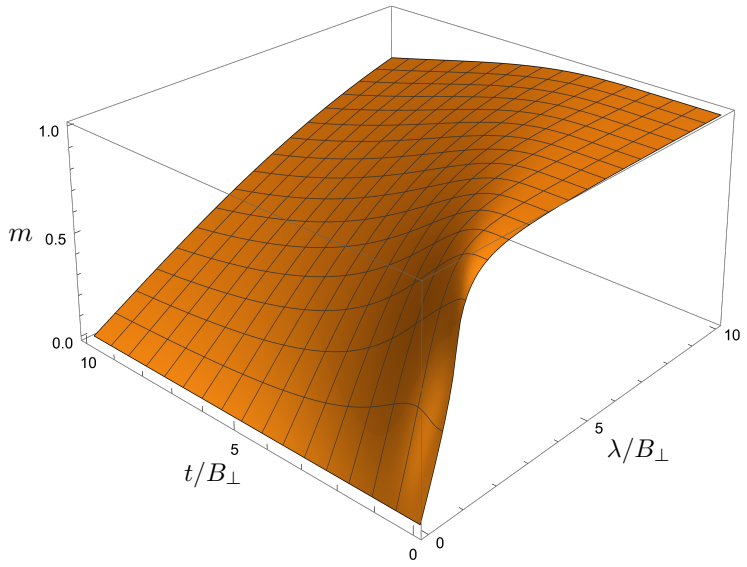

Figure 5.4: The function $m = \Omega(\lambda/B_\perp, t/B_\perp)$ relating the Lagrange multiplier λ to the staggered magnetization m, the bond mean-field parameter $B_\perp$ and the dimensionless temperature $t = T/K$.

5.4.2 Determination of the Lagrange multiplier

The Lagrange multiplier λ is closely linked to the staggered magnetization m, which satisfies the self-consistency equation

$$m = \frac{1}{2}\sum_{n=1,2}\int_{\mathbf{k}} \tanh\left(\frac{|\varepsilon_n(\mathbf{k})|}{2t}\right)\partial_M|\varepsilon_n(\mathbf{k})|, \tag{5.53}$$

where $M = (1+\delta+3\alpha)m$. Note that the bands $n = 3,4$ do not depend on M. From $\partial_\lambda f = 0$ and using that $\partial_\lambda\{|\varepsilon_1(\mathbf{k})|+|\varepsilon_2(\mathbf{k})|\} = -\partial_M\{|\varepsilon_1(\mathbf{k})|+|\varepsilon_2(\mathbf{k})|\}$ we obtain

$$\begin{aligned} m &= \frac{1}{2}\sum_{n=3,4}\int_{\mathbf{k}} \tanh\left(\frac{|\varepsilon_n(\mathbf{k})|}{2t}\right)\partial_\lambda|\varepsilon_n(\mathbf{k})| \\ &= \Omega\left(\frac{\lambda}{B_\perp}, \frac{t}{B_\perp}\right), \end{aligned} \tag{5.54}$$

where the function Ω is independent of m and given by the momentum integral

$$\begin{aligned}\Omega(x,y) &= \frac{1}{2}\sum_{\kappa=\pm 1}\int_{\mathbf{k}}\partial_x\sqrt{1+x^2+2\kappa x\sin\left(\sqrt{3}/2\,k_x\right)} \\ &\quad\times\tanh\left(\frac{\sqrt{1+x^2+2\kappa x\sin\left(\sqrt{3}/2\,k_x\right)}}{2y}\right).\end{aligned} \tag{5.55}$$

It is straightforward to compute the function $\Omega(x,y)$ numerically. The resulting relation between m, $\lambda/B_\perp$ and $t/B_\perp$ is shown in Fig. 5.4 for positive values of the staggered magnetization. The domain of negative magnetizations is obtained for negative Lagrange multipliers, $\Omega(-x,y)=-\Omega(x,y)$. This result shows that the Lagrange multiplier is zero in the non-magnetic phases and non-zero if the staggered magnetization is finite.

In the following, we will minimize the free-energy density f (5.47) at given temperature t with respect to the mean-field parameters A_z, B_z, $\tilde{A}_\perp$, $B_\perp$ and m by solving the corresponding self-consistency integral equations iteratively. At each step of the iteration we determine the Lagrange multiplier λ from the values of $B_\perp$ and m, using the equation $m=\Omega(\lambda/B_\perp, t/B_\perp)$.

5.5 Results

5.5.1 Topological Phase Transition

We start by discussing the zero-temperature topological phase transition between the gapless and gapped Kitaev QSL states as a function of the anisotropy $\delta = (K_z-K)/K$ of the Kitaev couplings and the relative strength $\alpha = J/K$ of the Ising coupling.

For $\alpha=0$ the Kitaev model is exactly solvable and the topological phase transition is known to occur at $\delta_c=1$, as derived in the triangle inequalities in Kitaev's original paper [22]. At this point the Dirac points of the dispersive low energy band merge, forming a semi Dirac point. We expect that the anisotropy induced by the Ising coupling α has a similar effect. However, sufficiently strong α will induce an antiferromagnetic state, which we will consider later.

In the absence of magnetization, $m = 0$, the dispersion of the low-energy band is simply given by $\pm|\gamma_c(\mathbf{k})|$, where $\gamma_c(\mathbf{k}) = u + v\left(e^{i\mathbf{k}\mathbf{a}_1} + e^{i\mathbf{k}\mathbf{a}_2}\right)$. The coefficients u and v are functions of δ, α and of the mean-field parameters, as defined in Eq. (5.22) for the JWT and in Eq. (5.43) for the Kitaev representation.

Rather than computing the momentum separation of the Dirac points in the gapless QSL or the the size of the energy gap on the other side of the transition, it is more convenient to compute the ratio $r = |u/v|$. While for $r < 2$ the band exhibits gapless Dirac points at zero energy, for $r > 2$ the Majorana fermion spectrum becomes gapped. We can therefore simply determine the topological phase transition at $r_c = 2$ by using a bi-section method.

Let us first determine the topological phase boundary using the mean-field theory based on the JWT. In this case the parameter $r = |u/v|$ is given by

$$r := \frac{(1+\delta+\alpha)|a_z|}{1+\alpha a_\perp}. \tag{5.56}$$

For $\alpha = 0$ the Kitaev model is exactly solvable in terms of Jordan-Wigner fermions since the local operator $(\hat{c}^\dagger_{A,\mathbf{r}} + \hat{c}_{A,\mathbf{r}})(\hat{c}^\dagger_{B,\mathbf{r}} - \hat{c}_{B,\mathbf{r}}) = -i\hat{\eta}^z_A(\mathbf{r})\hat{\eta}^z_B(\mathbf{r})$ commutes with the Hamiltonian. Although we don't require a mean-field treatment in this case, it is interesting to understand how the correct value of the topological phase transition, $\delta_c = 1$ ($K_z/K = 2$), is recovered within our mean-field theory. In fact, the mean-field theory becomes trivial for the pure anisotropic Kitaev model since the local flux excitations are dispersionless, with corresponding bands at energies $\pm|\gamma_z(\mathbf{k})| = \pm(1+\delta)|b_z|$. The free energy is independent of the mean-field parameters $a_\perp$ and $b_\perp$ and at zero temperature, $t = 0$, we obtain the mean-field parameters a_z and b_z from minimizing the energy

$$\begin{aligned}\varepsilon(a_z, b_z) &= -\frac{1}{V_{\mathscr{B}\mathscr{Z}}}\int_{\mathscr{B}\mathscr{Z}} d^2\mathbf{k}\left|(1+\delta)a_z + e^{i\mathbf{k}\mathbf{a}_1} + e^{i\mathbf{k}\mathbf{a}_2}\right| \\ &\quad -(1+\delta)(|b_z| + a_z b_z).\end{aligned} \tag{5.57}$$

From $\partial\varepsilon/\partial b_z = 0$ we obtain $a_z = 1$ if $b_z < 0$ and $a_z = -1$ if $b_z > 0$, regardless of the value of the anisotropy δ. Let us focus on the first case. Inserting $a_z = 1$ into

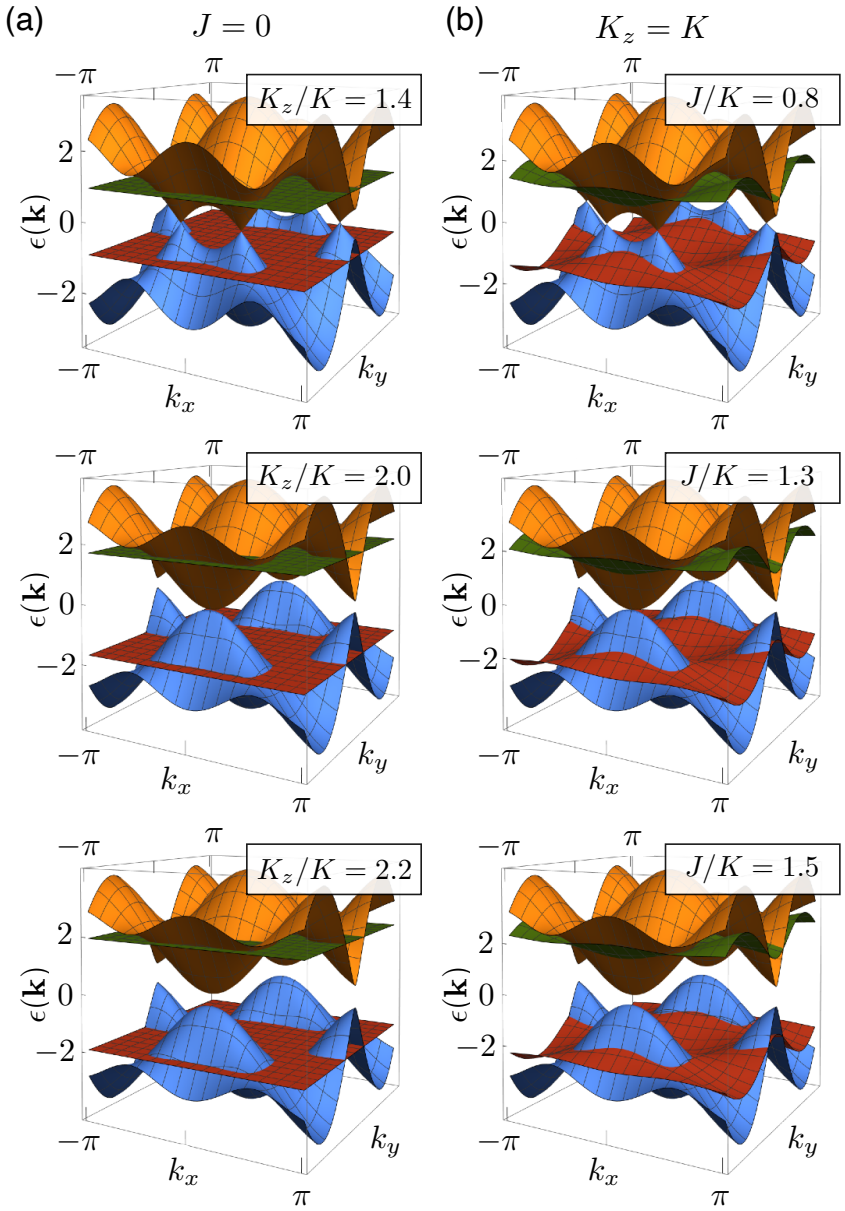

Figure 5.5: Evaluation of the Majorana fermion mean-field spectra across the topological phase transition between a gapless and gapped Kitaev QSL, as a function of (a) the anisotropy K_z/K in the pure Kitaev model and (b) the Ising coupling J/K in the case $K_z = K$. Note that the two mean-field schemes give identical results. At the topological phase transition the Dirac points merge along the edge of the Brillouin zone, as schematically shown in Fig. 5.1(b).

$\partial\varepsilon/\partial a_z = 0$ we obtain

$$b_z = -\frac{1}{V_{\mathscr{B}\mathscr{Z}}}\int_{\mathscr{B}\mathscr{Z}} d^2\mathbf{k}\frac{\cos(\mathbf{k}\mathbf{a}_1)+\cos(\mathbf{k}\mathbf{a}_2)}{|1+\delta+e^{i\mathbf{k}\mathbf{a}_1}+e^{i\mathbf{k}\mathbf{a}_2}|}, \tag{5.58}$$

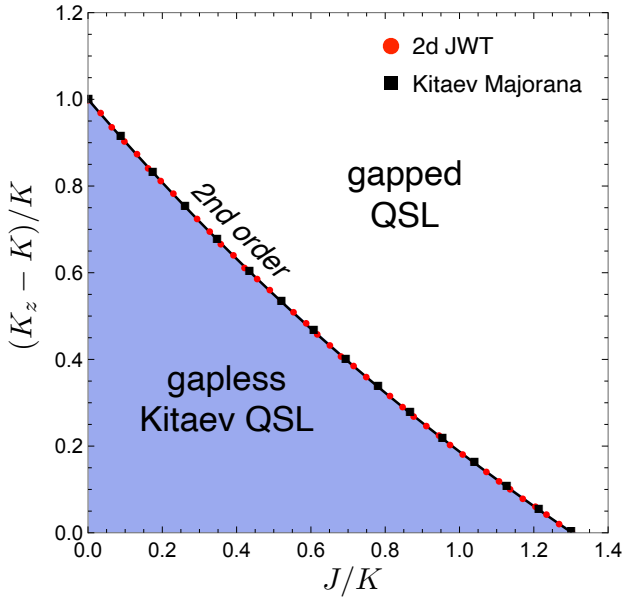

Figure 5.6: Topological phase boundary between a gapless and gapped Kitaev QSL as a function of the Ising coupling $\alpha = J/K$ and the anisotropy $\delta = (K_z - K)/K$ of the Kitaev couplings. Note that the mean field schemes based on the two-dimensional JWT and on the Kitaev Majorana representation give identical results. Potential magnetic instabilities are not considered here.

which is indeed negative. Note that for $a_z = -1$ we obtain the same value for b_z but with a positive sign. This solution is equivalent to the first solution but with a momentum shift of the entire excitation spectrum. We obtain $r = 1 + \delta$, and hence a topological phase transition at $\delta_c = 1$, which is equivalent to $K_z/K = 2$.

The resulting mean-field spectra are shown in Fig. 5.1(a) for different values of δ. With increasing δ the Dirac points approach each other along one of the edges of the hexagonal Brillouin zone, as illustrated in Fig. 5.1(b), and merge at $\delta_c = 1$, forming a semi-Dirac point. For $\delta > 1$ the spectrum becomes gapped. The other bands remain gapped and dispersionless across the topological phase transitions and only slightly change in energy.

As a next step we investigate the effect of the Ising coupling $\alpha = J/K$ on the isotropic Kitaev model, $\delta = 0$ ($K_z = K$). From Eqs. (5.22) and (5.23) it is clear that the gapped bands of flux excitations become weakly dispersive and that the Ising coupling induces anisotropy in the gapless Majorana bands. For $\alpha > 0$ the mean-field theory is no longer trivial and the free energy becomes a function of

the four mean-field parameters a_z, b_z, $a_\perp$ and $b_\perp$. As shown in Fig. 5.5(b), the effect of the Ising coupling on the gapless Dirac band is very similar to that of the anisotropy in the Kitaev couplings, and the system undergoes a topological phase transition at $\alpha_c \approx 1.3$. However, we expect that this transition will be pre-empted by an antiferromagnetic instability. The topological phase boundary as a function of both, δ and α is shown in Fig. 5.6.

We briefly discuss the mean-field theory for the topological phase transition base on the Kitaev Majorana representation. This treatment involves a larger number of degrees of freedom with one gapless Dirac band and three gapped bands of flux excitations. In addition, we have to incorporate a Lagrange multiplier λ to enforce the local constraints on the Majorana fermions. However, as we have seen in Sec. 5.4.2, λ is identical to zero in the non-magnetic QSL states. This leads to a drastic simplification of the spectrum since for $\lambda = 0$ the η_x and η_y bands don't hybridize and remain flat across the topological transition with degenerate energies $\pm|\gamma_x(\mathbf{k})| = \pm|\gamma_y(\mathbf{k})| = \pm B_\perp$, even if the Ising coupling α is included. For all values of the anisotropy δ and the Ising coupling α the mean-field dispersions $\pm|\gamma_c(\mathbf{k})|$ and $\pm|\gamma_z(\mathbf{k})|$ of the other two Majorana bands are identical to those of the two Majorana bands in the JWT treatment. It is therefore not surprising that the two mean-field treatments result in identical phase boundaries for the topological phase transition between the gapless and gapped Kitaev QSLs, as shown in Fig. 5.6.

5.5.2 Antiferromagnetism

In the previous section we have not included the possibility of the formation of an antiferromagnetic state with finite staggered magnetization m. For $m \neq 0$ the Lagrange multiplier λ in the Kitaev Majorana mean-field theory is no longer zero and acquires a value of the order of the magnetization (see Fig. 5.4). As a result, the η_x and η_y Majorana fermions hybridize and form dispersive bands with energies $\pm\varepsilon_{3,4}(\mathbf{k})$ (5.46). This shows that the η_x, η_y fermions are not simply spectators as in the case of the topological phase transition but play a crucial role in the energetics of the antiferromagnetic transition. Since these degrees of freedom are neglected in the JWT with fixed string orientation, we expect that the corresponding mean-field

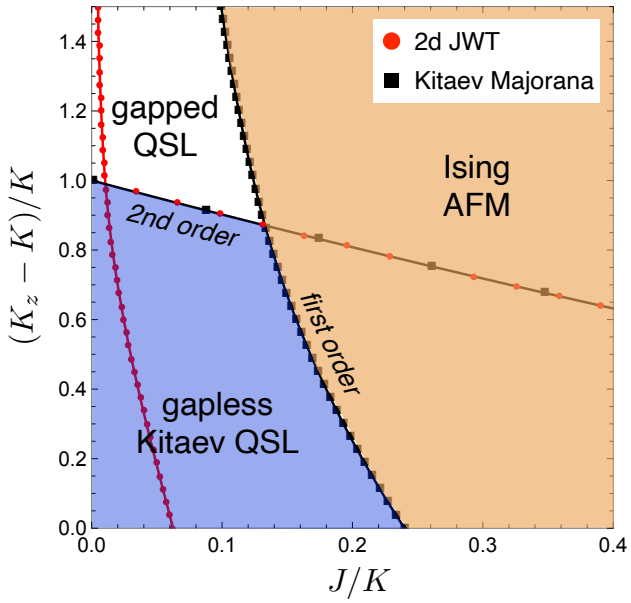

Figure 5.7: Zero-temperature phase diagram of the anisotropic Kitaev-Ising model as a function of the relative strength $\alpha = J/K$ of the Ising coupling and the anisotropy $\delta = (K_z - K)/K$ of the Kitaev couplings. While the two mean-field theories give identical phase boundaries for the topological phase transition between the gapless and gapped Kitaev QSLs, the treatment based on the JWT fails to correctly describe the first-order transition to the antiferromagnetically ordered state.

theory does not correctly describe the magnetic instability.

As shown in Fig. 5.7, there is indeed a significant discrepancy between the zero-temperature magnetic phase boundaries calculated within the two mean-field theories. We find that the magnetic phase transition is strongly first order with a jump in magnetization close to the fully polarized value. This is not surprising. The antiferromagnetic ordering is driven by an Ising exchange and as a result quantum fluctuations are frozen out at low temperatures, resulting in a large ordered moment. Moreover, transverse spin fluctuations are active only along the one-dimensional zig-zag chains formed by the x and y bonds.

5.5.3 Finite Temperature Phase Diagram

In the previous section we have identified problems with the mean-field theory based on the JWT for states with finite magnetization. Neglecting the flux excitations of the $\hat{\eta}^x$ and $\hat{\eta}^y$ Majorana fermions by using a particular gauge choice of the string operator in the 2d JWT, we also induce pathologies at finite temperatures.

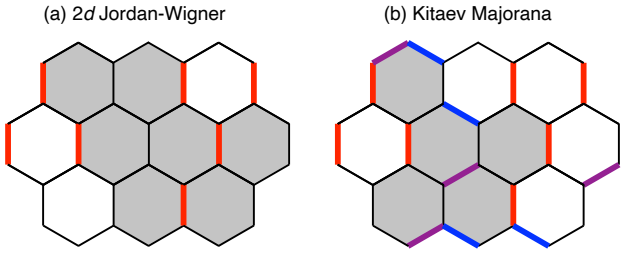

Figure 5.8: Illustration of the flux excitations in terms of the (a) $2d$ JWT and (b) the Kitaev Majorana representation. Excited bonds are shown as thick lines and plaquettes with non-zero flux are shaded grey.

In order to illustrate this we focus on the pure isotropic Kitaev model. In this case we obtain the mean-field dispersions $\varepsilon_1(\mathbf{k}) = |\gamma_c(\mathbf{k})| = |a_z + e^{i\mathbf{k}\mathbf{a}_1} + e^{i\mathbf{k}\mathbf{a}_2}|$ for the dispersive Dirac band and $\varepsilon_2(\mathbf{k}) = |\gamma_z(\mathbf{k})| = |b_z|$ for the flat band. As discussed in Sec. 5.5.1, at zero temperature the minimization of the energy density $\varepsilon(a_z, b_z)$ with respect to a_z and b_z results in two equivalent mean-field solutions, e.g. one with a negative value of b_z and $a_z = 1$. This reproduces the correct excitation spectrum of the isotropic Kitaev model with Dirac points at the corners of the hexagonal Brillouin zone. Let us now investigate the mean-field solution at finite temperature $t = T/K$. Minimizing the free energy density $f(a_z, b_z)$ with respect to b_z we obtain the simple relation

$$a_z = -\tanh\left(\frac{b_z}{2t}\right). \tag{5.59}$$

While for $b_z < 0$ we recover $a_z = 1$ as $t \to 0$, at any finite temperature $a_z < 1$. This corresponds to a mean-field dispersion with Dirac points displaced along the edges of the Brillouin zone, in the same way as for an anisotropic Kitaev model with $K_z < K$. This is clearly unphysical and caused by an artificial symmetry breaking due to the fixed orientation of the string operator.

The different finite-temperature response of the JWT and Kitaev-Majorana mean-field treatments can also be understood in terms of thermal excitations of the gapped flux excitations. As pointed out by Kitaev [22], expressing the spin-1/2 operators as $\hat{\sigma}_i^\gamma = i\hat{\eta}_i^0\hat{\eta}_i^\gamma$ ($\gamma = x, y, z$), the Z_2 flux through a hexagon is given by the product $\hat{W}_p$ of the nearest-neighbor bond operators $\hat{A}^\gamma_{\langle i,j\rangle_\gamma} = i\hat{\eta}_i^\gamma\hat{\eta}_j^\gamma$ around the plaquette. The bond operators square up to the identity operator and hence have

eigenvalues plus or minus one. The plaquette carries a flux if an odd number of bonds around it are excited ($\hat{W}_p = -1$). In the case of the pure (anisotropic) Kitaev model, the bond operators are local and $\hat{W}_p$ commutes with the Hamiltonian. As a result, the Hamiltonian can be diagonalised for each flux configuration and the ground state corresponds to the zero flux sector, resulting in a non-interacting Hamiltonian for the dispersive $\hat{\eta}^0$ Majorana fermion.

Both the $2d$ JWT and the Kitaev Majorana approaches correctly describe the zero flux sector and hence the ground-state properties of the anisotropic Kitaev model. At first glance, it might seem that the two approaches enumerate flux excitations differently since the JWT only includes bond excitations on the z links. However, the choice of the string operator in the JWT is a gauge degree of freedom and the Kitaev Majorana fermions are subject to local constraints. In the end, both mappings are exact and therefore equivalent. The problems arise when the finite-temperature mean-field average over bond operators is taken for a fixed orientation of the string. In Fig. 5.8 the bond excitations and resulting fluxes are sketched for the two approaches.

It is also worth mentioning that for the particular Kitaev-Ising model only the bond excitations on the z links acquire dynamics, resulting in the same mean-field dispersion of the $\hat{\eta}_z$ Majorana fermion as in the mean-field treatment based on the JWT. This is the reason why both approaches result in the same zero-temperature phase boundary for the topological phase transition between the gapless and gapped QSL states. Note that this is a special feature of the Ising exchange J. For a Heisenberg coupling the $\hat{\eta}_x$ and $\hat{\eta}_y$ fermions acquire dynamics as well.

Because of the problems with the finite temperature mean-field theory based on the two-dimensional JWT, we will use the Kitaev Majorana fermion representation to determine finite temperature phase diagrams, following the procedure outlined in Sec. 5.4. In Fig. 5.8 a representative phase diagram is shown as a function of the Ising coupling $\alpha = J/K$ and the dimensionless temperature $t = T/K$ for a fixed values $\delta = 0.2$ of the anisotropy of the Kitaev couplings. For this value of δ we find a zero-temperature phase transition from a gapless Kitaev QSL to an antiferromag-

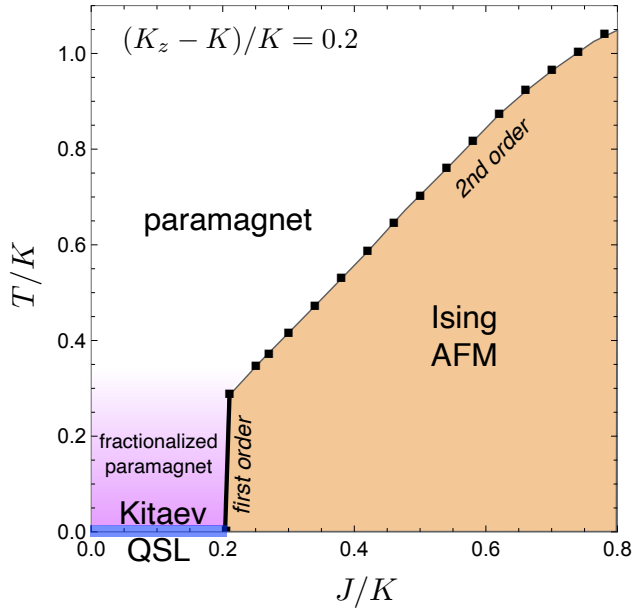

Figure 5.9: Finite-temperature mean-field phase diagram of the anisotropic Kitaev-Ising model as a function of the relative strength of the Ising coupling $\alpha = J/K$ and the dimensionless temperature $t = T/K$ for a value of $\delta = 0.2$ of the anisotropy of the Kitaev couplings.

netic state at $\alpha_c \approx 0.2$. This transition is strongly first order. At small temperatures the antiferromagnetic transition remains first order and is very steep. As one might expect, the magnetic transition becomes continuous above a certain temperature.

Let us now investigate the finite-temperature behavior in the regime of small values of J/K where the zero-temperature ground state is a gapless Kitaev QSL. An important energy scale is the gap Δ of the flux excitations which is equal to $\Delta/K \approx 0.26$ for the isotropic Kitaev model [22]. While for $T \ll \Delta$ the typical separation between fluxes is exponentially large and the thermal average of the flux operator $\langle \hat{W}_p \rangle$ close to $+1$, at temperatures $T > \Delta$, the flux excitations proliferate with high probability on all plaquettes, resulting in $\langle \hat{W}_p \rangle = 0$ of the flux operator. One might therefore expect a finite-temperature confinement transition from a QSL with deconfined Majorana fermions to a paramagnet where the Majorana fermions are confined via the flux excitations of the emergent Z_2 gauge field [165]. However, it is known that in two dimensions gauge theories are confining at any non-zero temperature. Hence the Kitaev QSL exists only at zero temperature and even an exponentially small density of thermally excited fluxes is sufficient to destroy the

QSL state. Nevertheless, interesting finite temperature crossovers are seen in quantum Monte Carlo simulations of the two-dimensional Kitaev model, using Majorana fermion representations [200, 201, 210].

In order to identify finite-temperature crossovers, we compute the specific heat per unit cell,

$$C = -t\frac{\partial^2 f}{\partial t^2}, \tag{5.60}$$

where $f(t)$ denotes the mean-field free energy density $f = F/(NK)$ (5.47) as a function of the dimensionless temperature $t = T/K$. In Fig. 5.10 the temperature evolution of the specific heat is shown for systems with an anisotropy $\delta = 0.2$ of the Kitaev couplings and increasing values $\alpha = J/K$ of the Ising coupling, up to the value $\alpha = 0.2$, which is slightly below the critical value of the $t = 0$ first-order transition between the Kitaev QSL and the Ising antiferromagnet. Unlike in previous work using quantum Monte Carlo simulations of finite systems [200, 201, 210], where two separate specific-heat peaks are found, our mean-field results only show a single peak at a temperature $T \approx \Delta$, where Δ is the energy gap of flux excitations. Note that for the pure Kitaev model ($\alpha = 0$) the anisotropy $\delta = 0.2$ gives rise to a small splitting of the flux gaps, $\Delta_z/K \approx 0.29$ and $\Delta_\perp/K \approx 0.24$, resulting in a slight broadening of the crossover peak in the specific heat. With increasing Ising coupling α the splitting further increases up to values $\Delta_z/K \approx 0.32$ and $\Delta_\perp/K \approx 0.22$ for $\alpha = 0.2$. Note that α also gives dynamics to the bond excitations along the z links, adding to the broadening of the crossover. At high temperatures, $T > \Delta$, we recover a conventional paramagnet, and the Curie-Weiss dependence $C \sim 1/T$ is clearly observed above temperatures of the order of the bandwidth of the Majorana fermions. At temperature $T < \Delta$ flux excitations are exponentially suppressed and signatures of fractionalization become visible. The crossover to a fractionalized paramagnet at low temperatures is indicated by a color gradient in the phase diagram, Fig. 5.9. The energy scale of the crossover coincides with the point at which the magnetic phase transition becomes continuous.

The inset of Fig. 5.10 shows the specific heat contribution from the gapless Majorana fermion band at lowest temperatures. As expected, we observe the $C_0 \sim$

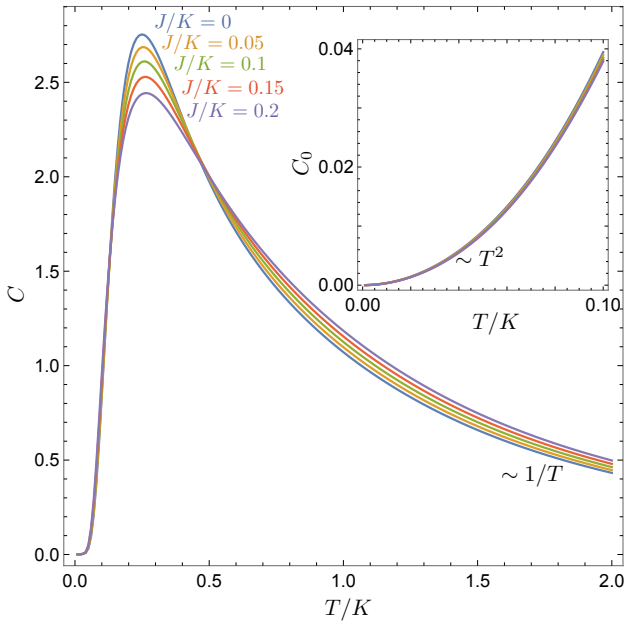

Figure 5.10: Specific heat C per unit cell as a function of the dimensionless temperature T/K, for an anisotropy $\delta = 0.2$ of the Kitaev couplings and different values of $\alpha = J/K$, corresponding to a gapless Kitaev QSL ground state. The peak is located at the energy scale of the gapped flux excitations and indicates a crossover from a fractionalized paramagnet with frozen flux excitations to a conventional paramagnet at high temperatures. In the latter the expected Curie dependence $C \sim 1/T$ is observed. The inset shows the low-temperature specific heat contribution C_0 of the gapless Majorana fermion band, showing the T^2 dependence expected for Dirac fermions in $d = 2$.

T^2 dependence expected for Dirac fermions in two spatial dimensions.

5.6 Discussion and Conclusion

In this chapter we have determined zero- and finite-temperature phase diagrams of the anisotropic, antiferromagnetic Kitaev-Heisenberg model on the honeycomb lattice, using parton mean-field theories based on two different Majorana fermion representations of the $S = 1/2$ spin operators: the one used by Kitaev [22] and a two-dimensional Jordan-Wigner transformation (JWT) [196, 197, 194, 198]. Both mappings have been used to obtain the exact solution of the anisotropic Kitaev model [22, 197].

In order to ensure that the Hamiltonian remains local after JWT, we studied a particular limit of the model, keeping the anisotropy in the Kitaev couplings finite while taking the extreme limit of an infinitely strong Ising anisotropy in the Heisen-

berg sector. For this model, it is possible to use the same snake-string operators in the JWT as for the pure anisotropic Kitaev model [196, 197, 194, 198], resulting in two Majorana modes. For sufficiently weak anisotropy and Ising coupling the low-energy band is gapless with Dirac points on the edges of the hexagonal Brillouin zone. The other band of gapped flux excitations is flat for the anisotropic Kitaev model but becomes weakly dispersive in the presence of the additional Ising coupling.

On the other hand, following Kitaev's approach [22], the spin-$1/2$ operators are mapped to a set of four Majorana fermions with three modes corresponding to gapped flux excitations. The Majorana fermion operators are subject to local constraints which we reformulated in a quadratic form and enforced through a Lagrange multiplier, following a previous study [209] of the magnetic field dependence of the pure Kitaev model.

Perhaps surprisingly, the two mean-field theories result in identical zero-temperature phase boundaries for the topological phase transition between the gapless and gapped Kitaev QSL states. The reason is that for an Ising exchange $\alpha = J/K$ only the bond excitations along the z links, which are accounted for in both approaches, acquire dynamics. The two additional gapped modes in the Kitaev mean-field theory remain flat across the transition and don't contribute to the physics. The mean-field dispersion of the remaining two bands is identical to the mean-field spectrum based on the JWT. The mean-field treatments give the correct value $K_z/K = 2$ for the topological phase transition of the anisotropic Kitaev model. The Ising coupling J/K is an additional source of anisotropy and cooperates with the anisotropy in the Kitaev couplings in driving the topological phase transition.

We demonstrated that all three bands of flux excitations play a crucial role for the antiferromagnetic instability and the finite-temperature behavior. The mean-field theory based on the two-dimensional JWT therefore fails to correctly describe the finite temperature phase diagrams. Even for an isotropic Kitaev model we found an anisotropic response at finite temperatures. We believe that this unphysical behavior is not an intrinsic problem of the two-dimensional JWT since the choice

of the string operator is a gauge degree of freedom. However, taking a finite-temperature mean-field average over the bond operators leads to artificial anisotropy that depends upon the choice of the string. Recent progress has been made in formulating a JWT in two and three dimensions that keeps locality and all relevant symmetries manifest [211, 208]. This is achieved through operators that create local deformations of the JW string operator. A mean-field theory based on such a gauge invariant formulation of the JWT would not suffer from artificial symmetry breaking. Given the increased complexity it remains unclear, however, if this approach if useful for practical calculations when dealing with realistic spin Hamiltonians.

We instead used the parton mean-field theory formulated in terms of the Kitaev Majorana fermions to obtain the finite-temperature phase diagram of the anisotropic Kitaev-Ising model. As expected, sufficiently strong Ising exchange results in a first-order transition from the gapless and gapped QSLs to an antiferromagnetic phase with fully gapped Majorana fermion spectrum. Unfortunately, we are not aware of numerical results in the literature for the magnetic instability of the antiferromagnetic Kitaev-Ising model. The critical mean-field value $(J/K)_c \approx 0.2$ for the first-order transition between the Kitaev QSL and the Ising antiferromagnet is considerably larger than the value $(J/K)_c \approx 0.035$ for the isotropic Kitaev-Heisenberg model, computed with tensor-network algorithms [212].

Although the QSL states only exist at zero temperature, the magnetic phase transition remains first order at low temperatures and becomes continuous above a certain temperature. While we believe that this behavior is generic and similar to other QSL systems, the first-order behavior is particularly strong for the present model. This is due to the extreme Ising anisotropy and the one-dimensionality of transverse spin fluctuations in the magnetically ordered phase.

At the temperature where the magnetic phase transition becomes second order we also observe a crossover on the QSL side from a fractionalised paramagnet at low temperatures with exponentially suppressed flux excitations to a conventional paramagnet at high temperatures. As expected, the crossover temperature scale, which we identify through a peak in the specific heat, is set by the energy gap Δ of

flux excitations, which is equal to $\Delta/K \approx 0.26$ for the isotropic Kitaev model [22] and slightly split into Δ_z and $\Delta_\perp$ by small anisotropy and the Ising exchange. This splitting leads to a broadening of the crossover.

Interestingly, quantum Monte-Carlo (QMC) simulations of (anisotropic) Kitaev models show a two step thermalization of the QSL state, identified by two clearly separated specific heat peaks at temperatures T_L and T_H [200, 201, 210]. This is in contrast with the single crossover we found within our mean-field treatment. For the isotropic Kitaev model the peaks are found at $T_L/K \approx 0.012$ and $T_H/K \approx 0.37$ [210]. Neither of the crossover temperatures is close to the flux gap $\Delta/K \approx 0.26$ [22] of the isotropic Kitaev model. The authors identify the lower temperature peak at T_L with the flux gap and attribute T_H to a feature in the density of states of the itinerant Majorana fermions. However, at T_H the entropy per spin drops from $\ln 2$ to $\frac{1}{2}\ln 2$ and the thermal average $\langle \hat{W}_p \rangle$ of the plaquette operator becomes non-zero, suggesting that flux excitations start to freeze out at the temperature T_H. The reason why we don't see a crossover at the much lower temperature T_L is likely because at mean-field level the local constraints on the Majorana fermions are only treated on average and the interaction vertex is not properly taken into account. Such correlation effects could give rise to the formation of a bound state at this new energy scale. The inclusion of diagrammatic corrections beyond mean-field could potentially provide an analytical confirmation of the QMC result.

The main purpose of our work was to compare different Majorana fermion mean-field theories for Kitaev QSLs. In order to ensure locality of the Hamiltonian after JWT we focused on a very specific, fine tuned spin model. A similar Kitaev-Ising model, but with ferromagnetic exchange couplings, was studied in Ref. [202] for the same reasons, e.g. to ensure locality after a two-dimensional JWT. Interestingly, in the regime of strong anisotropy of the Kitaev couplings this model exhibits a spin-nematic phase in between the gapped Kitaev QSL and the ferromagnetic phase.

It is important to stress that the parton mean-field theory based on the Kitaev mapping to a set of four Majorana fermions, subject to constraints enforced

by Lagrange multipliers, is applicable to a much wider class of extended Kitaev-Heisenberg models [188, 189, 190, 191, 192, 193, 213, 214, 215, 216, 217], including those relevant to real materials [169, 170, 171, 172, 173, 171, 174, 175, 176, 177, 178].

Chapter 6

Emergent Dirac Fermions in Kitaev Quantum Spin Liquids II: Renormalisation Group Analysis

The mean-field theory of the Kitaev-Ising model tells us that the topological phase transition between the gapless and gapped Z_2 spin liquids can also be induced in presence of other magnetic interactions. The phase transition is analogous to the semimetal-insulator transition of Dirac fermions in graphene, only now we have Majorana fermions instead of complex fermions. The additional magnetic interaction moves the system away from the exactly solvable point, thus acting like an interaction term on top of the free theory of Dirac fermions. This suggests that the underlying IR theory of such a phase transition could be described by a GNY-like theory! Bearing this in mind, we now derive the long-wavelength theory of the topological phase transition based on the mean-field dispersion in last chapter, and investigate the topological phase transition as a fermion-induced criticality of Majorana fermions.

The original work in this chapter was published in *Nature of Topological Phase Transition of Kitaev Quantum Spin Liquids*, H. Hu, F. Krüger, Physical Review Letters 133 (1), 146603.[218].

6.1 Introduction

The spin-$1/2$ honeycomb Kitaev model [22] [Fig. 6.1(a)] has been at the forefront of research into quantum spin liquids (QSLs) [163, 164, 165] since it is exactly solvable after fractionalizing the spin operators into a set of Majorana fermions [22, 194, 195]. Some of these correspond to local bond excitations which are linked to Z_2 fluxes through the plaquettes of the honeycomb lattice. Since the fluxes are conserved, the Kitaev model can be diagonalized for each flux configuration, resulting in a non-interacting Hamiltonian for the remaining Majorana fermion species. In the ground state, zero-flux sector, this results in a Dirac dispersion identical to that of electrons in graphene.

Anisotropy of the Kitaev couplings can drive a topological phase transition from a gapless to a gapped Z_2 Kitaev QSL [22]. In the regime of large anisotropy, the latter can be mapped to the toric code model which exhibits anyonic excitations and plays an important role in the context of quantum computation and quantum error correction [219]. Approaching the topological phase transition from the gapless QSL side, the Dirac points of the gapless Majorana bands move along the edge of the Brillouin zone [Fig. 6.1(b)] and eventually merge, forming a semi-Dirac point with a quadratic and a linear band touching direction. For larger anisotropies the spectrum becomes gapped. This behavior is very similar to the topological phase transition proposed to occur for electrons in strained honeycomb lattices [203, 204, 205] and was observed experimentally in black phosphorus [206, 207].

At first glance, the bond-directional exchange of the Kitaev model seems artificial, but it was realized that because of strong spin-orbital mixing [168, 220], the Kitaev model can be approximately realized in layered honeycomb iridates [169, 170, 171, 172, 173, 175, 174] and the halide α-$RuCl_3$ [176, 177, 178]. Although in these materials the additional magnetic interactions are still slightly too large, leading to magnetic ordering at low temperatures, the experimental realization of a Kitaev QSL is certainly within reach.

In the presence of additional magnetic interactions, such as Heisenberg or Gamma couplings [164, 188], the model is no longer exactly solvable since the flux

plaquette operators do not commute with the full Hamiltonian and the gapped Majorana modes, which correspond to flux excitations, acquire dynamics. While the selection of magnetically ordered states crucially depends on the nature of the additional couplings, the topological phase transition between the gapless and gapped Kitaev QSLs is expected to be universal.

In this chapter we analyze the nature of the topological quantum phase transition away from the exactly solvable point. To achieve this we perform a renormalization-group (RG) analysis of the effective Gross-Neveu-Yukawa (GNY) quantum field theory that describes the coupling of the dynamical Ising order parameter field to the gapless Majorana fermion semi-Dirac modes.

6.2 From Microscopic Model to Effective Field Theory

Instead of starting with the generic form of the effective field theory, we explicitly derive it for a specific microscopic model. Our starting point is the Kitaev model with couplings $K_\gamma > 0$ along nearest-neighbour bonds $\langle i,j\rangle_\gamma$ ($\gamma = x,y,z$), perturbed by an antiferromagnetic nearest-neighbor Ising exchange $J > 0$ [202, 162],

$$\hat{\mathscr{H}} = \sum_{\gamma=x,y,z} \sum_{\langle i,j\rangle_\gamma} K_\gamma \hat{\sigma}_i^\gamma \hat{\sigma}_j^\gamma + J \sum_{\langle i,j\rangle} \hat{\sigma}_i^z \hat{\sigma}_j^z. \tag{6.1}$$

Here the operators $\hat{\sigma}_i^\gamma$ denote spin-1/2 operators in units of $\hbar/2$, satisfying the spin-commutation algebra $[\hat{\sigma}_i^\alpha, \hat{\sigma}_j^\beta] = 2\delta_{ij}\varepsilon_{\alpha\beta\gamma}\hat{\sigma}_i^\gamma$. In order to drive a topological phase transition, we allow for anisotropy $K_z > K_x = K_y = K$. For $J = 0$, the topological phase transition is known to occur at $K_z/K = 2$ [22].

We map this Kitaev-Ising model to a Hamiltonian in terms of spinless fermions, using a two-dimensional Jordan-Wigner transformation (JWT) with a string operator along the one-dimensional contour shown in Fig. 6.1(c). The mapping, which was used as an alternative way to obtain the exact solution of the pure Kitaev model [194], is defined as $\hat{\sigma}_n^z = 1 - 2\hat{c}_n^\dagger \hat{c}_n = (\hat{c}_n^\dagger + \hat{c}_n)(\hat{c}_n^\dagger - \hat{c}_n)$, $\hat{\sigma}_n^x = \hat{D}_n(\hat{c}_n^\dagger + \hat{c}_n)$ and $\hat{\sigma}_n^y = i\hat{D}_n(\hat{c}_n^\dagger - \hat{c}_n)$. Here n labels the position along the

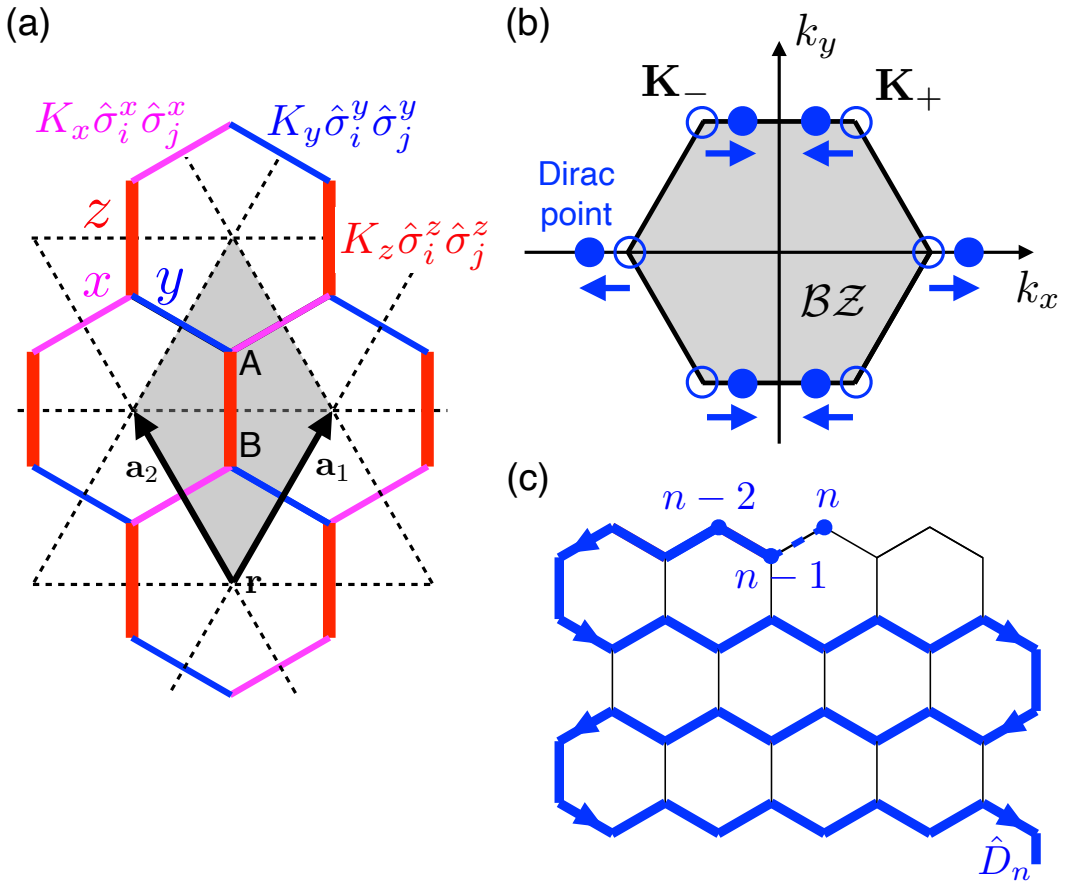

Figure 6.1: (a) Illustration of the bond-directional Ising exchanges $K_\gamma\hat{\sigma}_i^\gamma\hat{\sigma}_j^\gamma$ along the bonds $\gamma = x,y,z$ of the honeycomb Kitaev model. The unit cell contains two lattice sites (A,B) and is spanned by the lattice vectors $\mathbf{a}_{1,2} = (\pm\frac{\sqrt{3}}{2},\frac{3}{2})$. (b) As a function of anisotropy $(K_z - K)/K$ the Dirac points of the gapless Majorana bands move along the edge of the Brillouin zone and merge at the topological phase transition between the gapless and gapped QSL states. (c) Snake string operator used for the two-dimensional Jordan-Wigner transformation.

string and the string operator $\hat{D}_n = \prod_{\ell<n}(1-2\hat{c}_\ell^\dagger\hat{c}_\ell)$ is required to match the spin commutation and fermion anti-commutation relations. The x and y bonds on the honeycomb lattice are nearest-neighbour bonds along the string. Although the coupling terms along these bonds involve spin components $\hat{\sigma}^x$ and $\hat{\sigma}^y$, the property $\hat{D}_n\hat{D}_{n+1} = 1-2\hat{c}_n^\dagger\hat{c}_n$ ensures that the fermionized Hamiltonian remains local in the sense that no terms beyond nearest-neighbor coupling arise. The z bonds connect spins that are not nearest neighbors along the snake string. As a result, any Hamiltonian that involves couplings between the x or y spin components along the z bonds would become non-local. This however is not the case for the Kitaev Ising model

(6.1).

In terms of Majorana fermions $\hat{\psi}_A(\mathbf{r}) = i[\hat{c}_A^\dagger(\mathbf{r}) - \hat{c}_A(\mathbf{r})]$, $\hat{\eta}_A(\mathbf{r}) = \hat{c}_A^\dagger(\mathbf{r}) + \hat{c}_A(\mathbf{r})$, $\hat{\psi}_B(\mathbf{r}) = \hat{c}_B^\dagger(\mathbf{r}) + \hat{c}_B(\mathbf{r})$ and $\hat{\eta}_B(\mathbf{r}) = i[\hat{c}_B^\dagger(\mathbf{r}) - \hat{c}_B(\mathbf{r})]$ the Hamiltonian is

$$\begin{aligned}\hat{\mathscr{H}} &= -iK\sum_{\mathbf{r}}\sum_{i=1,2}\hat{\psi}_A(\mathbf{r})\hat{\psi}_B(\mathbf{r}+\mathbf{a}_i) \\ &\quad +J\sum_{\mathbf{r}}\sum_{i=1,2}[i\hat{\psi}_A(\mathbf{r})\hat{\psi}_B(\mathbf{r}+\mathbf{a}_i)]\,[i\hat{\eta}_A(\mathbf{r})\hat{\eta}_B(\mathbf{r}+\mathbf{a}_i)] \\ &\quad +(K_z+J)\sum_{\mathbf{r}}[i\hat{\psi}_A(\mathbf{r})\hat{\psi}_B(\mathbf{r})]\,[i\hat{\eta}_A(\mathbf{r})\hat{\eta}_B(\mathbf{r})], \qquad (6.2)\end{aligned}$$

where $\{\hat{\psi}_\alpha(\mathbf{r}), \hat{\psi}_{\alpha'}(\mathbf{r}')\} = \{\hat{\eta}_\alpha(\mathbf{r}), \hat{\eta}_{\alpha'}(\mathbf{r}')\} = 2\delta_{\alpha,\alpha'}\delta_{\mathbf{r},\mathbf{r}'}$ and $\{\hat{\psi}_\alpha(\mathbf{r}), \hat{\eta}_{\alpha'}(\mathbf{r}')\} = 0$.

Even for the pure Kitaev model, $J = 0$, this seems to be an interacting problem. However, in this case the $\hat{\eta}$ Majorana fermions only live on isolated z bonds and the bond operators $\hat{B}_z(\mathbf{r}) = i\hat{\eta}_A(\mathbf{r})\hat{\eta}_B(\mathbf{r})$, which have eigenvalues ± 1, commute with the Hamiltonian, $[\hat{B}_z(\mathbf{r}), \hat{\mathscr{H}}] = 0$. In the absence of flux excitations, we can replace all operators $\hat{B}_z(\mathbf{r})$ with the negative eigenvalue. This results in a non-interacting Hamiltonian for the $\hat{\psi}$ Majorana fermions with energy dispersion $\varepsilon_{\psi,\pm}(\mathbf{k}) = \pm|K_z + K(e^{i\mathbf{k}\cdot\mathbf{a}_1} + e^{i\mathbf{k}\cdot\mathbf{a}_2})|$. For $K_z/K < 2$ we obtain gapless excitations with a pair of Dirac points. These merge at $K_z/K = 2$ into a semi-Dirac point at $\mathbf{K}_s = (0, \frac{2\pi}{3})$. For $K_z/K > 2$ the spectrum is gapped.

For non-zero J the $\hat{\eta}$ Majorana fermions acquire dynamics and $[\hat{B}_z(\mathbf{r}), \hat{\mathscr{H}}] \neq 0$. In this case, the model is no longer exactly solvable. An approximate phase diagram of the Kitaev-Ising model can be obtained using mean-field theory [162], where the bond expectation values $A_\gamma = \langle i\hat{\psi}_A(\mathbf{r})\hat{\psi}_B(\mathbf{r}+\boldsymbol{\delta}_\gamma)\rangle$ and $B_\gamma = \langle i\hat{\eta}_A(\mathbf{r})\hat{\eta}_B(\mathbf{r}+\boldsymbol{\delta}_\gamma)\rangle$ ($\boldsymbol{\delta}_x = \mathbf{a}_1$, $\boldsymbol{\delta}_y = \mathbf{a}_2$, $\boldsymbol{\delta}_z = \mathbf{0}$), as well as the staggered magnetization $m = \langle i\hat{\psi}_A(\mathbf{r})\hat{\eta}_A(\mathbf{r})\rangle = -\langle i\hat{\psi}_B(\mathbf{r})\hat{\eta}_B(\mathbf{r})\rangle$ are determined self-consistently. This results in the phase diagram shown in Fig. 6.2.

As expected, a relatively small Ising exchange J leads to a first-order transition to an antiferromagnetic state. Importantly, a continuous topological phase transition between a gapless and a gapped Kitaev QSL still occurs for sufficiently small J. The insets of Fig. 6.2 show the evolution of the mean-field dispersion across this transition. While the gapless $\hat{\psi}$ Majorana modes behave in the same way as for the

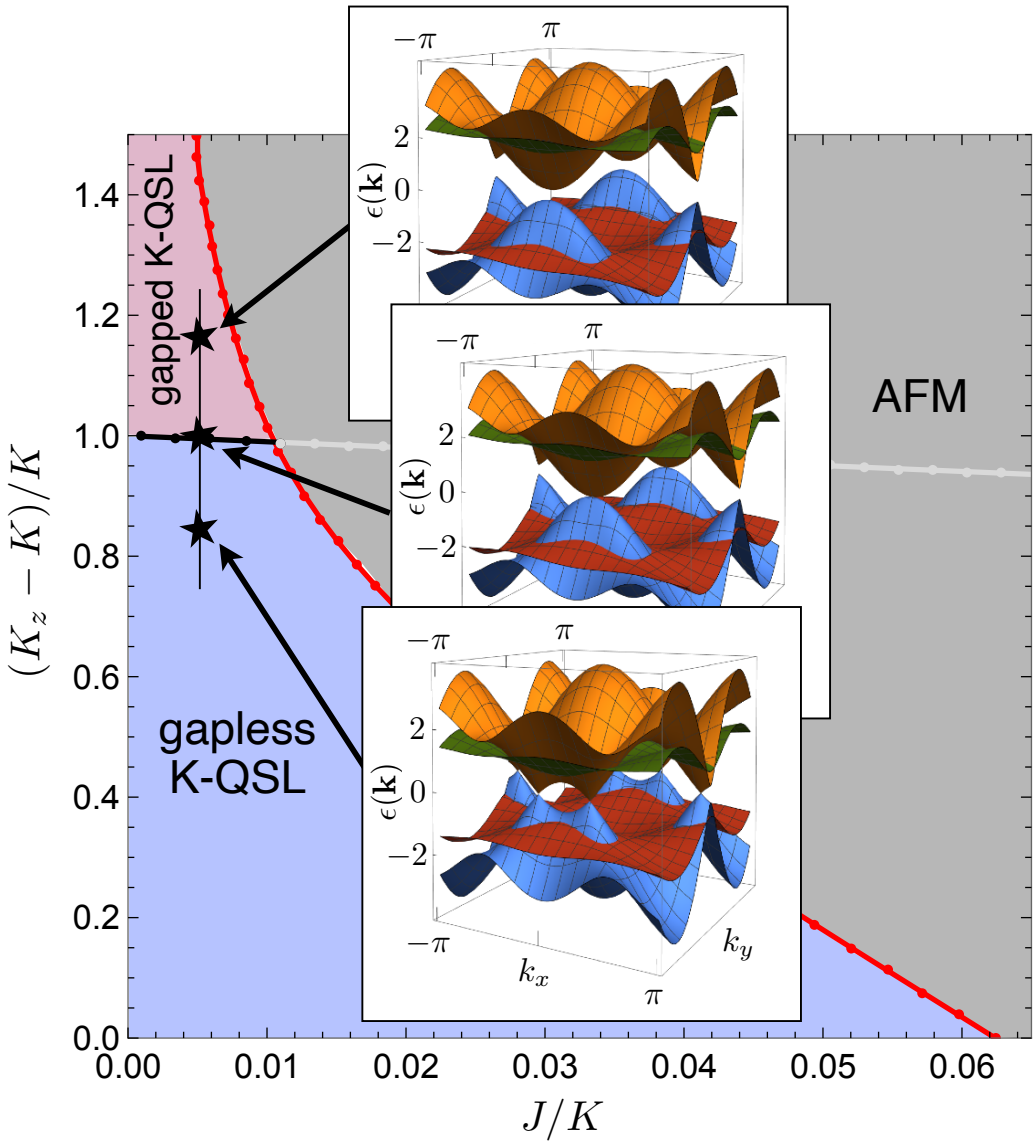

Figure 6.2: Mean-field phase diagram as a function of the anisotropy $(K_z - K)/K$ and the Ising exchange J/K. The evolution of the Majorana fermion spectrum across the topological phase transition between the gapless and gapped quantum spin liquid phases is shown in the insets.

pure anisotropic Kitaev model, a key difference is that the gapped $\hat{\eta}$ modes become dispersive.

In order to understand the nature of the topological quantum phase transition, it is essential to include fluctuations beyond mean-field theory, arising from the interaction vertex. We recast the problem using a Grassmann path integral with

action

$$\begin{aligned} S &= \int_k \boldsymbol{\psi}_k^\dagger \begin{pmatrix} -ik_0 & -i\xi_{\mathbf{k}}^* \\ i\xi_{\mathbf{k}} & -ik_0 \end{pmatrix} \boldsymbol{\psi}_k + \int_k \boldsymbol{\eta}_k^\dagger \begin{pmatrix} -ik_0 & -i\lambda_{\mathbf{k}}^* \\ i\lambda_{\mathbf{k}} & -ik_0 \end{pmatrix} \boldsymbol{\eta}_k \\ &\quad + \sum_\gamma g_\gamma \sum_{\mathbf{r}} \int_\tau [i\psi_A(\mathbf{r},\tau)\psi_B(\mathbf{r}+\boldsymbol{\delta}_\gamma,\tau)] \\ &\quad \times [i\eta_A(\mathbf{r},\tau)\eta_B(\mathbf{r}+\boldsymbol{\delta}_\gamma,\tau)], \end{aligned} \tag{6.3}$$

where τ denotes imaginary time, $\mathbf{k}$ the two-dimensional momentum, k_0 frequency, and $k = (k_0, \mathbf{k})$. The complex functions $\xi_{\mathbf{k}} = \sum_\gamma a_\gamma e^{i\mathbf{k}\boldsymbol{\delta}_\gamma}$ and $\lambda_{\mathbf{k}} = \sum_\gamma b_\gamma e^{i\mathbf{k}\boldsymbol{\delta}_\gamma}$ are linked to the mean-field dispersions, $\varepsilon_{\psi,\pm}(\mathbf{k}) = \pm|\xi_{\mathbf{k}}|$ and $\varepsilon_{\eta,\pm}(\mathbf{k}) = \pm|\lambda_{\mathbf{k}}|$, respectively. We have written the interactions as g_γ, for brevity. Because of symmetry $g_x = g_y$, $a_x = a_y$ and $b_x = b_y$. Note that $b_z/b_{x,y} > 2$ since the η Majorana fermion bands are gapped.

As the next step, we integrate out the gapped Majorana modes η, which results in an effective interaction for the gapless ψ Majorana fermions,

$$\begin{aligned} S_{\text{int}} &= \sum_{\alpha\beta\gamma} \rho_{\alpha\beta}^\gamma \sum_{\mathbf{r}} \int_\tau [i\psi_A(\mathbf{r}-\boldsymbol{\delta}_\alpha+\boldsymbol{\delta}_\gamma,\tau)\psi_B(\mathbf{r}+\boldsymbol{\delta}_\gamma,\tau)] \\ &\quad \times [i\psi_A(\mathbf{r},\tau)\psi_B(\mathbf{r}+\boldsymbol{\delta}_\beta,\tau)], \end{aligned} \tag{6.4}$$

$$\rho_{\alpha\beta}^\gamma = \frac{1}{2}\sum_\varepsilon g_\alpha g_\beta b_\gamma b_\varepsilon \int_q \frac{e^{-i\mathbf{q}(\boldsymbol{\delta}_\alpha+\boldsymbol{\delta}_\beta-\boldsymbol{\delta}_\gamma-\boldsymbol{\delta}_\varepsilon)}}{(q_0^2+|\lambda_{\mathbf{q}}|^2)^2}, \tag{6.5}$$

with $\alpha \neq \gamma$ and $\beta \neq \gamma$. The different types of interactions $\rho_{\alpha\beta}^\gamma$ are visualized in Fig. 6.3 and correspond to the coupling of bond operators $\hat{A}_\alpha$ and $\hat{A}_\beta$ linked through a γ bond.

It is important to stress that for $J = 0$ we obtain $g_x = g_y = 0$ and $b_x = b_y = 0$ since interactions are restricted to the z bonds and the η bands are dispersionless. In this case all interactions $\rho_{\alpha\beta}^\gamma$ are equal to zero and we obtain a theory of non-interaction ψ Majorana fermions.

As the final step, we perform a Hubbard-Stratonovich decoupling of the interactions. For reasons that will become clear later, we only need to work out the coupling between the dynamical order-parameter field and the semi-Dirac

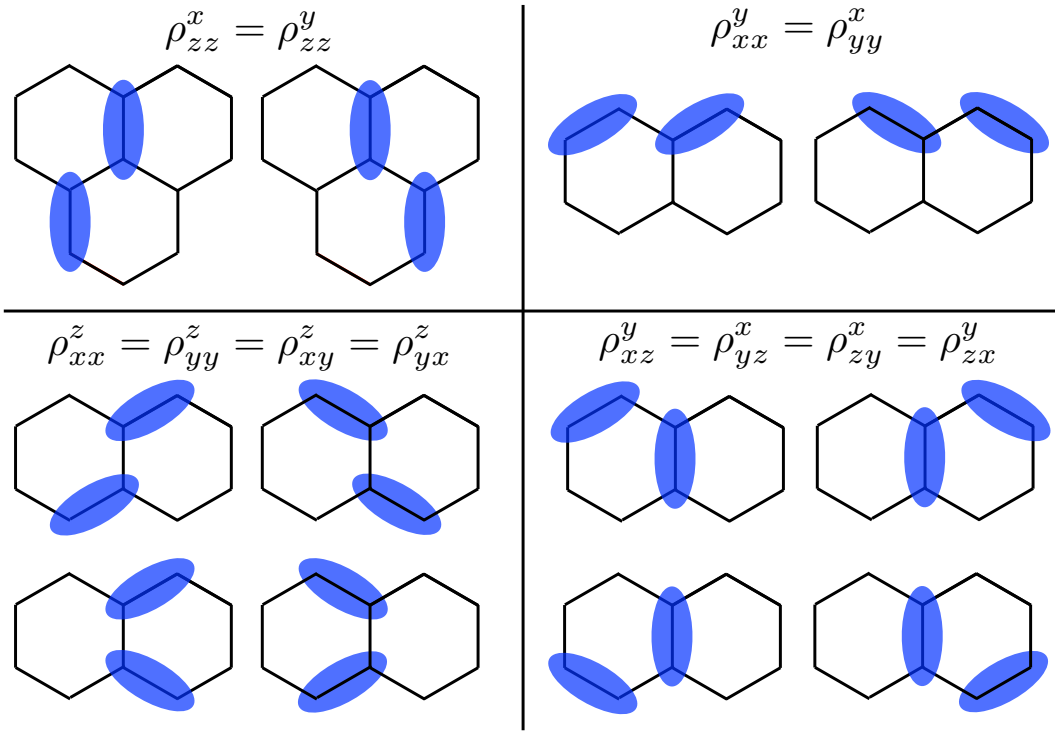

Figure 6.3: Illustration of the interaction terms between the bond-operators $\hat{A}_{ij} = i\hat{\psi}_i\hat{\psi}_j$ of the gapless Majorana modes $\hat{\psi}$, obtained after integrating the gapped modes $\hat{\eta}$.

Majorana fermions. The form of the coupling can be obtained more easily from a mean-field decoupling with $\phi_\gamma(\mathbf{r}) = \langle i\hat{\psi}_A(\mathbf{r})\hat{\psi}_B(\mathbf{r}+\boldsymbol{\delta}_\gamma)\rangle$. This results in $\sum_{\mathbf{r},\gamma}\Omega_\gamma(\mathbf{r})[i\hat{\psi}_A(\mathbf{r})\hat{\psi}_B(\mathbf{r}+\boldsymbol{\delta}_\gamma)]$, where the fields $\Omega_\gamma(\mathbf{r})$ are certain combinations of $\phi_\gamma(\mathbf{r})$, e.g. $\Omega_z(\mathbf{r}) = 2(\rho^x_{zz}+\rho^y_{zz})\phi_z(\mathbf{r}) + 2\rho^y_{xz}\phi_x(\mathbf{r}) + 2\rho^x_{yz}\phi_y(\mathbf{r})$. After Fourier transform and expansion around the semi-Dirac point $\mathbf{K}_s = (0, \frac{2\pi}{3})$ we obtain the Yukawa coupling term of the low energy field theory,

$$S_Y[\phi, \bar{\boldsymbol{\psi}}, \boldsymbol{\psi}] = \frac{g}{\sqrt{N}}\int_{k,q}\phi(q)\bar{\boldsymbol{\psi}}(k)\boldsymbol{\sigma}_y\boldsymbol{\psi}(k+q), \tag{6.6}$$

where $\boldsymbol{\sigma}_y$ denotes a Pauli matrix in sublattice space and the Ising fluctuation field is given by $\frac{g}{\sqrt{N}}\phi(q) = \Omega_z(q) - \Omega_x(q) - \Omega_y(q)$. Note that we generalized to N flavours of semi-Dirac fermions and scaled the coupling accordingly. Expanding the quadratic part $S_0[\bar{\boldsymbol{\psi}}, \boldsymbol{\psi}]$ of the action (6.3) around $\mathbf{K}_s$ we obtain

$$S_0[\bar{\boldsymbol{\psi}}, \boldsymbol{\psi}] = \int_k \bar{\boldsymbol{\psi}}_k \left[-ik_0 + k_L\boldsymbol{\sigma}_x + \left(k_Q^2 + \Delta\right)\boldsymbol{\sigma}_y\right]\boldsymbol{\psi}_k, \tag{6.7}$$

where $k_L = 3ak_y$ and $k_Q = \frac{\sqrt{3a}}{2}q_x$ ($a = a_x = a_y$) are the rescaled momenta along the linear and quadratic directions, respectively and $\Delta = a_z - 2a$ is the tuning parameter of the topological phase transition, where $\Delta = 0$ at the critical point. As one might have anticipated, the dynamical bosonic fluctuation field $\phi(q)$ in S_Y (6.6) couples in the same way as the static tuning parameter Δ in S_0 (6.7). The bosonic action $S[\phi]$ that is generated under perturbative RG is of the conventional Ginzburg-Landau form. However, this neglects the non-analytic bosonic self-energy correction $\Pi(q)$ due to the Landau damping of the order parameter fluctuations by gapless fermionic particle-hole fluctuations. Since $\Pi(q)$ dominates over the regular terms in the IR, it is crucial to use the quadratic bosonic action

$$S_0[\phi] = \int_k \phi(-k) G_\phi^{-1}(k) \phi(k) \tag{6.8}$$

with $G_\phi^{-1}(q) = \Pi(q)$ as starting point for subsequent perturbative RG calculation [221]. Using the correct infrared (IR) scaling form of the propagator, the fluctuation corrections under RG are independent of the choice of the ultraviolet (UV) cut-off scheme and therefore universal [222]. The bosonic self energy $\Pi(q) = g^2/N \int_k \mathrm{Tr}\left[G_{\boldsymbol{\psi}}(k)\boldsymbol{\sigma}_y G_{\boldsymbol{\psi}}(k+q)\boldsymbol{\sigma}_y\right]$ is obtained by calculating the fermion polarization bubble digram [Fig. 6.4(a)] over the full range of frequencies and momenta where the non-analyticity arrises from the IR contribution ($k \to 0$). Unfortunately, for the case of semi-Dirac fermions this integral cannot be computed analytically. Following the procedure in Ref. [222], we obtain

$$\Pi(q) = \frac{g^2}{8\pi^2} |q_Q| F\left(\frac{q_0^2 + q_L^2}{q_Q^4}\right), \tag{6.9}$$

where the function $F(u)$ for $u \in [0,\infty)$ is defined through the integral

$$\begin{aligned} F(u) &= \int_0^1 dt \int_{-\infty}^{\infty} dp \\ &\quad \times \left[\frac{(p+1)^4 + p^2(p+1)^2 + (1-t)u}{(p+1)^4 t + p^4(1-t) + t(1+t)u} - 2\right]. \end{aligned} \tag{6.10}$$

The field theory $S_0[\bar{\boldsymbol{\psi}}, \boldsymbol{\psi}] + S_0[\phi] + S_Y[\phi, \bar{\boldsymbol{\psi}}, \boldsymbol{\psi}]$ for the topological phase tran-

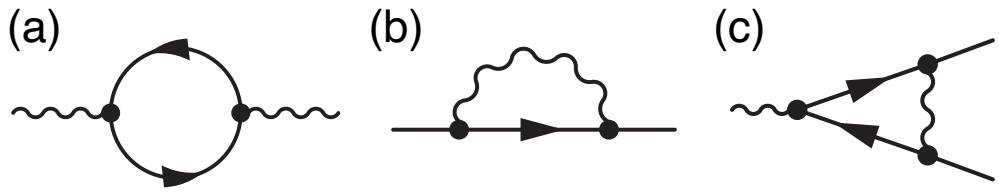

Figure 6.4: (a) Fermionic polarization bubble diagram that gives rise to the non-analytic IR propagator of the bosonic fluctuation field. Panels (b) and (c) show the diagram that contribute to the perturbative renormalization of the free-fermion action and the Yukawa coupling, respectively.

sition between the gapless and gapped Kitaev QSL states is very similar to the GNY theory that describes the quantum criticality of semi-Dirac fermions in 2+1 dimensions due to spontaneous symmetry breaking [222, 223, 224, 225, 159]. A key difference, however, is that for the symmetry-breaking transitions the Yukawa coupling is through the $\boldsymbol{\sigma}_z$ channel, which upon condensation of the order parameter results in the opening of a conventional mass gap in the fermion spectrum. The different form of the Yukawa coupling (6.6) through $\boldsymbol{\sigma}_y$ changes the form of the IR propagator $G_\phi(q)$ and of perturbative RG diagrams, resulting in distinct critical behavior.

6.3 Renormalisation Group Analysis

To set up the RG calculation, we consider shells in frequency-momentum space, $\varepsilon^2 = k_0^2 + k_L^2 + k_Q^4$ with cut-off $\varepsilon \leq \Lambda$ and integrate out modes from the infinitesimal shell $\Lambda e^{-d\ell} \leq \varepsilon \leq \Lambda$, followed by a rescaling $k_0 \to k_0 e^{-d\ell}$, $k_L \to k_L e^{-d\ell}$ and $k_Q \to k_Q e^{-z_Q d\ell}$ to the old cut-off. Note that at tree-level $z_Q = 1/2$. We further rescale the fields as $\psi \to \psi e^{-(\Delta_\psi/2)d\ell}$ and $\phi \to \phi e^{-(\Delta_\phi/2)d\ell}$.

The fermionic self-energy correction $\boldsymbol{\Sigma}(k)d\ell = -g^2/N \int_q^> G_\phi(q)\boldsymbol{\sigma}_y G_{\boldsymbol{\psi}}(k+q)\boldsymbol{\sigma}_y$, which corresponds to the diagram in Fig. 6.4(b), is of the same form as the original kernel in $S_0[\bar{\boldsymbol{\psi}}, \boldsymbol{\psi}]$,

$$\boldsymbol{\Sigma}(k)d\ell = \left[\Sigma_0(-ik_0\boldsymbol{\sigma}_0 + k_L\boldsymbol{\sigma}_x) + (\Sigma_Q k_y^2 + \Sigma_\Delta \Delta)\boldsymbol{\sigma}_y\right] d\ell, \tag{6.11}$$

where the coefficients are evaluated in terms of generalized spherical coordinates $k_0 = \varepsilon \sin\theta\cos\phi$, $k_L = \varepsilon \sin\theta \sin\phi$ and $k_Q^2 = \varepsilon\cos\theta$ ($\theta \in [0, \pi/2]$, $\phi \in [0, 2\pi]$,

z_Q	ν_Δ^{-1}	$\eta_{\boldsymbol{\psi}}$	η_ϕ
$\frac{1}{2}-\frac{0.0387}{N}$	$1-\frac{0.2912}{N}$	$\frac{0.1093}{N}$	$-\frac{0.6093}{N}$

Table 6.1: Critical exponents for the topological phase transition between the gapless and gapped Kitaev QSL phases in (2+1) dimensions, calculated to one-loop order.

$\varepsilon \in [\Lambda e^{-d\ell}, \Lambda]$) with Jacobian determinant $J(\varepsilon,\theta,\phi) = \frac{1}{2}\varepsilon^{3/2}\sin\theta/\sqrt{\cos\theta}$. The remaining integrals over $u = \tan^2\theta$ are computed numerically. The detailed calculation can be found in appendix A, here we only list the results:

$$\Sigma_0 = \frac{1}{2N}\int_0^\infty du \frac{1}{(u+1)^2 F(u)} \approx \frac{0.1511}{N}, \tag{6.12}$$

$$\Sigma_Q = -\frac{1}{2N}\int_0^\infty du \frac{u^2-12u+3}{(u+1)^3 F(u)} \approx \frac{0.0163}{N}, \tag{6.13}$$

$$\Sigma_\Delta = -\frac{1}{2N}\int_0^\infty du \frac{u-1}{(u+1)^2 F(u)} \approx -\frac{0.4312}{N}. \tag{6.14}$$

From the diagram shown in Fig. 6.4(c) be obtain the correction $\Omega\boldsymbol{\sigma}_y d\ell = (g^2/N)\int_q^> G_\phi(q)\boldsymbol{\sigma}_y G_{\boldsymbol{\psi}}(q)\boldsymbol{\sigma}_y G_{\boldsymbol{\psi}}(q)\boldsymbol{\sigma}_y$ to the Yukawa coupling matrix, where the shell integral gives $\Omega = \Sigma_\Delta$.

From the perturbative RG corrections we can extract critical exponents. Demanding that the fermion propagator at the transition ($\Delta = 0$) remains scale invariant, we obtain the scaling exponent $z_Q = \frac{1}{2} + \frac{1}{2}\Sigma_Q - \frac{1}{2}\Sigma_0$ of the quadratic momentum direction k_Q relative to the linear directions k_0 and k_L, and the scaling dimension $\Delta_{\boldsymbol{\psi}} = -\frac{7}{2} + \frac{3}{2}\Sigma_0 - \frac{1}{2}\Sigma_Q = -\frac{7}{2} + \eta_{\boldsymbol{\psi}}$ of the Majorana fermion field, where $\eta_{\boldsymbol{\psi}}$ denotes the anomalous dimension. The correlation length exponent ν_Δ of the topological phase transition is defined through the RG equation for Δ, $\partial_\ell\Delta = (1-\Sigma_0+\Sigma_\Delta)\Delta = \nu_\Delta^{-1}\Delta$. Finally, imposing that the Yukawa coupling g remains scale invariant, we obtain the scaling dimension of the bosonic fluctuation field, $\Delta_\phi = -3 + \eta_\phi$ with $\eta_\phi = 2\Omega - \Sigma_0 - \Sigma_Q$.

The resulting numerical values of the critical exponents are summarized in Table 6.1. For completeness, let us also investigate the relevance of the ϕ^4 vertex at the topological phase transition. At tree-level, the scaling dimension of the coefficient is equal to $[\lambda] = -3(2+z_Q) - 2\Delta_\phi = -3/2$, demonstrating that the vertex is

strongly irrelevant and hence can be neglected.

6.4 Discussion and Conclusion

To summarize, we have derived the effective field theory for the topological quantum phase transition between the gapless and gapped Kitaev QSL phases. For the pure, exactly solvable Kitaev model the problem reduces to a free-fermion field theory. Away from the exactly solvable point, the field theory is of the GNY type and describes the coupling between an Ising fluctuation field to the gapless semi-Dirac Majorana fermion modes. We determined the critical exponents from an RG analysis and demonstrated that the universality of the topological phase transition is different to that describing symmetry-breaking phase transitions of semi-Dirac fermions.

The exponent ν_Δ is linked to the opening of the energy gap in the Majorana fermion spectrum, $\Delta \sim (\delta - \delta_c)^{\nu_\Delta}$, as well as to the separation of the Dirac points on the gapless QSL side, $(\delta k) \sim (\delta_c - \delta)^{\nu_\Delta/2}$. It could in principle be determined experimentally by measuring the evolution of the magnetic excitation continuum across the topological phase transition. However, it remains a challenge to realize the topological phase transition in experiment since uniaxial strain would not only affect the anisotropy of the Kitaev couplings but also distort the lattice, resulting in an increase of other magnetic exchange couplings.

The Kiteav QSL is a novel and exotic state of matter due to its long range entanglement and the fractionalization of spin degrees of freedom into Majorana fermions. Our work shows that the quantum criticality associated with a topological phase transition adds another layer of complexity. At the transition the emergent Majorana fermions acquire an anomalous dimension, indicative of a breakdown of the quasiparticle picture and the formation of a Majorana non-Fermi liquid state.

Chapter 7

Closing Remarks

We now conclude the thesis by summarising the work discussed in this thesis. Since detailed discussions have already been given at the end of each chapter, here we only focus on the general aspects and their connections. Then the conclusion will be followed by a brief outlook to point out potential future directions.

7.1 Conclusion

In this thesis, the effect of quantum fluctuations of fermions on phase transitions in different scenarios is studied. We have shown that the low energy fermion scattering near the Fermi surface can (1) complicate the interplay between Kondo exchange anisotropy and single-ion spin anisotropy, which may lead to the hard-direction ordering in such systems, or (2) challenge the stability of Néel quantum critical point so that in the presence of Dirac fermions the Néel fixed point is only stable at a certain parameter range; Even more interestingly, (3) the fluctuation of emergent Majorana fermions in Kitaev quantum spin liquids can also give rise to similar physics as such in graphene, which provides an ideal angle to understand the properties and phase transitions of QSL in the better-understood fermion language. In this spirit, we showed that the topological phase transition between the gapless and gapped QSL states induced by Kitaev anisotropy and extra magnetic interactions can be described by a Gross-Neveu-Yukawa theory, corresponding to a new universality class.

In Chapter 3, an anisotropic Kondo model was utilised to explain the magnetic

hard-direction ordering observed in some Kondo lattice materials. A perturbative RG calculation showed that the RG flow of the magnitude of single-ion anisotropy may change sign at some length scale, indicating the previously hard direction becomes the new easy one. This is a generic effect due to the interplay between two types of anisotropies through fermionic fluctuations near the Fermi surface. The generality of the mechanism is further supported by a numerical RG calculation and an analytic solution at the extremely narrow bandwidth limit, where crossings also exist in the susceptibilities. This suggests that the mechanism works even away from the perturbative regime. Though this is a single impurity result, one can expect the same mechanism to also work in a Kondo lattice following the reasoning that the RKKY effect is a second-order effect of the Kondo coupling and should enhance the difference in the renormalised anisotropies so that the magnetic susceptibility diverges first along the 'hard-direction', giving rise to hard-direction magnetic order. Though there's no criticality in the calculation, the non-perturbative fermion scattering by the impurity near the Fermi surface can already show that exotic behaviours can arise in the presence of fermions.

In Chapter 4, we examined the effect of particle-hole fluctuation of Dirac fermions to a quantum critical point, namely the Néel quantum critical point in 2D. The Dirac fermions interact with the local moments through a Kondo coupling. Regardless of the simple point-like Fermi surface, in 2D the zero energy fluctuations near the Fermi surface can damp the order parameter field propagator in a similar manner as how fermionic fluctuations screen the long-range Coulomb interaction in 3D. The damping of the order parameter field is also a non-perturbative effect that can be treated by an RPA resummation of fermion polarisation bubble diagrams to infinite order. Consequently one gets a non-analytic contribution to the order parameter field self-energy that dorminates in the IR. In this spirit, a GNY model in which the bosonic fields are described by an NLσM is used to study the Néel criticality. Surprisingly, though of lower order in momenta, the Landau damping propagator γ is irrelevant near the Néel critical point, while the Kondo coupling λ is relevant. The RG flow is dependent on the number of Dirac fermion flavors

N_f. In the physical case $N_f = 4$, representing the Dirac fermions on a honeycomb lattice, although no new fixed point is present, the RG flow in a certain region is extremely slow, indicating the stability of the N'eel fixed point against the Kondo fluctuation of the Dirac fermions. This is because the $N_f = 4$ is the critical case. For $N_f < 4$, a new multi-critical point emerges.

In Chapter 5, we switched to the exactly solvable Kitaev honeycomb model, where the spin interactions are bond-orientally anisotropic. It is known that in such a model the ground state is a Z_2 QSL, and the spins fractionalise into Z_2 gauge fields and Majorana fermions with Dirac dispersion. In the presence of an additional antiferromagnetic Ising interaction term, the model is no longer exactly solvable. At the large Ising limit, the ground state is known to be antiferromagnetic. A mean-field decoupling with both Kitaev's Majorana fermion representation and Jordan-Wigner fermions representation is enacted to map out the phase diagram. The two representations result in the same topological phase boundary but predict the magnetic phase transition at different coupling strengths. This is probably due to the different treatments in the gauge fields at the mean-field level. We also obtain the finite temperature phase diagram of the magnetic phase transition along with the specific heat, which at low temperatures shows the signature of Dirac fermions, and crossover to the full spin half behavior when the temperature reaches the size of the flux gap.

From the results in Chapter 5, we saw that the topological phase transition between the gapped and gapless QSL mainly concerns the mobile Majorana fermions only, as the Lagrange multiplier related to the flux excitations stays zero throughout the transition. The phase transition therefore resembles the semimetal-insulator transition in real electron systems like graphene. With this in mind, we derived the low-energy effective field theory of the topological phase transition from the microscopic Kitaev-Ising model. For the pure Kitaev model, the low-energy theory is a free Majorana fermion theory, indicating the exact solvability of the model. With any additional magnetic interactions, the theory becomes interactive, and hence can be studied with the GNY language. Due to the distinct mathematical properties of the Majorana fermions, the resulting critical exponents are different from the ones

derived from complex Dirac fermions, corresponding to a new GNY universality class. This could in principle be confirmed by experimental measurements.

As a general conclusion, we applied the field-theoretical technique of perturbative renormalisation group associated with some numerical methods to study the phases and phase transitions in Kondo systems and Kitaev quantum spin liquids. The transitions are mainly driven by the quantum fluctuations of electrons near the Fermi surface. We focused on the situation of Dirac fermions where the Fermi surface is just a single point. The low-energy description of the associated quantum phase transitions in this case can be described by the Gross-Neveu-Yukawa theory. The results elucidated the importance of going beyond the Landau-Ginzburg paradigm and considering the order parameter screening in such gapless fermionic systems, and provided hints to a plethora of such fermion-induced quantum criticality.

7.2 Outlook

First, the results in Chapter 3 are based on a single-impurity calculation, therefore no magnetic ordering along the hard direction can be observed after the crossing. We have reasoned in Chapter 3 that the RKKY effect should help stabilise the magnetic order along the anisotropy-favored direction, and this could in principle be observed in a Kondo lattice model. The key is that the susceptibilities first cross in the Kondo regime, after which the RKKY effect takes over the control and the susceptibility diverges along the new 'easy direction'. Such a Doniach diagram can be observed at the mean-field level [226]. However, the Kondo hybridization is considered an order parameter in the mean-field theory. Though still possible, it is in general hard for the magnetic phase to coexist with Kondo hybridization [227, 228]. On the other hand, the real Kondo materials that exhibit the hard direction ordering usually contain transition metals like Hf and Ce, meaning the systems have strong spin-orbit coupling. In such cases, the only good quantum number is the total angular momentum, and the systems are better described by a Coqblin-Schieffer model [229]. It would be interesting to see if the mechanism works in such a model.

The calculation in Chapter 4 can be extended to study the effect of Dirac fermions on other more exotic fermion-induced quantum criticalities, such as the deconfined quantum criticality in the presence of Dirac fermions. It is suggested that the Heisenberg model with next-nearest neighbor interactions on a honeycomb lattice can have an RVB ground state. Therefore by tuning the strength of the next-nearest neighbor interaction, one can tune the system through a phase transition between an antiferromagnet and an RVB solid. The corresponding low-energy theory is described by a non-linear σ model associated with an emergent gauge field. On top of it, one can add another layer of complexity by Kondo coupling the spins to Dirac electrons, which will then lead to a theory of fermions, bosons and gauge fields. If it's a $U(1)$ gauge field, then the field theory is analogous to the quantum electrodynamics in high energy theory, but in two spatial dimensions (QED_3). The combination of deconfined quantum criticality and fermion-induced criticality can provide new insights into our understanding of the theory of phase transitions beyond the Landau-Ginzburg paradigm.

The Kondo coupling can also be introduced to connect the Kitaev QSLs and complex Dirac fermions, which then form the so-called fractionalised Fermi-liquid where the Luttinger theorem breaks down. It is argued in [230] that at mean-field level, the Majorana fermions can become the glue of the pairing between complex Dirac fermions to form a p-wave superconductor. In such cases, the low-energy theory again will be described by fermions, bosons and emergent gauge fields. Additionally, recent numerics show evidence that the Kitaev QSL can go through a phase transition between a Z_2 QSL and a $U(1)$ QSL [231]. If this is the case, the criticality will be similar to the Z_2 to $U(1)$ transition in Dirac QSLs with fractionalised spinon excitations [232, 233] due to the nature of Majorana fermions, and thus worth investigating.

Apart from the specific directions that may be interesting for future research, we should bear in mind that the Dirac fermion-induced quantum criticality is just a simple example of the family of quantum phase transitions in gapless systems. The problem will be both more complicated and interesting if taking into account the

shape of the Fermi surface. A natural step further is to consider the quantum phase transitions in nodal-line semimetals where the Fermi surface is a closed contour, or even in real metals with a full Fermi surface. Besides, we have already seen that the Dirac fermion-induced criticality in general leads to some non-Fermi liquid behavior. Moving to semimetallic and metallic systems with a more complicated Fermi surface will shed light on the general understanding of non-Fermi liquid theory.

Appendix A

RG analysis of the Interacting Majorana fermion theory

A.1 Landau-damped Bosonic IR propagator

The fermion polarization bubble diagram is regularized by subtracting the $q=0$ contribution: $\Pi(q) \to \Pi(q) - \Pi(0)$,

$$\begin{aligned}\Pi(q) &= \frac{g^2}{N}\int_k \mathrm{Tr}\left[G_\psi(k+q)\sigma_y G_\psi(k)\sigma_y - G_\psi(k)\sigma_y G_\psi(k)\sigma_y\right] \\ &= g^2\int_k \left\{\frac{(k_0+q_0)q_0+(k_L+q_L)q_L+(k_Q+q_Q)^2[k_Q^2+(k_Q+q_Q)^2]}{\varepsilon_k^2\varepsilon_{q+k}^2} - 2\frac{k_Q^4}{\varepsilon_k^4}\right\},\end{aligned} \tag{A.1}$$

where we have used $G_\psi(k) = (ik_0 + k_L\sigma_x + k_Q^2\sigma_y)/\varepsilon_k^2$, and $\varepsilon_k^2 = k_0^2 + k_L^2 + k_Q^4$. Taking the trace results in an N factor that cancels with the $1/N$ in the prefactor. The integral in Eq. (A.1) can be rendered radially symmetric in k_0 and k_L directions by utilizing the Feynman parametrization:

$$\frac{1}{a^n b^m} = \frac{\Gamma(n+m)}{\Gamma(n)\Gamma(m)}\int_0^1 dt \frac{t^{n-1}(1-t)^{m-1}}{[ta+(1-t)b]^{n+m}}, \tag{A.2}$$

where we have chosen $a = \varepsilon_{k+q}^2,\ b = \varepsilon_k^2,\ n = m = 1$. Shifting the variables as $(k_0, k_L) \to (k_0, k_L) - t(q_0, q_L)$ and converting to the radial coordinate $y^2 = k_0^2 + k_L^2$, Eq. (A.1) becomes

$$\Pi(q) = \frac{g^2}{(2\pi)^2}\int_{-\infty}^{\infty} dk_Q \int_0^{\infty} dy\, y \left\{ \int_0^1 dt \frac{(1-t)(q_0^2+q_L^2)+(k_Q+q_Q)^2[k_Q^2+(k_Q+q_Q)^2]}{[y^2+t(1-t)(q_0^2+q_L^2)+(1-t)k_Q^4+t(k_Q+q_Q)^4]^2} - 2\frac{k_Q^4}{(y^2+k_Q^4)^2} \right\}$$
$$= \frac{g^2}{8\pi^2}\int_{-\infty}^{\infty} dk_Q \left\{ \int_0^1 dt \frac{(1-t)(q_0^2+q_L^2)+(k_Q+q_Q)^2[k_Q^2+(k_Q+q_Q)^2]}{t(1-t)(q_0^2+q_L^2)+(1-t)k_Q^4+t(k_Q+q_Q)^4} - 2 \right\}$$
$$= \frac{g^2}{8\pi^2}|q_Q|\int_{-\infty}^{\infty} dp \left\{ \int_0^1 dt \frac{(1-t)\frac{q_0^2+q_L^2}{q_Q^4}+(1+p)^4+(1+p^2)p^2}{t(1-t)\frac{q_0^2+q_L^2}{q_Q^4}+(1-t)p^4+t(1+p)^4} - 2 \right\}$$
$$= \frac{g^2}{8\pi^2}|q_Q| F(\tfrac{q_0^2+q_L^2}{q_Q^4}).$$

In the second line we have used the radial integral identity in D dimension:

$$\int_0^{\infty} dy\, \frac{y^{D-1+\alpha}}{(y^\beta+M)^n} = \frac{\Gamma(\frac{D+\alpha}{\beta})\Gamma(n-\frac{D+\alpha}{\beta})}{\beta\Gamma(n)M^{n-\frac{D+\alpha}{\beta}}}, \tag{A.3}$$

and in the last line, we have introduced variable substitution $p = k_Q/|q_Q|$.

A.2 Majorana Fermion self-energy correction

It can be shown in general that the RG corrections are cut-off independent [55, 222]. Therefore for simplicity, we use a spherical cut-off scheme and perform the shell integrals over the (2+1)d frequency-momenta shell. We introduce the generalized spherical coordinates ($k_0 = \varepsilon\sin\theta\cos\phi,\ k_L = \varepsilon\sin\theta\sin\phi,\ k_Q^2 = \varepsilon\cos\theta$) with the Jacobian $J(\varepsilon,\theta,\phi) = \frac{1}{2}\varepsilon^{3/2}\sin\theta(\cos\theta)^{-1/2}$, and the shell integrals are calculated in the range $\varepsilon \in [\Lambda e^{-dl},\Lambda],\ \theta\in[0,\pi/2],\ \phi\in[0,2\pi]$.

The fermion self-energy correction at one-loop level has the form

$$\begin{aligned}
\boldsymbol{\Sigma}(k)d\ell &= -\frac{g^2}{N}\int_q^{>} G_\phi(q)\boldsymbol{\sigma}_y G_{\boldsymbol{\psi}}(k+q)\boldsymbol{\sigma}_y \\
&= -\frac{8\pi^2}{N}\int_q^{>}|q_Q|^{-1}\frac{1}{F(\tan^2\theta)}\boldsymbol{\sigma}_y\frac{i(k_0+q_0)\boldsymbol{\sigma}_0+(k_L+q_L)\boldsymbol{\sigma}_x+[(k_Q+q_Q)^2+\Delta]\boldsymbol{\sigma}_y}{\varepsilon(k+q)^2}\boldsymbol{\sigma}_y \\
&= \left[\Sigma_0(-ik_0\boldsymbol{\sigma}_0+k_L\boldsymbol{\sigma}_x)+(\Sigma_Q k_y^2+\Sigma_\Delta\Delta)\boldsymbol{\sigma}_y\right]d\ell.
\end{aligned} \tag{A.4}$$

We expand out the outer-momenta k in the integrand and keep the leading order to get the form of the kernel in $S_0[\psi]$. In the following, we derive the explicit form of

Σ_0, Σ_Q and Σ_Δ separately.

$$\begin{aligned}\Sigma_0 &= -\frac{8\pi^2}{N}\int_q^> |q_Q|^{-1}\frac{1}{F(\tan^2\theta)}\left(\frac{1}{\varepsilon_q^2}-2\frac{q_0^2}{\varepsilon_q^4}\right)\\ &= \frac{1}{N}\int_{\Lambda e^{-dl}}^{\Lambda} d\varepsilon\int_0^{\pi/2} d\theta\ \varepsilon^{-1}\tan\theta\cos^2\theta\frac{1}{F(\tan^2\theta)}\\ &= \frac{1}{2N}d\ell\int_0^\infty du\ \frac{1}{(u+1)^2}\frac{1}{F(u)}.\end{aligned} \tag{A.5}$$

In the last step, we have made the variable substitution $u=\tan^2\theta$, $(u+1)^{-1}du = 2\tan\theta d\theta$. In the same spirit, one can obtain

$$\begin{aligned}\Sigma_Q &= \frac{8\pi^2}{N}\int_q^> |q_Q|^{-1}\frac{1}{F(\tan^2\theta)}\left(\frac{1}{\varepsilon_q^2}-14\frac{q_Q^4}{\varepsilon_q^4}+16\frac{q_Q^8}{\varepsilon_q^6}\right)\\ &= -\frac{1}{N}\int_{\Lambda e^{-dl}}^{\Lambda} d\varepsilon\int_0^{\pi/2} d\theta\varepsilon^{-1}\tan\theta\frac{1}{F(\tan^2\theta)}\left(1-14\cos^2\theta+16\cos^4\theta\right)\\ &= -\frac{1}{2N}d\ell\int_0^\infty du\ \frac{u^2-12u+3}{(u+1)^3}\frac{1}{F(u)},\end{aligned} \tag{A.6}$$

and

$$\begin{aligned}\Sigma_\Delta &= \frac{8\pi^2}{N}\int_q^> |q_Q|^{-1}\frac{1}{F(\tan^2\theta)}\left(\frac{1}{\varepsilon_q^2}-2\frac{q_Q^4}{\varepsilon_q^4}\right)\\ &= -\frac{1}{N}\int_{\Lambda e^{-dl}}^{\Lambda} d\varepsilon\int_0^{\pi/2} d\theta\varepsilon^{-1}\tan\theta\frac{1}{F(\tan^2\theta)}\left(1-2\cos^2\theta\right)\\ &= -\frac{1}{2N}d\ell\int_0^\infty du\ \frac{u-1}{(u+1)^2}\frac{1}{F(u)}.\end{aligned} \tag{A.7}$$

A.3 Correction to Yukawa coupling

At one-loop level, the shell integral that renormalizes the Yukawa coupling has no dependence on outer-momenta:

$$\begin{aligned}
\Omega\boldsymbol{\sigma}_y d\ell &= \frac{g^2}{N}\int_q^> \boldsymbol{\sigma}_y G_\psi(q)\boldsymbol{\sigma}_y G_\psi(q)\boldsymbol{\sigma}_y G_\phi(q) \\
&= -\frac{8\pi^2}{N}\int_q^> |q_Q|^{-1}\,\frac{1}{F(\tan^2\theta)}\,\frac{q_0^2+q_L^2-q_Q^4}{\varepsilon_q^4}\boldsymbol{\sigma}_y \\
&= -\frac{1}{N}d\ell\int_0^{\pi/2} d\theta\ \tan\theta\,\frac{1}{F(\tan^2\theta)}\left(1-2\cos^2\theta\right)\boldsymbol{\sigma}_y \\
&= -\frac{1}{2N}d\ell\int_0^{\infty} du\ \frac{u-1}{(u+1)^2}\,\frac{1}{F(u)}\boldsymbol{\sigma}_y. \qquad \text{(A.8)}
\end{aligned}$$

Bibliography

[1] Philip W. Phillips, Nigel E. Hussey, and Peter Abbamonte. Stranger than metals. *Science*, 377(6602):eabh4273, 2022.

[2] G. R. Stewart. Unconventional superconductivity. *Advances in Physics*, 66(2):75–196, 2017.

[3] Maylis Orio, Dimitrios A. Pantazis, and Frank Neese. Density functional theory. *Photosynthesis Research*, 102(2):443–453, 2009.

[4] Kenneth G. Wilson. The renormalization group: Critical phenomena and the kondo problem. *Rev. Mod. Phys.*, 47:773–840, Oct 1975.

[5] Kenneth G. Wilson. The renormalization group and critical phenomena. *Rev. Mod. Phys.*, 55:583–600, Jul 1983.

[6] Zi-Xiang Li, Yi-Fan Jiang, Shao-Kai Jian, and Hong Yao. Fermion-induced quantum critical points. *Nature Communications*, 8(1):314, 2017.

[7] K. v. Klitzing, G. Dorda, and M. Pepper. New method for high-accuracy determination of the fine-structure constant based on quantized hall resistance. *Phys. Rev. Lett.*, 45:494–497, Aug 1980.

[8] Jun-ichi Wakabayashi and Shinji Kawaji. Hall effect in silicon mos inversion layers under strong magnetic fields. *Journal of the Physical Society of Japan*, 44(6):1839–1849, 2025/02/04 1978.

[9] Xiao-Gang Wen. *Quantum Field Theory of Many-Body Systems: From the Origin of Sound to an Origin of Light and Electrons*. Oxford University Press, 09 2007.

[10] T. Senthil, Ashvin Vishwanath, Leon Balents, Subir Sachdev, and Matthew P. A. Fisher. Deconfined quantum critical points. *Science*, 303(5663):1490–1494, 2004.

[11] Adam Nahum, J. T. Chalker, P. Serna, M. Ortuño, and A. M. Somoza. Deconfined quantum criticality, scaling violations, and classical loop models. *Phys. Rev. X*, 5:041048, Dec 2015.

[12] K. S. Novoselov, A. K. Geim, S. V. Morozov, D. Jiang, M. I. Katsnelson, I. V. Grigorieva, S. V. Dubonos, and A. A. Firsov. Two-dimensional gas of massless dirac fermions in graphene. *Nature*, 438(7065):197–200, 2005.

[13] P. M. Ostrovsky, I. V. Gornyi, and A. D. Mirlin. Theory of anomalous quantum hall effects in graphene. *Phys. Rev. B*, 77:195430, May 2008.

[14] Yuan Cao, Valla Fatemi, Shiang Fang, Kenji Watanabe, Takashi Taniguchi, Efthimios Kaxiras, and Pablo Jarillo-Herrero. Unconventional superconductivity in magic-angle graphene superlattices. *Nature*, 556(7699):43–50, 2018.

[15] P.W. Anderson. Resonating valence bonds: A new kind of insulator? *Materials Research Bulletin*, 8(2):153–160, 1973.

[16] P. W. Anderson. The resonating valence bond state in la¡sub¿2¡/sub¿cuo¡sub¿4¡/sub¿ and superconductivity. *Science*, 235(4793):1196–1198, 1987.

[17] P. Fazekas and P. W. Anderson. On the ground state properties of the anisotropic triangular antiferromagnet. *The Philosophical Magazine: A Journal of Theoretical Experimental and Applied Physics*, 30(2):423–440, 1974.

[18] Shenghan Jiang, Panjin Kim, Jung Hoon Han, and Ying Ran. Competing Spin Liquid Phases in the S=$\frac{1}{2}$ Heisenberg Model on the Kagome Lattice. *SciPost Phys.*, 7:006, 2019.

[19] Yasir Iqbal, Didier Poilblanc, and Federico Becca. Vanishing spin gap in a competing spin-liquid phase in the kagome heisenberg antiferromagnet. *Phys. Rev. B*, 89:020407, Jan 2014.

[20] Th. Jolicoeur, E. Dagotto, E. Gagliano, and S. Bacci. Ground-state properties of the s=1/2 heisenberg antiferromagnet on a triangular lattice. *Phys. Rev. B*, 42:4800–4803, Sep 1990.

[21] L. O. Manuel and H. A. Ceccatto. Magnetic and quantum disordered phases in triangular-lattice heisenberg antiferromagnets. *Phys. Rev. B*, 60:9489–9493, Oct 1999.

[22] Alexei Kitaev. Anyons in an exactly solved model and beyond. *Annals of Physics*, 321(1):2–111, 2006.

[23] Z. Y. Meng, T. C. Lang, S. Wessel, F. F. Assaad, and A. Muramatsu. Quantum spin liquid emerging in two-dimensional correlated dirac fermions. *Nature*, 464(7290):847–851, 2010.

[24] M J P Gingras and P A McClarty. Quantum spin ice: a search for gapless quantum spin liquids in pyrochlore magnets. *Reports on Progress in Physics*, 77(5):056501, may 2014.

[25] Z. Y. Meng, T. C. Lang, S. Wessel, F. F. Assaad, and A. Muramatsu. *Nature*, (7290).

[26] Takashi Imai and Young S. Lee. Do quantum spin liquids exist? *Physics Today*, 69(8):30–36, 08 2016.

[27] Yi Zhou, Kazushi Kanoda, and Tai-Kai Ng. Quantum spin liquid states. *Rev. Mod. Phys.*, 89:025003, Apr 2017.

[28] Lucile Savary and Leon Balents. Quantum spin liquids: a review. *Reports on Progress in Physics*, 80(1):016502, nov 2016.

[29] C. Broholm, R. J. Cava, S. A. Kivelson, D. G. Nocera, M. R. Norman, and T. Senthil. Quantum spin liquids. *Science*, 367(6475):eaay0668, 2020.

[30] M. R. Norman. Colloquium: Herbertsmithite and the search for the quantum spin liquid. *Rev. Mod. Phys.*, 88:041002, Dec 2016.

[31] Jinsheng Wen, Shun-Li Yu, Shiyan Li, Weiqiang Yu, and Jian-Xin Li. Experimental identification of quantum spin liquids. *npj Quantum Materials*, 4(1):12, 2019.

[32] Michael Hermele, T. Senthil, Matthew P. A. Fisher, Patrick A. Lee, Naoto Nagaosa, and Xiao-Gang Wen. Stability of $u(1)$ spin liquids in two dimensions. *Phys. Rev. B*, 70:214437, Dec 2004.

[33] Flavio S. Nogueira and Hagen Kleinert. Quantum electrodynamics in $2+1$ dimensions, confinement, and the stability of $u(1)$ spin liquids. *Phys. Rev. Lett.*, 95:176406, Oct 2005.

[34] Rufus Boyack, Ahmed Rayyan, and Joseph Maciejko. Deconfined criticality in the qed_3 gross-neveu-yukawa model: The $1/n$ expansion revisited. *Phys. Rev. B*, 99:195135, May 2019.

[35] Flavio S. Nogueira and Hagen Kleinert. Compact quantum electrodynamics in $2+1$ dimensions and spinon deconfinement: A renormalization group analysis. *Phys. Rev. B*, 77:045107, Jan 2008.

[36] Igor F. Herbut and Babak H. Seradjeh. Permanent confinement in the compact qed_3 with fermionic matter. *Phys. Rev. Lett.*, 91:171601, Oct 2003.

[37] Éric Dupuis, M. B. Paranjape, and William Witczak-Krempa. Transition from a dirac spin liquid to an antiferromagnet: Monopoles in a qed_3-gross-neveu theory. *Phys. Rev. B*, 100:094443, Sep 2019.

[38] Subir Sachdev. *Quantum Phases of Matter*. Cambridge University Press, 2023.

[39] W.J. de Haas, J. de Boer, and G.J. van dën Berg. The electrical resistance of gold, copper and lead at low temperatures. *Physica*, 1(7):1115–1124, 1934.

[40] Jun Kondo. Resistance minimum in dilute magnetic alloys. *Progress of Theoretical Physics*, 32(1):37–49, 07 1964.

[41] P W Anderson. A poor man's derivation of scaling laws for the kondo problem. *Journal of Physics C: Solid State Physics*, 3(12):2436, 1970.

[42] Alexander Altland and Ben D. Simons. *Condensed Matter Field Theory*. Cambridge University Press, Cambridge, 2 edition, 2010.

[43] P.C. Hohenberg and A.P. Krekhov. An introduction to the ginzburg–landau theory of phase transitions and nonequilibrium patterns. *Physics Reports*, 572:1–42, 2015. An introduction to the Ginzburg–Landau theory of phase transitions and nonequilibrium patterns.

[44] N. D. Mermin and H. Wagner. Absence of ferromagnetism or antiferromagnetism in one- or two-dimensional isotropic heisenberg models. *Phys. Rev. Lett.*, 17:1133–1136, Nov 1966.

[45] M. Gell-Mann and F. E. Low. Quantum electrodynamics at small distances. *Phys. Rev.*, 95:1300–1312, Sep 1954.

[46] M. Gell-Mann and F. E. Low. Quantum electrodynamics at small distances. *Phys. Rev.*, 95:1300–1312, Sep 1954.

[47] R. Shankar. Renormalization-group approach to interacting fermions. *Rev. Mod. Phys.*, 66:129–192, Jan 1994.

[48] Chester A. Vause. A phenomenological renormalization group approach to electric conductivity with application to high-tc superconductors. *Physics Letters A*, 138(3):131–135, 1989.

[49] R B Stinchcombe and B P Watson. Renormalization group approach for percolation conductivity. *Journal of Physics C: Solid State Physics*, 9(17):3221, sep 1976.

[50] E. V. Teodorovich. Renormalization group method in the problem of the effective conductivity of a randomly heterogeneous porous medium. *Journal of Experimental and Theoretical Physics*, 95(1):67–76, 2002.

[51] Christoph J. Halboth and Walter Metzner. Renormalization-group analysis of the two-dimensional hubbard model. *Phys. Rev. B*, 61:7364–7377, Mar 2000.

[52] Urs Ledermann and Karyn Le Hur. Phases of the two-band model of spinless fermions in one dimension. *Phys. Rev. B*, 61:2497–2505, Jan 2000.

[53] D. Schmeltzer. Quantum criticality at the metal-insulator transition. *Phys. Rev. B*, 63:075105, Jan 2001.

[54] David J. Gross and André Neveu. Dynamical symmetry breaking in asymptotically free field theories. *Phys. Rev. D*, 10:3235–3253, Nov 1974.

[55] Mikolaj D. Uryszek, Elliot Christou, Akbar Jaefari, Frank Krüger, and Bruno Uchoa. Quantum criticality of semi-dirac fermions in $2+1$ dimensions. *Phys. Rev. B*, 100:155101, Oct 2019.

[56] Hiroki Isobe, Bohm-Jung Yang, Andrey Chubukov, Jörg Schmalian, and Naoto Nagaosa. Emergent non-fermi-liquid at the quantum critical point of a topological phase transition in two dimensions. *Phys. Rev. Lett.*, 116:076803, Feb 2016.

[57] G. R. Stewart. Non-fermi-liquid behavior in d- and f-electron metals. *Rev. Mod. Phys.*, 73:797–855, Oct 2001.

[58] P. Coleman. Theories of non-fermi liquid behavior in heavy fermions. *Physica B: Condensed Matter*, 259-261:353–358, 1999.

[59]

[60] Sung-Sik Lee. Recent developments in non-fermi liquid theory. *Annual Review of Condensed Matter Physics*, 9(Volume 9, 2018):227–244, 2018.

[61] Huajia Wang, Srinivas Raghu, and Gonzalo Torroba. Non-fermi-liquid superconductivity: Eliashberg approach versus the renormalization group. *Phys. Rev. B*, 95:165137, Apr 2017.

[62] Nikolai Zerf, Luminita N. Mihaila, Peter Marquard, Igor F. Herbut, and Michael M. Scherer. Four-loop critical exponents for the gross-neveu-yukawa models. *Phys. Rev. D*, 96:096010, Nov 2017.

[63] P W Anderson. A poor man's derivation of scaling laws for the kondo problem. *Journal of Physics C: Solid State Physics*, 3(12):2436–2441, dec 1970.

[64] M. P. Kwasigroch, Huanzhi Hu, F. Krüger, and A. G. Green. Magnetic hard-direction ordering in anisotropic kondo systems. *Phys. Rev. B*, 105:224418, Jun 2022.

[65] Clarina de la Cruz, Q. Huang, J. W. Lynn, Jiying Li, W. Ratcliff II, J. L. Zarestky, H. A. Mook, G. F. Chen, J. L. Luo, N. L. Wang, and Pengcheng Dai. Magnetic order close to superconductivity in the iron-based layered lao1-xf x feas systems. *Nature*, 453(7197):899–902, 2008.

[66] Jun Zhao, Q. Huang, Clarina de la Cruz, Shiliang Li, J. W. Lynn, Y. Chen, M. A. Green, G. F. Chen, G. Li, Z. Li, J. L. Luo, N. L. Wang, and Pengcheng Dai. Structural and magnetic phase diagram of cefeaso1?xfx and its relation to high-temperature superconductivity. *Nature Materials*, 7(12):953–959, 2008.

[67] R. M. Fernandes, A. V. Chubukov, and J. Schmalian. What drives nematic order in iron-based superconductors? *Nature Physics*, 10(2):97–104, 2014.

[68] P. W. Anderson and W. F. Brinkman. Anisotropic superfluidity in ^{3}He: A possible interpretation of its stability as a spin-fluctuation effect. *Phys. Rev. Lett.*, 30:1108–1111, May 1973.

[69] D. Fay and J. Appel. Coexistence of p-state superconductivity and itinerant ferromagnetism. *Phys. Rev. B*, 22:3173–3182, Oct 1980.

[70] Andrew G. Green, Gareth Conduit, and Frank Krüger. Quantum order-by-disorder in strongly correlated metals. *Annual Review of Condensed Matter Physics*, 9(1):59–77, 2018.

[71] M. Brando, D. Belitz, F. M. Grosche, and T. R. Kirkpatrick. Metallic quantum ferromagnets. *Rev. Mod. Phys.*, 88:025006, May 2016.

[72] D. Belitz, T. R. Kirkpatrick, and Thomas Vojta. First order transitions and multicritical points in weak itinerant ferromagnets. *Phys. Rev. Lett.*, 82:4707–4710, Jun 1999.

[73] Andrey V. Chubukov, Catherine Pépin, and Jerome Rech. Instability of the quantum-critical point of itinerant ferromagnets. *Phys. Rev. Lett.*, 92:147003, Apr 2004.

[74] D. Belitz, T. R. Kirkpatrick, and Thomas Vojta. How generic scale invariance influences quantum and classical phase transitions. *Rev. Mod. Phys.*, 77:579–632, Jul 2005.

[75] T. R. Kirkpatrick and D. Belitz. Universal low-temperature tricritical point in metallic ferromagnets and ferrimagnets. *Phys. Rev. B*, 85:134451, Apr 2012.

[76] C. Pfleiderer, S. R. Julian, and G. G. Lonzarich. Non-fermi-liquid nature of the normal state of itinerant-electron ferromagnets. *Nature*, 414(6862):427–430, 2001.

[77] Y. J. Uemura, T. Goko, I. M. Gat-Malureanu, J. P. Carlo, P. L. Russo, A. T. Savici, A. Aczel, G. J. MacDougall, J. A. Rodriguez, G. M. Luke, S. R.

Dunsiger, A. McCollam, J. Arai, Ch. Pfleiderer, P. Böni, K. Yoshimura, E. Baggio-Saitovitch, M. B. Fontes, J. Larrea, Y. V. Sushko, and J. Sereni. Phase separation and suppression of critical dynamics at quantum phase transitions of mnsi and (sr1?xcax)ruo3. *Nature Physics*, 3(1):29–35, 2007.

[78] M. Otero-Leal, F. Rivadulla, M. García-Hernández, A. Piñeiro, V. Pardo, D. Baldomir, and J. Rivas. Effect of spin fluctuations on the thermodynamic and transport properties of the itinerant ferromagnet cos_2. *Phys. Rev. B*, 78:180415, Nov 2008.

[79] V. Taufour, D. Aoki, G. Knebel, and J. Flouquet. Tricritical point and wing structure in the itinerant ferromagnet uge_2. *Phys. Rev. Lett.*, 105:217201, Nov 2010.

[80] E. A. Yelland, J. M. Barraclough, W. Wang, K. V. Kamenev, and A. D. Huxley. High-field superconductivity at an electronic topological transition in urhge. *Nature Physics*, 7(11):890–894, 2011.

[81] G. J. Conduit, C. J. Pedder, and A. G. Green. Fluctuation-induced pair density wave in itinerant ferromagnets. *Phys. Rev. B*, 87:121112, Mar 2013.

[82] G. J. Conduit, A. G. Green, and B. D. Simons. Inhomogeneous phase formation on the border of itinerant ferromagnetism. *Phys. Rev. Lett.*, 103:207201, Nov 2009.

[83] Una Karahasanovic, Frank Krüger, and Andrew G. Green. Quantum order-by-disorder driven phase reconstruction in the vicinity of ferromagnetic quantum critical points. *Phys. Rev. B*, 85:165111, Apr 2012.

[84] C. J. Pedder, F. Krüger, and A. G. Green. Resummation of fluctuations near ferromagnetic quantum critical points. *Phys. Rev. B*, 88:165109, Oct 2013.

[85] Valentin Taufour, Udhara S. Kaluarachchi, Rustem Khasanov, Manh Cuong Nguyen, Zurab Guguchia, Pabitra Kumar Biswas, Pietro Bonfà, Roberto De Renzi, Xiao Lin, Stella K. Kim, Eun Deok Mun, Hyunsoo Kim, Yuji

Furukawa, Cai-Zhuang Wang, Kai-Ming Ho, Sergey L. Bud'ko, and Paul C. Canfield. Ferromagnetic quantum critical point avoided by the appearance of another magnetic phase in lacrge$_3$ under pressure. *Phys. Rev. Lett.*, 117:037207, Jul 2016.

[86] Sven Friedemann, Will J. Duncan, Max Hirschberger, Thomas W. Bauer, Robert Küchler, Andreas Neubauer, Manuel Brando, Christian Pfleiderer, and F. Malte Grosche. Quantum tricritical points in nbfe2. *Nature Physics*, 14(1):62–67, 2018.

[87] C. Pfleiderer, D. Reznik, L. Pintschovius, H. v. Löhneysen, M. Garst, and A. Rosch. Partial order in the non-fermi-liquid phase of mnsi. *Nature*, 427(6971):227–231, 2004.

[88] Frank Krüger, Una Karahasanovic, and Andrew G. Green. Quantum order-by-disorder near criticality and the secret of partial order in mnsi. *Phys. Rev. Lett.*, 108:067003, Feb 2012.

[89] D. Hafner, Binod K. Rai, J. Banda, K. Kliemt, C. Krellner, J. Sichelschmidt, E. Morosan, C. Geibel, and M. Brando. Kondo-lattice ferromagnets and their peculiar order along the magnetically hard axis determined by the crystalline electric field. *Phys. Rev. B*, 99:201109, May 2019.

[90] Ordering along the magnetic hard axis was observed in the metallic ferromagnets $CeAgSb_2$ [94], CeRuPO [95], $CeFeAs_{0.7}P_{0.3}O$ [96], $Yb(Rh_{0.73}Co_{0.27})_2Si_2$ [97], $YbNi_4P_2$ [98], $YbIr_3Ge_7$ [99], YbNiSn [110], YbPtGe [111], YbRhSb [112], YbPdSi [113], β-$CeNiSb_3$ [234], $CeIrGe_3$ [100, 101].

[91] Eric C. Andrade, Manuel Brando, Christoph Geibel, and Matthias Vojta. Competing orders, competing anisotropies, and multicriticality: The case of co-doped ybrh$_2$si$_2$. *Phys. Rev. B*, 90:075138, Aug 2014.

[92] F. Krüger, C. J. Pedder, and A. G. Green. Fluctuation-driven magnetic hard-axis ordering in metallic ferromagnets. *Phys. Rev. Lett.*, 113:147001, Oct 2014.

[93] Jun Kondo. Resistance minimum in dilute magnetic alloys. *Progress of Theoretical Physics*, 32(1):37–49, 07 1964.

[94] K.D Myers, S.L Bud'ko, I.R Fisher, Z Islam, H Kleinke, A.H Lacerda, and P.C Canfield. Systematic study of anisotropic transport and magnetic properties of ragsb2 (r=y, la?nd, sm, gd?tm). *Journal of Magnetism and Magnetic Materials*, 205(1):27 – 52, 1999.

[95] C. Krellner and C. Geibel. Single crystal growth and anisotropy of cerupo. *Journal of Crystal Growth*, 310(7):1875 – 1880, 2008.

[96] A. Jesche, T. Förster, J. Spehling, M. Nicklas, M. de Souza, R. Gumeniuk, H. Luetkens, T. Goltz, C. Krellner, M. Lang, J. Sichelschmidt, H.-H. Klauss, and C. Geibel. Ferromagnetism and superconductivity in cefeas$_{1-x}P_x$o ($0 \leq x \leq 40$). *Phys. Rev. B*, 86:020501, Jul 2012.

[97] S. Lausberg, A. Hannaske, A. Steppke, L. Steinke, T. Gruner, L. Pedrero, C. Krellner, C. Klingner, M. Brando, C. Geibel, and F. Steglich. Doped ybrh$_2$si$_2$: Not only ferromagnetic correlations but ferromagnetic order. *Phys. Rev. Lett.*, 110:256402, Jun 2013.

[98] Alexander Steppke, Robert Küchler, Stefan Lausberg, Edit Lengyel, Lucia Steinke, Robert Borth, Thomas Lühmann, Cornelius Krellner, Michael Nicklas, Christoph Geibel, Frank Steglich, and Manuel Brando. Ferromagnetic quantum critical point in the heavy-fermion metal ybni4(p1-xasx)2. *Science*, 339(6122):933–936, 2013.

[99] Binod K. Rai, Macy Stavinoha, J. Banda, D. Hafner, Katherine A. Benavides, D. A. Sokolov, Julia Y. Chan, M. Brando, C.-L. Huang, and E. Morosan. Ferromagnetic ordering along the hard axis in the kondo lattice ybir$_3$ge$_7$. *Phys. Rev. B*, 99:121109, Mar 2019.

[100] Yuji Muro, Duhwa Eom, Naoya Takeda, and Masayasu Ishikawa. Contrasting kondo-lattice behavior in cetsi 3 and cetge 3 (t=rh and ir). *Journal of the Physical Society of Japan*, 67(10):3601–3604, 1998.

[101] V. K. Anand, A. D. Hillier, D. T. Adroja, D. D. Khalyavin, P. Manuel, G. Andre, S. Rols, and M. M. Koza. Understanding the magnetism in noncentrosymmetric ceirge$_3$: Muon spin relaxation and neutron scattering studies. *Phys. Rev. B*, 97:184422, May 2018.

[102] Akihiro Kondo, Koichi Kindo, Keisuke Kunimori, Hiroki Nohara, Hiroshi Tanida, Masafumi Sera, Riki Kobayashi, Takashi Nishioka, and Masahiro Matsumura. Marked change in the ground state of ceru2al10 induced by small amount of rh substitution. *Journal of the Physical Society of Japan*, 82(5):054709, 2013.

[103] D. D. Khalyavin, D. T. Adroja, P. Manuel, J. Kawabata, K. Umeo, T. Takabatake, and A. M. Strydom. Change of magnetic ground state by light electron doping in ceos$_2$al$_{10}$. *Phys. Rev. B*, 88:060403, Aug 2013.

[104] Tetsuya Takeuchi, Tetsutaro Inoue, Kiyohiro Sugiyama, Dai Aoki, Yoshihumi Tokiwa, Yoshinori Haga, Koichi Kindo, and Yoshichika Onuki. Magnetic and thermal properties of ceirin5 and cerhin5. *Journal of the Physical Society of Japan*, 70(3):877–883, 2001.

[105] R. Žitko, R. Peters, and Th. Pruschke. Properties of anisotropic magnetic impurities on surfaces. *Phys. Rev. B*, 78:224404, Dec 2008.

[106] See Supplemental Material at ¡insert address¿ for further details.

[107] A. K. Zhuravlev. Negative impurity magnetic susceptibility and heat capacity in a Kondo model with narrow peaks in the local density of electron states. *Physics of Metals and Metallography*, 108(2):107–115, August 2009.

[108] Tie-Feng Fang, Ning-Hua Tong, Zhan Cao, Qing-Feng Sun, and Hong-Gang Luo. Spin susceptibility of anderson impurities in arbitrary conduction bands. *Phys. Rev. B*, 92:155129, Oct 2015.

[109] Ke Yang and Ning-Hua Tong. On the truncation error of numerical renormalization group, 2020.

[110] Mitsuo Kasaya, Tomofune Tani, Katsuyuki Kawate, Toshio Mizushima, Yosikazu Isikawa, and Kiyoo Sato. Magnetic properties of the dense kondo compound ybnisn. *Journal of the Physical Society of Japan*, 60(9):3145–3149, 1991.

[111] Kenichi Katoh, Seisuke Nakagawa, Giichi Terui, and Akira Ochiai. Magnetic and transport properties of single-crystal ybptge. *Journal of the Physical Society of Japan*, 78(10):104721, 2009.

[112] Y. Muro, Y. Haizaki, M. S. Kim, K. Umeo, H. Tou, M. Sera, and T. Takabatake. Heavy-fermion weak-ferromagnet ybrhsb. *Phys. Rev. B*, 69:020401, Jan 2004.

[113] Naohito Tsujii, Lukas Keller, Andreas Dönni, and Hideaki Kitazawa. Anisotropic magnetic properties and magnetic structure of ybpdsi. *Journal of Physics: Condensed Matter*, 28(33):336002, jun 2016.

[114] Leo Kouwenhoven and Leonid Glazman. Revival of the kondo effect. *Physics World*, 14(1):33–38, jan 2001.

[115] Jiutao Li, Wolf-Dieter Schneider, Richard Berndt, and Bernard Delley. Kondo scattering observed at a single magnetic impurity. *Phys. Rev. Lett.*, 80:2893–2896, Mar 1998.

[116] V. Madhavan, W. Chen, T. Jamneala, M. F. Crommie, and N. S. Wingreen. Tunneling into a single magnetic atom: Spectroscopic evidence of the kondo resonance. *Science*, 280(5363):567–569, 1998.

[117] Nikolaus Knorr, M. Alexander Schneider, Lars Diekhöner, Peter Wahl, and Klaus Kern. Kondo effect of single co adatoms on cu surfaces. *Phys. Rev. Lett.*, 88:096804, Feb 2002.

[118] D. Goldhaber-Gordon, Hadas Shtrikman, D. Mahalu, David Abusch-Magder, U. Meirav, and M. A. Kastner. Kondo effect in a single-electron transistor. *Nature*, 391(6663):156–159, 1998.

[119] R. M. Potok, I. G. Rau, Hadas Shtrikman, Yuval Oreg, and D. Goldhaber-Gordon. Observation of the two-channel kondo effect. *Nature*, 446(7132):167–171, 2007.

[120] Huanzhi Hu, Jennifer Lin, Mikolaj D. Uryszek, and Frank Krüger. Stability of the néel quantum critical point in the presence of dirac fermions. *Phys. Rev. B*, 107:085113, Feb 2023.

[121] M. Z. Hasan and C. L. Kane. Colloquium: Topological insulators. *Rev. Mod. Phys.*, 82:3045–3067, Nov 2010.

[122] Xiao-Liang Qi and Shou-Cheng Zhang. Topological insulators and superconductors. *Rev. Mod. Phys.*, 83:1057–1110, Oct 2011.

[123] Oskar Vafek and Ashvin Vishwanath. Dirac fermions in solids: From high-tc cuprates and graphene to topological insulators and weyl semimetals. *Annual Review of Condensed Matter Physics*, 5(1):83–112, 2014.

[124] Binghai Yan and Claudia Felser. Topological materials: Weyl semimetals. *Annual Review of Condensed Matter Physics*, 8(1):337–354, 2017.

[125] N. P. Armitage, E. J. Mele, and Ashvin Vishwanath. Weyl and dirac semimetals in three-dimensional solids. *Rev. Mod. Phys.*, 90:015001, Jan 2018.

[126] M. Zahid Hasan, Guoqing Chang, Ilya Belopolski, Guang Bian, Su-Yang Xu, and Jia-Xin Yin. Weyl, dirac and high-fold chiral fermions in topological quantum matter. *Nature Reviews Materials*, 6(9):784–803, 2021.

[127] Maxim Dzero, Kai Sun, Victor Galitski, and Piers Coleman. Topological kondo insulators. *Phys. Rev. Lett.*, 104:106408, Mar 2010.

[128] Maxim Dzero, Jing Xia, Victor Galitski, and Piers Coleman. Topological kondo insulators. *Annual Review of Condensed Matter Physics*, 7(1):249–280, 2016.

[129] Hsin-Hua Lai, Sarah E. Grefe, Silke Paschen, and Qimiao Si. Weyl–kondo semimetal in heavy-fermion systems. *Proceedings of the National Academy of Sciences*, 115(1):93–97, 2018.

[130] Sami Dzsaber, Xinlin Yan, Mathieu Taupin, Gaku Eguchi, Andrey Prokofiev, Toni Shiroka, Peter Blaha, Oleg Rubel, Sarah E. Grefe, Hsin-Hua Lai, Qimiao Si, and Silke Paschen. Giant spontaneous hall effect in a nonmagnetic weyl–kondo semimetal. *Proceedings of the National Academy of Sciences*, 118(8):e2013386118, 2021.

[131] Adolfo G. Grushin, Eduardo V. Castro, Alberto Cortijo, Fernando de Juan, María A. H. Vozmediano, and Belén Valenzuela. Charge instabilities and topological phases in the extended hubbard model on the honeycomb lattice with enlarged unit cell. *Phys. Rev. B*, 87:085136, Feb 2013.

[132] Noel A. García-Martínez, Adolfo G. Grushin, Titus Neupert, Belén Valenzuela, and Eduardo V. Castro. Interaction-driven phases in the half-filled spinless honeycomb lattice from exact diagonalization. *Phys. Rev. B*, 88:245123, Dec 2013.

[133] Maria Daghofer and Martin Hohenadler. Phases of correlated spinless fermions on the honeycomb lattice. *Phys. Rev. B*, 89:035103, Jan 2014.

[134] Sylvain Capponi and Andreas M. Läuchli. Phase diagram of interacting spinless fermions on the honeycomb lattice: A comprehensive exact diagonalization study. *Phys. Rev. B*, 92:085146, Aug 2015.

[135] Johannes Motruk, Adolfo G. Grushin, Fernando de Juan, and Frank Pollmann. Interaction-driven phases in the half-filled honeycomb lattice: An infinite density matrix renormalization group study. *Phys. Rev. B*, 92:085147, Aug 2015.

[136] Daniel D. Scherer, Michael M. Scherer, and Carsten Honerkamp. Correlated spinless fermions on the honeycomb lattice revisited. *Phys. Rev. B*, 92:155137, Oct 2015.

[137] Yanick Volpez, Daniel D. Scherer, and Michael M. Scherer. Electronic instabilities of the extended hubbard model on the honeycomb lattice from functional renormalization. *Phys. Rev. B*, 94:165107, Oct 2016.

[138] Moyuru Kurita, Youhei Yamaji, and Masatoshi Imada. Stabilization of topological insulator emerging from electron correlations on honeycomb lattice and its possible relevance in twisted bilayer graphene. *Phys. Rev. B*, 94:125131, Sep 2016.

[139] D. Sánchez de la Peña, J. Lichtenstein, and C. Honerkamp. Competing electronic instabilities of extended hubbard models on the honeycomb lattice: A functional renormalization group calculation with high-wave-vector resolution. *Phys. Rev. B*, 95:085143, Feb 2017.

[140] Elliot Christou, Bruno Uchoa, and Frank Krüger. Hidden charge order of interacting dirac fermions on the honeycomb lattice. *Phys. Rev. B*, 98:161120, Oct 2018.

[141] Zi-Xiang Li, Yi-Fan Jiang, Shao-Kai Jian, and Hong Yao. Fermion-induced quantum critical points. *Nature Communications*, 8(1):314, 2017.

[142] Igor F. Herbut. Interactions and phase transitions on graphene's honeycomb lattice. *Phys. Rev. Lett.*, 97:146401, Oct 2006.

[143] Igor F. Herbut, Vladimir Juricic, and Bitan Roy. Theory of interacting electrons on the honeycomb lattice. *Phys. Rev. B*, 79:085116, Feb 2009.

[144] Fakher F. Assaad and Igor F. Herbut. Pinning the order: The nature of quantum criticality in the hubbard model on honeycomb lattice. *Phys. Rev. X*, 3:031010, Aug 2013.

[145] David J. Gross and André Neveu. Dynamical symmetry breaking in asymptotically free field theories. *Phys. Rev. D*, 10:3235–3253, Nov 1974.

[146] J. Zinn-Justin. Four-fermion interaction near four dimensions. *Nuclear Physics B*, 367(1):105 – 122, 1991.

[147] G. Gat, A. Kovner, B. Rosenstein, and B.J. Warr. Four-fermi interaction in (2+1) dimensions beyond leading order in 1/n. *Physics Letters B*, 240(1):158 – 162, 1990.

[148] J.A. Gracey. Calculation of exponent to o(1/n2) in the o(n) gross neveu model. *International Journal of Modern Physics A*, 06(03):395–407, 1991.

[149] J.A. Gracey. Anomalous mass dimension at o(1/n2) in the o(n) gross-neveu model. *Physics Letters B*, 297(3):293 – 297, 1992.

[150] Aleksandr Nikolaevich Vasil'ev and AS Stepanenko. The 1/n expansion in the gross-neveu model: Conformal bootstrap calculation of the exponent 1/v to the order 1/n 2. *Theoretical and Mathematical Physics*, 97(3):1349–1354, 1993.

[151] J.A. Gracey. Computation of critical exponent at o(1/n3) in the four-fermi model in arbitrary dimensions. *International Journal of Modern Physics A*, 9(5):727–744, 1994.

[152] Luca Iliesiu, Filip Kos, David Poland, Silviu S. Pufu, and David Simmons-Duffin. Bootstrapping 3d fermions with global symmetries. *Journal of High Energy Physics*, 2018(1):36, Jan 2018.

[153] Mikolaj D. Uryszek, Frank Krüger, and Elliot Christou. Fermionic criticality of anisotropic nodal point semimetals away from the upper critical dimen-

sion: Exact exponents to leading order in $\frac{1}{N_f}$. *Phys. Rev. Res.*, 2:043265, Nov 2020.

[154] Sudip Chakravarty, Bertrand I. Halperin, and David R. Nelson. Low-temperature behavior of two-dimensional quantum antiferromagnets. *Phys. Rev. Lett.*, 60:1057–1060, Mar 1988.

[155] Sudip Chakravarty, Bertrand I. Halperin, and David R. Nelson. Two-dimensional quantum heisenberg antiferromagnet at low temperatures. *Phys. Rev. B*, 39:2344–2371, Feb 1989.

[156] Sudip Chakravarty, Bertrand I. Halperin, and David R. Nelson. Two-dimensional quantum heisenberg antiferromagnet at low temperatures. *Phys. Rev. B*, 39:2344–2371, Feb 1989.

[157] Sudip Chakravarty, Bertrand I. Halperin, and David R. Nelson. Low-temperature behavior of two-dimensional quantum antiferromagnets. *Phys. Rev. Lett.*, 60:1057–1060, Mar 1988.

[158] David R. Nelson and Robert A. Pelcovits. Momentum-shell recursion relations, anisotropic spins, and liquid crystals in $2+\varepsilon$ dimensions. *Phys. Rev. B*, 16:2191–2199, Sep 1977.

[159] Shouvik Sur and Bitan Roy. Unifying interacting nodal semimetals: A new route to strong coupling. *Phys. Rev. Lett.*, 123:207601, Nov 2019.

[160] A.M. Polyakov. Interaction of goldstone particles in two dimensions. applications to ferromagnets and massive yang-mills fields. *Physics Letters B*, 59(1):79–81, 1975.

[161] S Hikami and E Brezin. Three-loop calculations in the two-dimensional non-linear model. *Journal of Physics A: Mathematical and General*, 11(6):1141–1150, jun 1978.

[162] Shahnam Ghanbari Saheli, Jennifer Lin, Huanzhi Hu, and Frank Krüger. Majorana-fermion mean field theories of kitaev quantum spin liquids. *Phys. Rev. B*, 109:014407, Jan 2024.

[163] Lucile Savary and Leon Balents. Quantum spin liquids: A review. *Reports on Progress in Physics*, 80(1):016502, Nov 2016.

[164] J. Knolle and R. Moessner. A field guide to spin liquids. *Annual Review of Condensed Matter Physics*, 10(1):451–472, Dec 2018.

[165] M. Hermanns, I. Kimchi, and J. Knolle. Physics of the kitaev model: Fractionalization, dynamic correlations, and material connections. *Annual Review of Condensed Matter Physics*, 9(1):17–33, Jan 2018.

[166] C. Broholm, R. J. Cava, S. A. Kivelson, D. G. Nocera, M. R. Norman, and T. Senthil. Quantum spin liquids. *Science*, 367(6475):eaay0668, 2020.

[167] Jinsheng Wen, Shun-Li Yu, Shiyan Li, Weiqiang Yu, and Jian-Xin Li. Experimental identification of quantum spin liquids. *npj Quantum Materials*, 4(1):12, 2019.

[168] G. Jackeli and G. Khaliullin. Mott insulators in the strong spin-orbit coupling limit: From heisenberg to a quantum compass and kitaev models. *Phys. Rev. Lett.*, 102:017205, Jan 2009.

[169] Yogesh Singh and P. Gegenwart. Antiferromagnetic mott insulating state in single crystals of the honeycomb lattice material na_2iro_3. *Phys. Rev. B*, 82:064412, Aug 2010.

[170] X. Liu, T. Berlijn, W.-G. Yin, W. Ku, A. Tsvelik, Young-June Kim, H. Gretarsson, Yogesh Singh, P. Gegenwart, and J. P. Hill. Long-range magnetic ordering in na_2iro_3. *Phys. Rev. B*, 83:220403, Jun 2011.

[171] Yogesh Singh, S. Manni, J. Reuther, T. Berlijn, R. Thomale, W. Ku, S. Trebst, and P. Gegenwart. Relevance of the heisenberg-kitaev model for the honeycomb lattice iridates A_2iro_3. *Phys. Rev. Lett.*, 108:127203, Mar 2012.

[172] S. K. Choi, R. Coldea, A. N. Kolmogorov, T. Lancaster, I. I. Mazin, S. J. Blundell, P. G. Radaelli, Yogesh Singh, P. Gegenwart, K. R. Choi, S.-W. Cheong, P. J. Baker, C. Stock, and J. Taylor. Spin waves and revised crystal structure of honeycomb iridate na_2iro_3. *Phys. Rev. Lett.*, 108:127204, Mar 2012.

[173] Feng Ye, Songxue Chi, Huibo Cao, Bryan C. Chakoumakos, Jaime A. Fernandez-Baca, Radu Custelcean, T. F. Qi, O. B. Korneta, and G. Cao. Direct evidence of a zigzag spin-chain structure in the honeycomb lattice: A neutron and x-ray diffraction investigation of single-crystal na_2iro_3. *Phys. Rev. B*, 85:180403, May 2012.

[174] T. Takayama, A. Kato, R. Dinnebier, J. Nuss, H. Kono, L. S. I. Veiga, G. Fabbris, D. Haskel, and H. Takagi. Hyperhoneycomb iridate $\beta-li_2iro_3$ as a platform for kitaev magnetism. *Phys. Rev. Lett.*, 114:077202, Feb 2015.

[175] K. A. Modic, Tess E. Smidt, Itamar Kimchi, Nicholas P. Breznay, Alun Biffin, Sungkyun Choi, Roger D. Johnson, Radu Coldea, Pilanda Watkins-Curry, Gregory T. McCandless, Julia Y. Chan, Felipe Gandara, Z. Islam, Ashvin Vishwanath, Arkady Shekhter, Ross D. McDonald, and James G. Analytis. Realization of a three-dimensional spin–anisotropic harmonic honeycomb iridate. *Nature Communications*, 5(1):4203, 2014.

[176] K. W. Plumb, J. P. Clancy, L. J. Sandilands, V. Vijay Shankar, Y. F. Hu, K. S. Burch, Hae-Young Kee, and Young-June Kim. $\alpha-rucl_3$: A spin-orbit assisted mott insulator on a honeycomb lattice. *Phys. Rev. B*, 90:041112, Jul 2014.

[177] A. Banerjee, C. A. Bridges, J. Q. Yan, A. A. Aczel, L. Li, M. B. Stone, G. E. Granroth, M. D. Lumsden, Y. Yiu, J. Knolle, S. Bhattacharjee, D. L. Kovrizhin, R. Moessner, D. A. Tennant, D. G. Mandrus, and S. E. Nagler. Proximate kitaev quantum spin liquid behaviour in a honeycomb magnet. *Nature Materials*, 15(7):733–740, 2016.

[178] Arnab Banerjee, Jiaqiang Yan, Johannes Knolle, Craig A. Bridges, Matthew B. Stone, Mark D. Lumsden, David G. Mandrus, David A. Tennant, Roderich Moessner, and Stephen E. Nagler. Neutron scattering in the proximate quantum spin liquid α-rucl¡sub¿3¡/sub¿. *Science*, 356(6342):1055–1059, 2017.

[179] Hidenori Takagi, Tomohiro Takayama, George Jackeli, Giniyat Khaliullin, and Stephen E. Nagler. Concept and realization of kitaev quantum spin liquids. *Nature Reviews Physics*, 1(4):264–280, 2019.

[180] Ara Go, Jun Jung, and Eun-Gook Moon. Vestiges of topological phase transitions in kitaev quantum spin liquids. *Phys. Rev. Lett.*, 122:147203, Apr 2019.

[181] T. Yokoi, S. Ma, Y. Kasahara, S. Kasahara, T. Shibauchi, N. Kurita, H. Tanaka, J. Nasu, Y. Motome, C. Hickey, S. Trebst, and Y. Matsuda. Half-integer quantized anomalous thermal hall effect in the kitaev material candidate α-rucl¡sub¿3¡/sub¿. *Science*, 373(6554):568–572, 2021.

[182] Martin Mourigal, Mechthild Enderle, Axel Klöpperpieper, Jean-Sébastien Caux, Anne Stunault, and Henrik M. Rønnow. Fractional spinon excitations in the quantum heisenberg antiferromagnetic chain. *Nature Physics*, 9(7):435–441, 2013.

[183] B. Lake, D. A. Tennant, J.-S. Caux, T. Barthel, U. Schollwöck, S. E. Nagler, and C. D. Frost. Multispinon continua at zero and finite temperature in a near-ideal heisenberg chain. *Phys. Rev. Lett.*, 111:137205, Sep 2013.

[184] Philipp Hauke, Markus Heyl, Luca Tagliacozzo, and Peter Zoller. Measuring multipartite entanglement through dynamic susceptibilities. *Nature Physics*, 12(8):778–782, 2016.

[185] A. Scheie, Pontus Laurell, A. M. Samarakoon, B. Lake, S. E. Nagler, G. E. Granroth, S. Okamoto, G. Alvarez, and D. A. Tennant. Witnessing en-

tanglement in quantum magnets using neutron scattering. *Phys. Rev. B*, 103:224434, Jun 2021.

[186] J. Knolle, D. L. Kovrizhin, J. T. Chalker, and R. Moessner. Dynamics of a two-dimensional quantum spin liquid: Signatures of emergent majorana fermions and fluxes. *Phys. Rev. Lett.*, 112:207203, May 2014.

[187] J. Knolle, D. L. Kovrizhin, J. T. Chalker, and R. Moessner. Dynamics of fractionalization in quantum spin liquids. *Phys. Rev. B*, 92:115127, Sep 2015.

[188] Johannes Knolle, Subhro Bhattacharjee, and Roderich Moessner. Dynamics of a quantum spin liquid beyond integrability: The kitaev-heisenberg-Γ model in an augmented parton mean-field theory. *Phys. Rev. B*, 97:134432, Apr 2018.

[189] Matthias Gohlke, Ruben Verresen, Roderich Moessner, and Frank Pollmann. Dynamics of the kitaev-heisenberg model. *Phys. Rev. Lett.*, 119:157203, Oct 2017.

[190] F. J. Burnell and Chetan Nayak. Su(2) slave fermion solution of the kitaev honeycomb lattice model. *Phys. Rev. B*, 84:125125, Sep 2011.

[191] Robert Schaffer, Subhro Bhattacharjee, and Yong Baek Kim. Quantum phase transition in heisenberg-kitaev model. *Phys. Rev. B*, 86:224417, Dec 2012.

[192] Hong-Chen Jiang, Zheng-Cheng Gu, Xiao-Liang Qi, and Simon Trebst. Possible proximity of the mott insulating iridate na_2iro_3 to a topological phase: Phase diagram of the heisenberg-kitaev model in a magnetic field. *Phys. Rev. B*, 83:245104, Jun 2011.

[193] Johannes Reuther, Ronny Thomale, and Simon Trebst. Finite-temperature phase diagram of the heisenberg-kitaev model. *Phys. Rev. B*, 84:100406, Sep 2011.

[194] Han-Dong Chen and Zohar Nussinov. Exact results of the kitaev model on a hexagonal lattice: Spin states, string and brane correlators, and anyonic excitations. *Journal of Physics A: Mathematical and Theoretical*, 41(7):075001, 2008.

[195] Jianlong Fu, Johannes Knolle, and Natalia B. Perkins. Three types of representation of spin in terms of majorana fermions and an alternative solution of the kitaev honeycomb model. *Phys. Rev. B*, 97:115142, Mar 2018.

[196] Xiao-Yong Feng, Guang-Ming Zhang, and Tao Xiang. Topological characterization of quantum phase transitions in a spin-$1/2$ model. *Phys. Rev. Lett.*, 98:087204, Feb 2007.

[197] Han-Dong Chen and Jiangping Hu. Exact mapping between classical and topological orders in two-dimensional spin systems. *Phys. Rev. B*, 76:193101, Nov 2007.

[198] Balázs Dóra and Roderich Moessner. Gauge field entanglement in kitaev's honeycomb model. *Phys. Rev. B*, 97:035109, Jan 2018.

[199] Xiao-Gang Wen. Topological order: From long-range entangled quantum matter to a unified origin of light and electrons. *International Scholarly Research Notices*, 2013(1):198710, 2013.

[200] Joji Nasu, Masafumi Udagawa, and Yukitoshi Motome. Vaporization of kitaev spin liquids. *Phys. Rev. Lett.*, 113:197205, Nov 2014.

[201] Joji Nasu, Masafumi Udagawa, and Yukitoshi Motome. Thermal fractionalization of quantum spins in a kitaev model: Temperature-linear specific heat and coherent transport of majorana fermions. *Phys. Rev. B*, 92:115122, Sep 2015.

[202] Joji Nasu, Yasuyuki Kato, Junki Yoshitake, Yoshitomo Kamiya, and Yukitoshi Motome. Spin-liquid–to–spin-liquid transition in kitaev magnets driven by fractionalization. *Phys. Rev. Lett.*, 118:137203, Mar 2017.

[203] Petra Dietl, Frédéric Piéchon, and Gilles Montambaux. New magnetic field dependence of landau levels in a graphenelike structure. *Phys. Rev. Lett.*, 100:236405, Jun 2008.

[204] G. Montambaux, F. Piéchon, J.-N. Fuchs, and M. O. Goerbig. Merging of dirac points in a two-dimensional crystal. *Phys. Rev. B*, 80:153412, Oct 2009.

[205] S. Banerjee, R. R. P. Singh, V. Pardo, and W. E. Pickett. Tight-binding modeling and low-energy behavior of the semi-dirac point. *Phys. Rev. Lett.*, 103:016402, Jul 2009.

[206] Jimin Kim, Seung Su Baik, Sae Hee Ryu, Yeongsup Sohn, Soohyung Park, Byeong-Gyu Park, Jonathan Denlinger, Yeonjin Yi, Hyoung Joon Choi, and Keun Su Kim. Observation of tunable band gap and anisotropic dirac semimetal state in black phosphorus. *Science*, 349(6249):723–726, 2015.

[207] Jimin Kim, Seung Su Baik, Sung Won Jung, Yeongsup Sohn, Sae Hee Ryu, Hyoung Joon Choi, Bohm-Jung Yang, and Keun Su Kim. Two-dimensional dirac fermions protected by space-time inversion symmetry in black phosphorus. *Phys. Rev. Lett.*, 119:226801, Nov 2017.

[208] Kangle Li and Hoi Chun Po. Higher-dimensional jordan-wigner transformation and auxiliary majorana fermions. *Phys. Rev. B*, 106:115109, Sep 2022.

[209] F. Yilmaz, A. P. Kampf, and S. K. Yip. Phase diagrams of kitaev models for arbitrary magnetic field orientations. *Phys. Rev. Res.*, 4:043024, Oct 2022.

[210] Yukitoshi Motome and Joji Nasu. Hunting majorana fermions in kitaev magnets. *Journal of the Physical Society of Japan*, 89(1):012002, 2020.

[211] Hoi Chun Po, Symmetric Jordan-Wigner transformation in higher dimensions, arXiv:2107.10842.

[212] Juan Osorio Iregui, Philippe Corboz, and Matthias Troyer. Probing the stability of the spin-liquid phases in the kitaev-heisenberg model using tensor network algorithms. *Phys. Rev. B*, 90:195102, Nov 2014.

[213] Kazuya Shinjo, Shigetoshi Sota, and Takami Tohyama. Density-matrix renormalization group study of the extended kitaev-heisenberg model. *Phys. Rev. B*, 91:054401, Feb 2015.

[214] Darshan G. Joshi. Topological excitations in the ferromagnetic kitaev-heisenberg model. *Phys. Rev. B*, 98:060405, Aug 2018.

[215] R. L. Smit, S. Keupert, O. Tsyplyatyev, P. A. Maksimov, A. L. Chernyshev, and P. Kopietz. Magnon damping in the zigzag phase of the kitaev-heisenberg-Γ model on a honeycomb lattice. *Phys. Rev. B*, 101:054424, Feb 2020.

[216] Pedro M. Cônsoli, Lukas Janssen, Matthias Vojta, and Eric C. Andrade. Heisenberg-kitaev model in a magnetic field: $1/s$ expansion. *Phys. Rev. B*, 102:155134, Oct 2020.

[217] Animesh Nanda, Adhip Agarwala, and Subhro Bhattacharjee. Phases and quantum phase transitions in the anisotropic antiferromagnetic kitaev-heisenberg-Γ magnet. *Phys. Rev. B*, 104:195115, Nov 2021.

[218] Huanzhi Hu and Frank Krüger. Nature of topological phase transition of kitaev quantum spin liquids. *Phys. Rev. Lett.*, 133:146603, Oct 2024.

[219] A.Yu. Kitaev. Fault-tolerant quantum computation by anyons. *Annals of Physics*, 303(1):2–30, 2003.

[220] Ji ří Chaloupka, George Jackeli, and Giniyat Khaliullin. Kitaev-heisenberg model on a honeycomb lattice: Possible exotic phases in iridium oxides A_2iro$_3$. *Phys. Rev. Lett.*, 105:027204, Jul 2010.

[221] Hiroki Isobe, Bohm-Jung Yang, Andrey Chubukov, Jörg Schmalian, and Naoto Nagaosa. Emergent non-fermi-liquid at the quantum critical point of a topological phase transition in two dimensions. *Phys. Rev. Lett.*, 116:076803, Feb 2016.

[222] Mikolaj D. Uryszek, Frank Krüger, and Elliot Christou. Fermionic criticality of anisotropic nodal point semimetals away from the upper critical dimension: Exact exponents to leading order in $\frac{1}{N_f}$. *Phys. Rev. Res.*, 2:043265, Nov 2020.

[223] Mikolaj D. Uryszek, Elliot Christou, Akbar Jaefari, Frank Krüger, and Bruno Uchoa. Quantum criticality of semi-dirac fermions in $2+1$ dimensions. *Phys. Rev. B*, 100:155101, Oct 2019.

[224] Jing-Rong Wang, Guo-Zhu Liu, and Chang-Jin Zhang. Excitonic pairing and insulating transition in two-dimensional semi-dirac semimetals. *Phys. Rev. B*, 95:075129, Feb 2017.

[225] Bitan Roy and Matthew S. Foster. Quantum multicriticality near the dirac-semimetal to band-insulator critical point in two dimensions: A controlled ascent from one dimension. *Phys. Rev. X*, 8:011049, Mar 2018.

[226] S. Doniach. The kondo lattice and weak antiferromagnetism. *Physica B+C*, 91:231 – 234, 1977.

[227] A.V. Goltsev. Competition, coexistence and interplay between magnetic order, kondo effect and superconductivity in heavy-fermion compounds. *Physica B: Condensed Matter*, 192(4):403–418, 1993.

[228] B. H. Bernhard and C. Lacroix. Coexistence of magnetic order and kondo effect in the kondo-heisenberg model. *Phys. Rev. B*, 92:094401, Sep 2015.

[229] B. Coqblin and J. R. Schrieffer. Exchange interaction in alloys with cerium impurities. *Phys. Rev.*, 185:847–853, Sep 1969.

[230] Urban F. P. Seifert, Tobias Meng, and Matthias Vojta. Fractionalized fermi liquids and exotic superconductivity in the kitaev-kondo lattice. *Phys. Rev. B*, 97:085118, Feb 2018.

[231] Shang-Shun Zhang, Gábor B. Halász, and Cristian D. Batista. Theory of the kitaev model in a $[111]$ magnetic field. *Nature Communications*, 13(1):399, 2022.

[232] Xiao-Gang Wen. Quantum orders and symmetric spin liquids. *Phys. Rev. B*, 65:165113, Apr 2002.

[233] Rufus Boyack, Chien-Hung Lin, Nikolai Zerf, Ahmed Rayyan, and Joseph Maciejko. Transition between algebraic and z_2 quantum spin liquids at large n. *Phys. Rev. B*, 98:035137, Jul 2018.

[234] Evan Lyle Thomas, Dixie P. Gautreaux, Han-Oh Lee, Zachary Fisk, and Julia Y. Chan. Discovery of ?-lnnisb3 (ln = la, ce): Crystal growth, structure, and magnetic and transport behavior. *Inorganic Chemistry*, 46(8):3010–3016, 04 2007.